UNIVERSIDADE ESTADUAL DE CAMPINAS
INSTITUTO DE GEOCIÊNCIAS

BRUNO CÉSAR ZANARDO HONÓRIO

DEVELOPMENT AND APPLICATIONS OF TIME-FREQUENCY BASED SEISMIC ATTRIBUTES

DESENVOLVIMENTO E APLICAÇÕES DE ATRIBUTOS SÍSMICOS BASEADOS EM ANÁLISES TEMPO-FREQUÊNCIA

CAMPINAS
2016

BRUNO CÉSAR ZANARDO HONÓRIO

DEVELOPMENT AND APPLICATIONS OF TIME-FREQUENCY BASED SEISMIC ATTRIBUTES

DESENVOLVIMENTO E APLICAÇÕES DE ATRIBUTOS SÍSMICOS BASEADOS EM ANÁLISES TEMPO-FREQUÊNCIA

THESIS PRESENTED TO THE INSTITUTE OF GEOSCIENCES OF THE UNIVERSITY OF CAMPINAS AS PART TO OBTAIN THE DEGREE OF DOCTOR IN CIENCES IN AREA OF GEOLOGY AND NATURAL RESOURCES

TESE APRESENTADA AO INSTITUTO DE GEOCIÊNCIAS DA UNIVERSIDADE ESTADUAL DE CAMPINAS COMO REQUISITO PARA OBTENÇÃO DO TITULO DE DOUTOR EM CIÊNCIAS NA ÁREA DE GEOLOGIA E RECURSOS NATURAIS

ORIENTADOR: PROF. DR. ALEXANDRE CAMPANE VIDAL

COORIENTADOR: PROF. DR. MARCÍLIO CASTRO DE MATOS

ESTE EXEMPLAR CORRESPONDE À VERSÃO FINAL DA TESE DEFENDIDA PELO ALUNO BRUNO CÉSAR ZANARDO HONÓRIO E ORIENTADO PELO PROF. DR. S ALEXANDRE CAMPANE VIDAL

CAMPINAS

2016

Agência(s) de fomento e nº(s) de processo(s): CNPq, 142102/2012-1

Ficha catalográfica
Universidade Estadual de Campinas
Biblioteca do Instituto de Geociências
Cássia Raquel da Silva - CRB 8/5752

H759d

Honório, Bruno César Zanardo, 1983-
Development and applications of time-frequency based seismic attributes / Bruno César Zanardo Honório. – Campinas, SP : [s.n.], 2016.

Orientador: Alexandre Campane Vidal.
Coorientador: Marcílio Castro de Matos.
Tese (doutorado) – Universidade Estadual de Campinas, Instituto de Geociências.

1. Geofísica. 2. Ondas sísmicas. 3. Método sísmico de reflexão. 4. Processamento de sinais - Análise espectral. I. Vidal, Alexandre Campane,1969-. II. Matos, Marcílio Castro de. III. Universidade Estadual de Campinas. Instituto de Geociências. IV. Título.

Informações para Biblioteca Digital

Título em outro idioma: Desenvolvimento e aplicação de atributos sísmicos baseados em análises tempo-frequencia
Palavras-chave em inglês:
Geophysics
Seismic waves
Seismic reflection method
Signal processing - spectral analysis
Área de concentração: Geologia e Recursos Naturais
Titulação: Doutor em Geociências
Banca examinadora:
Alexandre Campane Vidal [Orientador]
Emilson Pereira Leite
João Marcos Travassos Romano
Luis Alberto D'Afonseca
Rodrigo Drummond Couto Duarte
Data de defesa: 12-09-2016
Programa de Pós-Graduação: Geociências

UNIVERSIDADE ESTADUAL DE CAMPINAS
INSTITUTO DE GEOCIÊNCIAS
PÓS-GRADUAÇÃO EM GEOCIÊNCIAS NA
ÀREA DE GEOLOGIA E RECURSOS NATURAIS

AUTOR: Bruno César Zanardo Honório

"**Desenvolvimento e aplicações de atributos sísmicos baseados em análises tempo-frequência.**"

ORIENTADOR: Prof. Dr. Alexandre Campane Vidal

COORIENTADOR: Prof. Dr. Marcílio Castro de Matos

Aprovado em: 12 / 09 / 2016

EXAMINADORES:

Prof. Dr. Alexandre Campane Vidal – Orientador

Prof. Dr. Emilson Pereira Leite

Prof. Dr. João Marcos Travassos Romano

Prof. Dr. Luis Alberto D'Afonseca

Dr. Rodrigo Drummond Couto Duarte

A Ata de Defesa assinada pelos membros da Comissão Examinadora, consta no processo de vida acadêmica do aluno.

Campinas, 12 de setembro de 2016.

Dedication

To my beloved parents and brother: Zé, Kuca and Lucas

Acknowledgements

If a long journey starts by a first step, it only endures until the finish line by the union of several forces, for which I will be always thankful.

I would like to express my endless gratitude to my advisor Alexandre Vidal, who since the very beginning of the graduate program gave me the ways and motivation to explore and learn this fantastic world of geosciences.

My sincere thanks to my co-advisor Marcílio Matos, who has always been by my side, even geographically little far. I have always admired your geophysical works. Now, I admire you as person as well. You helped me more than you think.

I thank Prof. Dr. Emilson Pereira Leite, Prof. Dr João Marcos Travassos Romano, Dr. Luis Alberto D'Afonseca, Dr. Rodrigo Drummond, and Prof. Dr. Liliana Alcazar Diogo for participating in my qualifying and/or final exams, contributing substantially to the work developed here.

Thanks to all my fellas in the lab.: Ulisses Correia (Giant), Leandro Melani (Galã), Luis Sugi (Luizera), and Alexandre Sanchetta (Champs). I hope I gave you more than nicknames. The list continues: Juliana Bueno, Michelle Kuroda, Aline Belila, Mateus Basso, Guilherme Chinelatto, and Ivan Mingireanov. All and each of you somehow assisted me in this journey.

To my friends I have made in Norway. Although this was not done as part of my PhD., this period has greatly impacted it and my development: Giulio Casini, Sacha Tremblay, David Hunt, Aart-Jan, Alexandra Jurkiw, Fabio Lapponi, Michael Zeller, and Ole Wennberg. No professional development is rich enough without the personal incomes: thanks to Jan Norbisrath, Dan Stokes, Rich McAllister, Tatyana Gabellone, Aleksandra Hosa, Sarah Bateman, Larissa Hansen, and Chandra Tapossea.

To my friends outside the Campus, who teach me what is not in the books. RB, Nadja, Josafá and family.

To all the IGe staff for making the things happen, specially to Valdirene Pinotti who always has the right and precise answers.

Thanks to the Brazilian Council for Technological and Scientific Development (CNPq) for its financial support. I hope I have made a good usage of this public resource.

To my families - of blood (Botucatu and somewhere around) and heart (Campinas). Your support was fundamental.

A special thanks to my beloved wife, Lidia Bertolo. I wish I could return all your love and patience. Your support goes beyond this PhD.

We are, finally, all wanderers in search of knowledge. Most of us hold the dream of becoming something better than we are, something larger, richer, in some way more important to the world and ourselves. Too often, the way taken is the wrong way, with too much emphasis on what we want to have, rather than what we wish to become.

Louis L'Amour (Education of a Wandering Man)

Biography

I am Physicist (2008) and M.Sc. in Science and Petroleum Engineering (2011), both from the University of Campinas - UNICAMP. This document is part of my Ph.D. degree in Geosciences (2016), which was also granted from UNICAMP. Since 2010, I´m collaborating with the Geological Reservoir Modeling (MGR) group at the Centre for Petroleum Studies - CEPETRO, where I´ve been involved in research projects together with oil companies. In 2014, I had my first international work experience, in which I´ve been in the Statoil Carbonate Research Center - Norway, working in a pre-salt oil field in the Santos Basin, Brazil. My academic and professional interests are focused on applied geophysics on the following subjects: characterization of petroleum reservoirs, time-frequency analysis, signal processing, seismic resolution improvement and seismic attributes.

RESUMO

A imagem sísmica é uma composição de diversas estruturas geológicas as quais geralmente possuem diferentes escalas. Por ser condicionada pela frequência dominante da *wavelet* sísmica, esta imagem pode mascarar a detecção de características sutis presentes na subsuperfície. Em contrapartida, a decomposição espectral consegue acessar as componentes do sinal sísmico particulares à uma determinada escala e pode ser útil para compreender as variações de forma de onda, a espessura dentro das zonas de interesse do reservatório e, de modo geral, obter uma informação mais valiosa da geologia sob investigação.

No presente trabalho, estou interessado em desenvolver abordagens e fluxos de trabalho utilizando atributos sísmicos conjuntos à analises tempo-frequência com o objetivo final de fornecer informações mais detalhadas dos dados sísmicos. Especificamente, (1) propus um procedimento baseado na análise de componentes independentes (ICA), um método estatístico de ordem superior, para lidar com os volumes de iso-frequência gerados pela decomposição espectral, a transformada wavelet contínua (CWT) neste caso. As componentes computadas através da ICA são combinadas no espaço de cores vermelho-verde-azul (RGB), produzindo uma única imagem. Realizo um estudo comparativo com a abordagem convencional, a qual escolhe empiricamente as componentes de frequência a serem utilizadas no RGB. Comparo também os resultados com os obtidos pela análise de componentes principais (PCA). Em ambos os casos, o método baseado na ICA pôde gerar uma melhor imagem e fielmente delinear a estrutura de canais do sistema fluvio-deltaico presente no volume sísmico de uma zona *offshore* localizada no setor holandês do Mar do Norte; (2) a metodologia desenvolvida em 1 é aplicada conjuntamente com o atributo *sweetness*, uma relação entre amplitude e frequência instantâneas, e um procedimento de detecção de descontinuidades em um reservatório carbonático do Albiano na Bacia de Campos, Brasil. Neste caso, pudemos mapear diferentes elementos estruturais e padrões litológicos que, por sua vez, puderam ser associados ao Joulters Cays (JC) nas Bahamas, corroborando JC como um análogo moderno para o campo; (3) proponho a combinação de um procedimento para aumento do conteúdo espectral baseado na resolução diferencial (DR) com a extração de atributos de descontinuidades. Ao refinar

o cálculo do atributo de acordo com as diferentes bandas de frequência das componentes da DR e combiná-los no espaço de cores RGBα, pudemos obter uma definição mais detalhada das falhas e estruturas cársticas presentes na área de estudo; (4) por fim, trago a *improved complete ensemble empirical mode decomposition* (ICEEMD), uma técnica proposta no processamento de sinais biomédicos baseada na decomposição em modos empíricos (EMD), para o contexto da análise do sinal sísmico. Neste caso, faço um estudo comparativo com a técnica referência de EMD, i.e., a *complete ensemble empirical mode decomposition* (CEEMD), para dados sintéticos e reais, bem como atributos convencionalmente avaliados no contexto da EMD. Apesar de em alguns casos as diferenças serem sutis, modos melhores separados com menor ocorrência de ruído, melhor distribuição de energia e representação tempo-frequência, características espectrais das reflexões mais claramente resolvidas sugerem a ICEEND como o método de referência para as variações "*noise-assisted*" de EMD.

Palavras-chave: Geofísica, ondas sísmicas, método sísmico de reflexão, processamento de sinais - análise espectral

ABSTRACT

The seismic image is a composite of various geological structures which usually have different scales. Because this image is conditioned by the dominant frequency of the seismic wavelet, it can mask the detection of subtle features present in the subsurface. In contrast, the spectral decomposition can access the components of the seismic signal at a particular scale and can be useful to understand the changes in the waveform, the thickness within the reservoir zones and, in general, obtain a more valuable information from the geology under investigation.

In the present work, I am interested in developing approaches and workflows using time-frequency joint seismic attributes to the final goal of providing deeper and detailed information from the seismic data. Specifically, (1) I have proposed a higher-order statistic procedure based on independent component analysis (ICA) to deal with the iso-frequency volumes generated by spectral decomposition, the continuous wavelet transform (CWT) in this case. The components computed through the ICA are combined into the red-green-blue (RGB) color space, producing a single and good quality image. A comparative study is made with the conventional approach, which chooses empirically the frequency components to be used in the RGB color stack. We also compared the results with the ones obtained by principal component analysis (PCA). In both cases, the ICA based method could generate a better image and faithfully delineate a channel system presented in a fluviodeltaic seismic volume from an offshore zone located in the Dutch sector of the North Sea; (2) The methodology developed in 1 is applied jointly with sweetness attribute, a relation between instantaneous amplitude and instantaneous frequency, and a discontinuity detection procedure in an Albian carbonate reservoir in Campos Basin, Brazil. In this case, we could map different architectural elements and lithological patterns, which in turn could be associated with the Joulters Cays (JC) in the Bahamas, corroborating JC as a modern analog to the field; (3) I have combined a spectral enhancement procedure based differential resolution (DR) with discontinuity attribute extraction. By refining the attribute computation according to the different frequency bands of the DR components and combining them into RGBα, we could get a more detailed definition of the faults and karst structures present in the studied area; (4) Finally, I bring the improved

complete ensemble empirical mode decomposition (ICEEMD), an empirical mode decomposition (EMD) based technique proposed in biomedical signal processing, to the context of seismic signal analysis. In this case, we do a comparative study with the current EMD technique, i.e, the complete ensemble empirical mode decomposition (CEEMD) for synthetic and real seismic data as well the seismic attributes conventionally evaluated in the EMD-based framework. Although in some cases the differences are subtle, better modes separation with lower noise occurrence, better power distribution and time-frequency representation, spectral characteristics of the reflections more clearly resolved suggest ICEEND as the reference method for "noise-assisted" variations of EMD.

Keywords: Geophysics, seismic waves, seismic reflection method, signal processing - spectral analysis

LIST OF FIGURES

TABLE OF CONTENTS

CHAPTER 1: INTRODUCTION

In the past few decades, a considerable effort has been made and significant advances have been achieved in the application of seismic attribute analysis to subsurface oil exploration (Chopra and Marfurt, 2005; 2007). In addition to many classical seismic attributes algorithms (Taner et al., 1979), many emerging ones have been developed, which significantly enhanced the interpreters' ability for identify and characterize a given geological feature under the subsurface seismic data. Nowadays, seismic attributes became an integral part of modern 3D seismic interpretation workflows.

Fundamentally, a seismic attribute is any measurement extracted direct or indirectly from the seismic data that help us better visualize or quantify features of interpretation interest. Broadly speaking, seismic attributes fall into two categories: morphological- and reflectivity-related attributes. The morphological attributes give us an understanding about the reflector dip, azimuth, and terminations, which can in turn be associated with faults, fractures, channels, carbonate buildups and karsts. The reflectivity attributes help us to extract information on reflector amplitude, waveform, and variation related to illumination angle, which can in turn be associated to lithology, reservoir thickness, and presence of hydrocarbon.

Time-frequency (TF) analysis or general spectral decomposition (SD) is a specific technique that plays in these two broad fields, i.e., it can be used either on morphological (geometrical) and reflectivity (physical) based approaches. Analyzing the time-frequency characteristic of seismic traces can give important insights from the complex structure of the "multi-layered" signal consisting of several components that occurs as consequence of the variety of geological features. Some of its usefulness include structural and seismic stratigraphy interpretation, denoising (ground roll, 50- or 60-Hz cultural noise, high-frequency random noise), thin-bed and channels characterization, time-frequency-based attenuation analysis, and direct hydrocarbons detection to mention a few.

There are a variety of time-frequency analysis algorithms and approaches to access and characterize the frequency behavior of a given signal, but overall they can be categorized into linear, quadratic (bilinear), and non(bi)linear methods. In linear methods, the analyzed signal is characterized by its inner products (or cross-correlation) with a pre-defined family of templates. The most known example of linear method is

the windowed Fourier transform, which is generated by translating and modulating a basic window function. Improvement on the resolution of the windowed Fourier transform was one of the motivations behind the development of other techniques for the analysis of nonstationary signals, such as the continuous wavelet transform (CWT) (Grossmann and Morlet, 1984; Chakraborty and Okaya, 1995), S-transform (Stockwell et al., 1996), synchrosqueezing transform (Daubechies et al., 2011), and matching pursuit (Mallat and Zhang, 1993; Wang, 2007). Because these methods use templates functions to access the TF content of the signal, invariably they "colors" the representation and can influence the interpretability of the signal properties. Additionally, and again because the templates functions, these methods are limited by the Heisenberg uncertainty, which affect the resolution attained in the TF representation. In quadratic methods, one can avoid the use of functions templates to build the TF representation. The Wigner-Ville distribution (WVD) is an example of such approach. In this case, a "more-focused" TF representation can be achieved. However, interference terms from multicomponent or nonlinear frequency modulated signals arise rendering a more complicate TF representation and interpretation. Although these interference terms can be handled by further processing with smoothed kernel, it reintroduces the blurring in the TF representation. Additionally, signal reconstruction in quadratic methods is not as straightforward as in linear methods. Other examples of quadratic methods include the smoothed pseudo-Wigner-Ville distribution (SPWVD) (Franz et al., 1995) the Choi-Williams distribution (CWD) (Choi and Williams, 1989) and the Wigner-Ville maximum entropy method (WV-MEM) (Zoukaneri and Porsani, 2015). The Empirical Mode Decomposition (EMD) method (Huang et al., 1998) is a nonlinear method, an alternative that would allow TF analysis of multicomponent signals without the weaknesses sketched above, overcoming the artificial spectrum spread caused by sudden changes. The EMD algorithm received more robust and versatile extensions, given rise to the ensemble EMD (EEMD) (Wu and Huang, 2009), the complete ensemble EMD with adaptive noise (CEEMD) (Torres et al., 2011), and more recently to an improved version of CEEMD (ICEEMD) (Colominas et al., 2014). With the exception of the last one (ICEEMD), the applicability and usefulness of the EMD-based methods to seismic time-frequency analysis are demonstrated and compared in Han and van der Ban (2013).

From the lines drawn above, it is clear that the variety of TF frequency methods combined with the variety of seismic attributes that can be computed from the TF

representations lead to wide range of possibilities to the final goal of proving and supporting the geoscientist with some new information and different insights from the geology under study. Although this complexity and the intrinsic limitation of each method, time-frequency joint seismic attributes has proven its value in the understanding the geology hidden in the seismic data. The present work is an attempt to move a step further on this direction. Rather than a comparative study of which TF representation is best suitable to seismic signal analysis, I am focused on understand where some established techniques in the literature have stopped, and propose new ideas to overcome their limitations. To this finality, I present this work in the form of scientific papers in order to document and transfer the technology I have applied or developed. Chapters 2 and 3 are published in the "seismic attributes" special section of the SEG Interpretation journal. Chapter 4 and 5 are in press for publication in SEG Interpretation journal and will be published in February 2017 as a technical paper and in "Seismic time-frequency analysis" special section, respectively.

In chapter 2, by using higher order statistics, I address the complexity on handling the iso-frequency volumes generated from seismic spectral decomposition.

In chapter 3, the technique proposed in chapter 2 is applied jointly with sweetness and discontinuity detection attributes in an integrated workflow.

In chapter 4, I propose a combination of the "Differential Resolution", a spectral enhancement technique, with the computation of discontinuities at different spectral bands.

In chapter 5, I bring an EMD-based technique proposed in biomedical signal processing to the context of seismic signal analysis.

Finally, in Chapter 6, I present my conclusions and recommendations.

REFERENCES

Chakraborty, A. and Okaya, D., 1995, Frequency-time decomposition of seismic data using wavelet based methods: Geophysics, 60, 1906–1916.

Choi, H. I. and Williams, W. J., 1989, Improved time-frequency representation of multi-component signals using exponential kernels: IEEE Transactions on Acoustic and Speech Signal Process, 37, 862–871.

Chopra, S. and Marfurt, K. J., 2005, Seismic attributes — A historical perspective: Geophysics, 70, 3SO–28SO.

Chopra, S. and Marfurt, K. J., 2007, Seismic attributes for prospect identification and reservoir characterization. SEG.

Colominas, M. A., Schlotthauer, G. and Torres, M. E., 2014, Improved complete ensemble EMD: A suitable tool for biomedical signal processing: Biomedical Signal Processing and Control, 14, 19-29.

Daubechies, I., Lu, J. and Wu, H.-T., 2011, Synchrosqueezed wavelet transforms: An empirical mode decomposition-like tool: Applied and Computational Harmonic Analysis, 30(2), 243–261.

Franz, H., Manickam, T. G., Urbanke, R. L. and Jones, W., 1995, Smoothed pseudo-Wigner distribution, Choi-Williams distribution, and cone-kernel representation: Ambiguity analysis and experimental comparison: Signal Processing, 43, 149–168.

Grossmann, A. and Morlet, J., 1984, Decomposition of Hardy functions into square integrable wavelets of constant shape: SIAM Journal on Mathematical Analysis, 15, 723–736.

Han, J. and van der Baan, M., 2013. Empirical mode decomposition for seismic time-frequency analysis: Geophysics, 78(2), O9-O19.

Huang, N. E., Z. Shen, S. R. Long, M. C. Wu, H. H. Shih, Q. Zheng, N.-C. Yen, C. C. Tung, H. H. Liu,1998. The empirical mode decomposition and the Hilbert spectrum for nonlinear and non-stationary time series analysis: Proceedings of the Royal Society A Mathematical Physical and Engineering Sciences 454 (1971), 903–995.

Mallat, S. G. and Zhang, Z., 1993, Matching pursuit in a time-frequency dictionary: IEEE Transactions on Signal Processing, 41, 3397–3415.

Stockwell, R. G., Mansinha, L. and Lowe, R. P., 1996, Localization of the complex spectrum: The S-transform: IEEE Transactions on Signal Processing, 44, 998–1001.

Taner, M. T., Koehler, F., E. and R., S., 1979. Complex seismic trace analysis: Geophysics, 44(6), 1041–1063.

Torres, M., Colominas, M., Schlotthauer, G. and Flandrin, P., 2011, A complete ensemble empirical mode decomposition with adaptive noise: IEEE International Conference on Acoustics, Speech and Signal Processing (ICASSP), 4144–4147.

Walden, A., 1985, Non-Gaussian reflectivity, entropy, and deconvolution. Geophysics, 50, 2862–2888.

Wang, Y., 2007, Seismic time-frequency spectral decomposition by matching pursuit: Geophysics, 72(1), V13–V20.

Wu, Z. and Huang, N. E., 2009, Ensemble empirical mode decomposition: A noise-assisted data analysis method: Advances in Adaptive Data Analysis, 1(1), 1–41.

Zoukaneri, I. and Porsani, M. J., 2015, A combined Wigner-Ville and maximum entropy method for high-resolution time-frequency analysis of seismic data:Geophysics, 80(6), O1–O11.

CHAPTER 2: INDEPENDENT COMPONENT SPECTRAL ANALYSIS

Bruno César Zanardo Honório[1], Alexandre Cruz Sanchetta[2], Emilson Pereira Leite[1] and Alexandre Campane Vidal[1]

[1] University of Campinas – UNICAMP, Department of Geology and Natural Resources, Campinas, Brazil; E-mail: brunohonorio@gmail.com; emilson@ige.unicamp.br; vidal@ige.unicamp.br

[2] State University of Campinas – UNICAMP, Department of Petroleum Engineering, Campinas, Brazil; E-mail: alexandr@dep.fem.unicamp.br

This paper was published by SEG journal Interpretation in 2014.

ABSTRACT

Spectral decomposition techniques can break down the broadband seismic records into a series of frequency components that are useful for seismic interpretation and reservoir characterization. However, it is laborious and time-consuming to analyze and to interpret each seismic frequency volume taking all the usable seismic bandwidth. In this context, we propose a multivariate technique based on independent component analysis (ICA) with the goal of choosing the spectral components that best represent the whole seismic spectrum while keeping the main geological information. The ICA based method goes beyond the Gaussian assumption and takes advantage of higher order statistics to find a new set of variables that are independent of each other. The independence between two components is a more general statistical concept than the non-correlation and, in principle, allows the extraction of more significant information from the data. We have tested four different contrast functions to estimate the independent components (ICs), which we could verify a better channel system identification depending on the contrast function used. By stacking the ICs in the red-green-blue color space, we could represent the main information in a single and good quality image. To illustrate the proposed method, we have applied it to a seismic volume which was acquired over the F3 block in the Dutch sector of the North Sea. We also compared the results with those obtained by principal component analysis. In this case, the ICA based method could generate a better image and faithfully delineate a channel system presented in the studied seismic volume.

INTRODUCTION

Spectral decomposition is an effective method for signal analysis, and is commonly used to generate seismic attributes for reservoir characterization. By transforming the data into the frequency domain, it often reveals many features that are hidden or not properly seen in the time domain, which makes it an important tool for seismic processing and interpretation (Chakraborty and Okaya, 1995).

Several works have reported that spectral analysis is useful as a direct hydrocarbons indicator (Sun et al., 2002; Wang, 2007; Li et al., 2011), as well as in reservoir characterization (Partyka et al., 1999; Matos et al., 2005; Liu and Marfurt, 2007a; Matos et al. 2012; Davogustto et al., 2013; Wallet, 2013). A common way to analyze seismic data in the spectral domain is by searching through each frequency component, in order to determine which single frequency component best represents a particular feature of interest (Guo et. al, 2009). Although the frequency transformation is useful, an interpreter may generate and analyze dozens of isofrequency volumes using the seismic bandwidth. Therefore, it is useful to develop effective ways to represent and visualize such transformed data.

A considerable effort has been made to find a better way for frequency representation. Particularly, the red-green-blue (RGB) color display technique plays an important role in the visualization of frequency components (Stark, 2006; Henderson et. al, 2007; Liu and Marfurt, 2007b; Guo et al.,2009; McArdle and Ackers, 2012). Guo et. al, (2009) applied the principal component analysis (PCA) to reduce the redundancy of the spectral decomposed seismic record, ranking the variance of the data. Then, using the three channels of the RGB color display and the three first principal components, more than 80% of the spectral variability could be represented in a single image.

The PCA technique, however, is based only on the variance and covariance of the data. The uncorrelatedness obtained by PCA is just a weaker form of independence (Hyvärinen and Oja, 2000). Unlike PCA, ICA deals with higher-order statistics, which, in principle, assigns more information to the components. In this way, ICA can be seen as an extension of PCA (Hyvärinen et al., 2001). While the PCA decorrelates the input data, ICA separates the remaining higher-order dependencies (Draper et al., 2003). Another comparison between the two methods is that PCA assumes the signal as Gaussian distributed, whereas ICA assumes that the signal is non-Gaussian distributed (Lu, 2006). Considering that the seismic data can be viewed as signals with super-

Gaussian distributions, i.e., with positive kurtosis (Walden, 1985) and, therefore, non-Gaussian, this assumption fits the fundamental assumption of ICA.

In this study, we propose a technique based on ICA to select those frequency features that best represent the entire seismic spectrum. To do so, we briefly present a different implementation of the continuous wavelet transform (CWT) used to generate the seismic frequency volumes; the mathematical fundamentals of ICA and the strategy for ICs visualization. We then test the proposed technique by applying it to the F3 block in the Dutch sector of the North Sea. Finally, we compare the ICA results with composite images obtained from the PCA technique.

THEORY AND METHOD

Spectral Decomposition

Spectral decomposition or time-frequency analysis of a seismic record is utilized to characterize the time-dependent frequency response of subsurface rocks and reservoirs (Sinha et al., 2005).

Since it is a non-unique process, there are various methods to perform the time-frequency analysis of nonstationary signals. Among them, the time-frequency continuous wavelet transform (TFCWT, Sinha et al. 2005) responds with an optimal time-frequency resolution and, therefore, it is a useful approach to seismic data analysis. The TFCWT takes the Fourier transform of the inverse continuous wavelet transform. Mathematically, the operation can be represented as the inner product between the wavelet transform of the signal $Wf(\sigma,\tau)$ (i.e., the scalogram or time-scale map) and the wavelet as an adaptive window $\widehat{\Psi}_{\omega}(\sigma)$:

$$\hat{f}\,(\omega,\tau) = \langle Wf(\sigma,\tau), \widehat{\Psi}_{\omega}(\sigma)\,\rangle. \tag{1}$$

The adaptive window $\widehat{\Psi}_{\omega}(\sigma)$ means that for a particular scale σ, we have a determined frequency ω and vice-versa, and it is represented as:

$$\overline{\widehat{\Psi}}_{\omega}(\sigma) = \frac{\widehat{\Psi}(\sigma\omega)e^{-i\omega\tau}}{C_{\Psi}\sigma^{3/2}}, \tag{2}$$

where C_{Ψ} is a constant for wavelet Ψ and τ is the time-shifting parameter. The function $\overline{\widehat{\Psi}}_{\omega}(\sigma)$ is the complex conjugate of the mother wavelet in the frequency domain $\widehat{\Psi}_{\omega}(\sigma)$. For a detailed discussion on TFCWT and how it is implemented, see Sinha et al. (2005). Note that other spectral decomposition method can be applied. The main concern of the article is how to better deal with large frequency volumes that can be produced by

spectral decomposition techniques. However, the choice of a spectral decomposition technique should always require improved information on the spectral content of the seismogram.

The Morlet wavelet (Figure 1a) is the function commonly used in CWT. It is based on a complex exponential modulated by a Gaussian envelope (Morlet et al., 1982). Mathematically, it is expressed as (Torrence and Compo, 1998):

$$\Psi_0(t) = \pi^{-\frac{1}{4}} e^{\omega_0 it} e^{-\frac{t^2}{2}}, \tag{3}$$

where t the is time parameter and ω_0 is the frequency taken as 2π to satisfy the admissibility condition (Farge, 1992; Sinha et al., 2005). The time-frequency map of a seismic signal adopting TFCWT and the isofrequency volumes generation can be represented as show in Figure 2. 1:

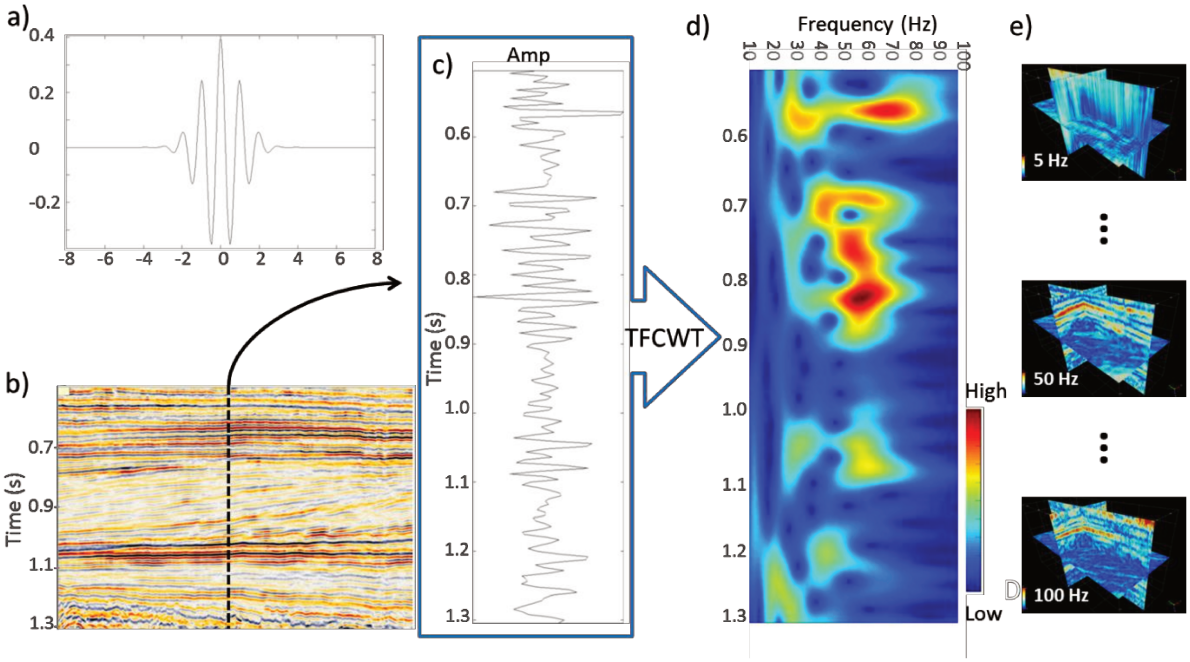

Figure 2. 1: TFCWT: (a) Real part of the Morlet mother wavelet; (b) Seismic section and the selected trace in (c); (d) Magnitude spectrum. The procedure is repeated for all traces and the isofrequency volumens are built (e).

Definition of ICA

The ICA approach is directly related to projection pursuit (Huber, 1985), which is a statistical technique for finding "interesting" projections of multidimensional data. In turn, such projections are useful for optimal data visualization. Huber (1985) argued that the least Gaussian distributions are the ones with the most interesting directions, which is what we do for estimating the ICA model. For example, Figure 2. 2a shows three different kinds of distribution while Figure 2. 2b illustrates the usefulness of

finding the projection pursuit direction. In this case, such direction is horizontal and we can identify the clustered structure of the data. It is also important to note that the projection on the first principal component, i.e., the direction of maximum variance is vertical and would not show the clustered structure.

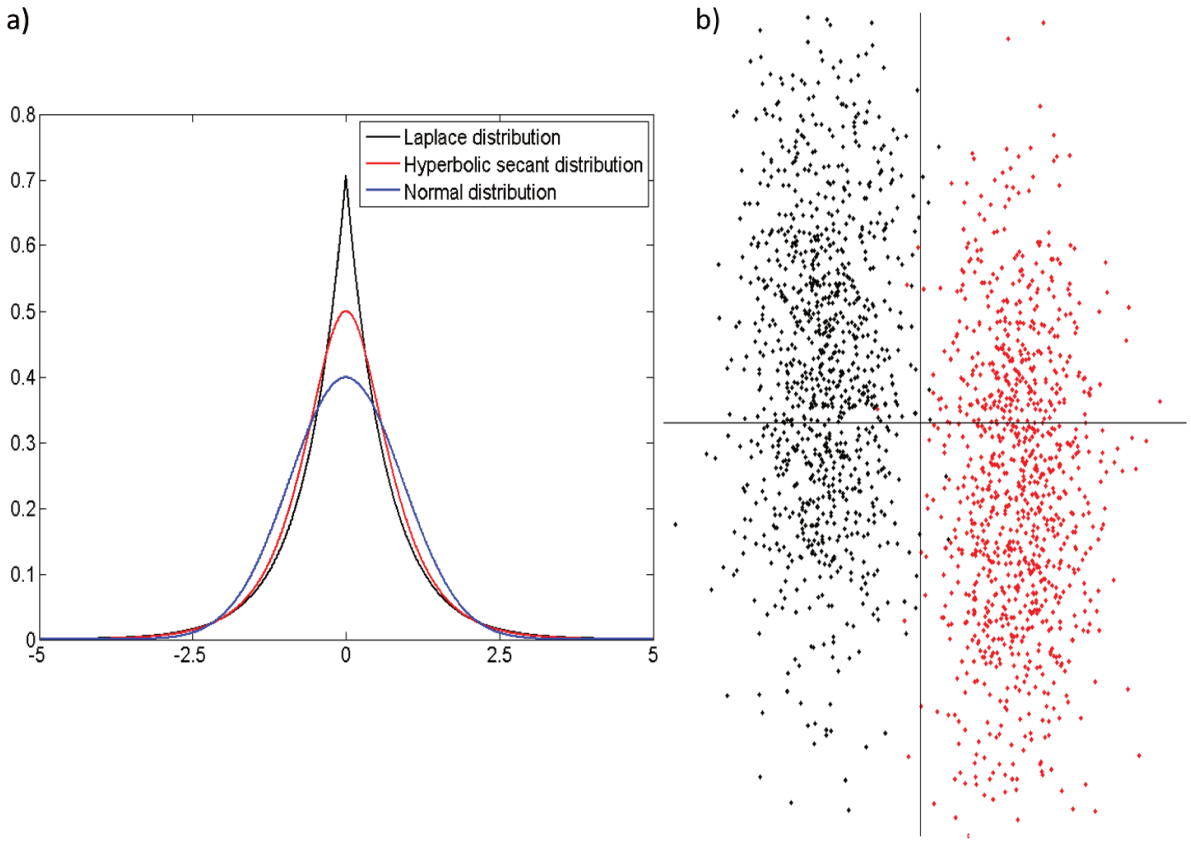

Figure 2. 2: (a) Probability distribution of the Laplace, Hyperbolic secant and Normal distributions. The excess kurtoses are equals to 3, 2 and 0 respectively; (b) Illustration of the projection pursuit. The non-Gaussian projection pursuit direction is horizontal and clearly shows an optimal cluster separation. The variance-based methods like PCA would fail, not recognizing the two clusters (modified from Hyvärinen and Oja, 2000).

The idea of applying the ICA method to seismic frequency components comes from its application in image processing of natural color and stereo images (Hoyer and Hyvärinen, 2000). In this case, ICA is used to extract features that can be used in denoising, compression and pattern recognition. In our case, we intend to extract the spectral response that can better delineate seismic features associated with different geologic features. Using a vector-matrix form, the ICA model can be formulated as follows:

$$\mathbf{x} = \sum_{i=1}^{m} \mathbf{a}_i s_i = \mathbf{A}\mathbf{s}, \tag{4}$$

where **x** is an observed *m*-dimensional vector that represents the multiple spectral components of the seismic data in our case, and **s** is the signal source vector (or ICs) whose components are taken as mutually independent. The ICs can be viewed as the spectral response of different types of geologic features weighted by the unknown mixing matrix **A**.

A common issue in statistical signal processing & neural networks is to find a transformation that provides some desired feature from the input data. For simplicity, such representation is commonly taken as a linear transformation of the original data. In the special case of ICA, the linear transformation is performed by a weight matrix **W**, which estimates the signal source vector ***s'*** as a set of scalar sources that are statistically and mutually independent:

$$\boldsymbol{s'} = \sum_{\boldsymbol{i=1}}^{\boldsymbol{m}} \boldsymbol{w_i}\, \mathrm{x_i} = \mathbf{Wx}. \qquad (5)$$

So, the goal of an ICA algorithm is to find a matrix **W** that maximizes the independence between each estimated source s'_i. Here **s'** denotes the estimated **s**. However, in order to make the problem of IC estimation simpler and better constrained, some processing is usually very useful before applying an ICA algorithm to the data (Hyvärinen and Oja, 2000).

Preprocessing

The first step is to center the data ($\mathbf{x'} \equiv \mathbf{x} - \overline{\mathbf{x}}$), so that a zero-mean variable is obtained. Here, $\overline{\mathbf{x}}$ is the mean of **x**. Consequently, $\mathbf{s'}$ is also a zero-mean variable. The aim of the zero-mean step is to simplify the ICA algorithm and subsequently the mean can be added at the final stage.

The second step is the sphering transformation (also known as whitening; not to be confused with spectral whitening), which removes the second order statistical dependence in the data. This can be done by transforming linearly the observed vector **x'** to obtain a new vector **z** whose components are uncorrelated and their variances equal unity:

$$\mathbf{z} = \mathbf{V}\mathbf{x'}, \qquad \text{so that} \qquad E\{\mathbf{z}\mathbf{z}^T\} = \mathbf{I}, \qquad (6)$$

where **z** the sphered data, **V** is the sphering matrix, and $E\{.\}$ the expectation function.

The transformation given by equation 6 is always possible. In fact, it can be performed by PCA using the eigenvalue decomposition (EVD) of the covariance matrix

$\mathbf{C_x}' = \mathbf{U}\,\boldsymbol{\lambda}\,\mathbf{U}^T$. Here, $\mathbf{U}$ is the orthogonal matrix of eigenvectors of $\mathbf{C_x}'$ and $\boldsymbol{\lambda}$ denotes the diagonal matrix of its eigenvalues, i.e., $\boldsymbol{\lambda}$ = diag (λ_1, ..., λ_n). Hence, we have $\mathbf{V_{PCA}}=\boldsymbol{\lambda}^{-1/2}\mathbf{U}^{\mathrm{T}}$, so that:

$$\mathbf{z} = \mathbf{V_{PCA}}\mathbf{x}', \tag{7}$$

where $\boldsymbol{\lambda}^{-1/2} = \mathrm{diag}\left(\lambda_1^{-1/2}, \ldots, \lambda_n^{-1/2}\right)$.

The formulation as stated above makes a direct connection with the final and useful preprocessing step, which can be performed as sphering takes place: the dimension reduction (DR) of the data. The DR acts as a denoising procedure and prevents over-learning from happening during ICA (Hyvärinen et al., 1999). To do so, we analyze the eigenvalues of the covariance matrix and discard those that do not represent significant information. This step enhances the ICA performance by discarding small trailing eigenvalues and reduces computational complexity (compute time and memory consumption) by minimizing pair-wise dependencies (Liu and Wechsler, 1999; Hoyer and Hyvärinen, 2000).

The preprocessing steps can be synthesized as follow:

$$\mathbf{s}' = \mathbf{W}\mathbf{x} \xrightarrow{\textbf{centering}} \mathbf{W}\mathbf{x}' \xrightarrow{\textbf{sphering}} \mathbf{W}\mathbf{z} \xrightarrow{\textbf{PCA solution}} \mathbf{W}\mathbf{V_{PCA}}\mathbf{x}' \xrightarrow{\textbf{DR}} \mathbf{W}\boldsymbol{\lambda}_{\boldsymbol{n}}^{-\frac{\mathbf{1}}{\mathbf{2}}}\mathbf{U}_{\boldsymbol{n}}^{\mathbf{T}}\mathbf{x}',$$

where the n-th largest eigenvalues are represented by the diagonal matrix $\boldsymbol{\lambda}_n$ and $\mathbf{U}_n$ is the corresponding eigenvector matrix.

Because there is no easy way for thresholding the eigenvalues, we adopt an empirical and quantitative approach for DR. The eigenvalue that accounts for less than 1% of the accumulated eigenvalues is set as threshold. Figure 2. 3 illustrates the preprocessing workflow for the FastICA (Hyvärinen and Oja, 1997), as explained below.

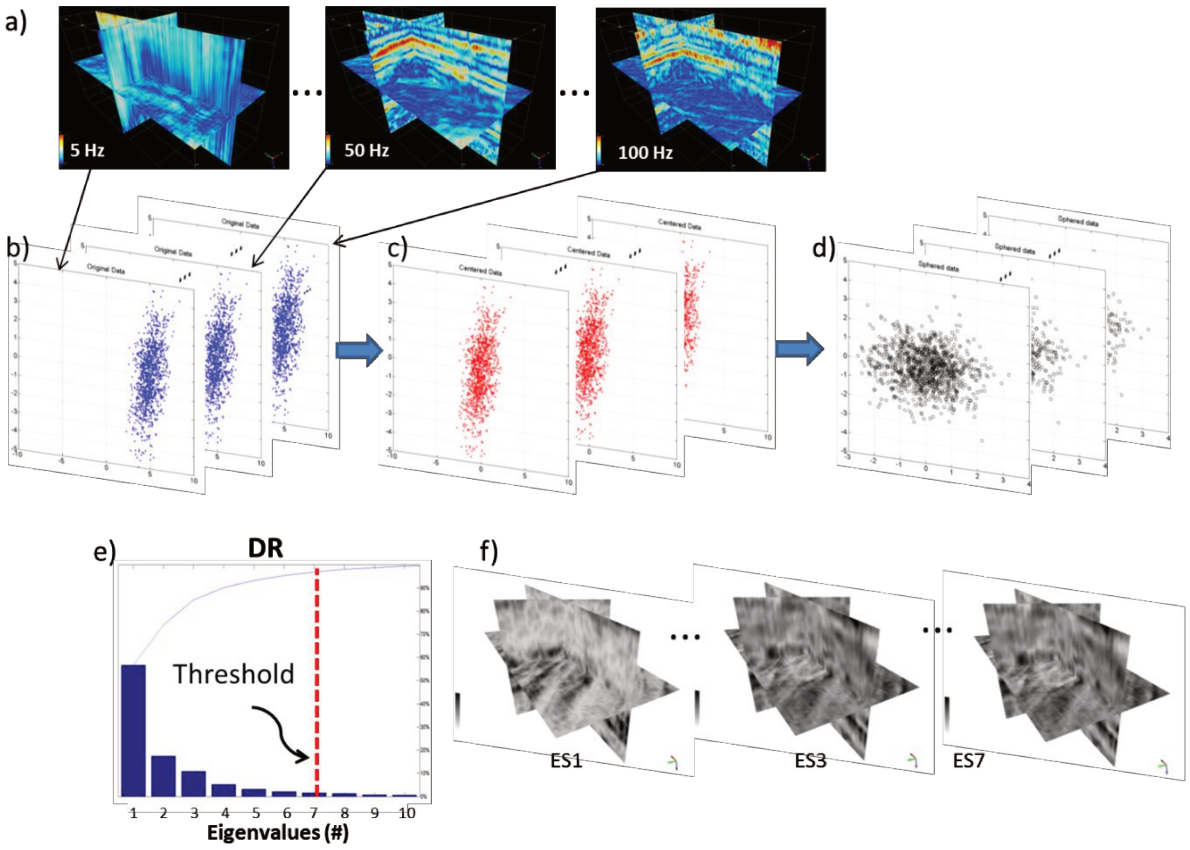

Figure 2. 3: Preprocessing steps for FastICA. (a) Seismic frequency volumes generated in intervals of 5 Hz and its representation in (b); (c) centered data; (d) sphered data; (e) eigenvalues measuring the amount of data variability represented by their corresponding eigenspectra (ES) shown in (f). The red dashed line in (e) shows the thresholded dimension.

ICs estimation

Taking the preprocessed data, ICA aims at finding a linear transformation **W** that minimizes the statistical dependencies between each estimated source s'_i (Hoyer and Hyvärinen, 2000). Although there may not be a closed form expression to find a **W** with such desirable property, the ICA algorithms use non-Gaussianity based criteria to find ICs (Hyvärinen et al., 2001). These algorithms iteratively approximate **W** in a such way that the independence is maximized.

Kurtosis and negentropy are two different measures of non-Gaussianity. Since in practice the probability density function (pdf) is unknown, ICA based on kurtosis could be sensitive to outliers (Huber, 1985) making it not robust enough as a measure of non-Gaussianity (Hyvärinen and Oja, 2000). On the other hand, we can use an approximation of the negentropy J as our objective (contrast) function to measure the non-Gaussianity of a random variable $y = \mathbf{w}^T\mathbf{z}$. It is expressed as (Hyvärinen, 1999b):

$$J_G(y) = [E\{G(y)\} - E\{G(v)\}]^2, \quad (8)$$

for some non-quadratic function *G* and standardized variable v. Equation 8 is always non-negative and equals zero for Gaussian-distributed *y*. In this way, based on the maximum-entropy principle, the ICA method represents an optimization problem in which the contrast function should be maximized.

To do that, we use a fixed-point algorithm, namely FastICA (Hyvärinen and Oja, 1997). In FastICA, ICs can be extracted successively one after another (deflation or the one-unit algorithm) or simultaneously (symmetric algorithm). We adopt the symmetric-based FastICA approach because the deflationary method has the drawback that estimation errors in the first vectors are accumulated in the subsequent ones, whereas the symmetric orthonormalization approach enables parallel computation of independent components (Hyvärinen et al., 2001).

Basically, each algorithm iteration updates each row $\mathbf{w}_i^{\mathrm{T}}$ of $\mathbf{W}$ by:

$$\mathbf{w}_i{}^{\boldsymbol{updated}} \leftarrow E\{\mathbf{z}\mathrm{g}(\mathbf{w}_i^{\mathrm{T}}\mathbf{z})\} - E\{\mathrm{g}'(\mathbf{w}_i^{\mathrm{T}}\mathbf{z})\}\mathbf{w}_i,$$

$$\mathbf{w_i} \leftarrow \mathbf{w_i}{}^{\boldsymbol{updated}} / ||\mathbf{w_i}{}^{\boldsymbol{updated}}|| \,.$$

The steps are repeated until convergence. To prevent different components from converging to the same maxima, we apply a symmetric decorrelation, e.g., by the classical method involving matrix square roots, which does not "privileges" any component (Hyvärinen and Oja, 2000). The decorrelation is done by applying EVD to the inverse square root matrix $(\mathbf{WW^T})^{-1/2}$. Then, we set $\mathbf{W}^{\boldsymbol{dec}} \leftarrow (\mathbf{WW^T})^{-1/2}\mathbf{W}$ (Hyvärinen and Oja, 2000), where $\mathbf{W}^{\boldsymbol{dec}}$ is $\mathbf{W}$ decorrelated.

The expectations for FastICA, in practice, must be replaced by their estimates, and the natural choice is the corresponding sample means (Hyvärinen and Oja, 2000). In the algorithm iteration, g is the derivative of G, and g' is its second derivative. We tested four different contrast functions commonly used in FastICA algorithm:

$$\mathrm{G}_1(y) = \frac{1}{3}y^3, \tag{9}$$

$$G_2(y) = \frac{1}{4}y^4, \tag{10}$$

$$G_3(y) = \mathrm{logcosh}(y), \tag{11}$$

$$G_4(y) = -e^{(-y^2/2)}, \tag{12}$$

Practically any non-quadratic function G can be used to perform ICA. However, choosing G that does not grow too fast, one can obtain estimators that are more robust. In particular, the contrast functions using G_3 and G_4 have proved to be very useful

(Hyvärinen and Oja, 2000). In Figure 2. 4, we illustrate the behavior of the functions G used in our study.

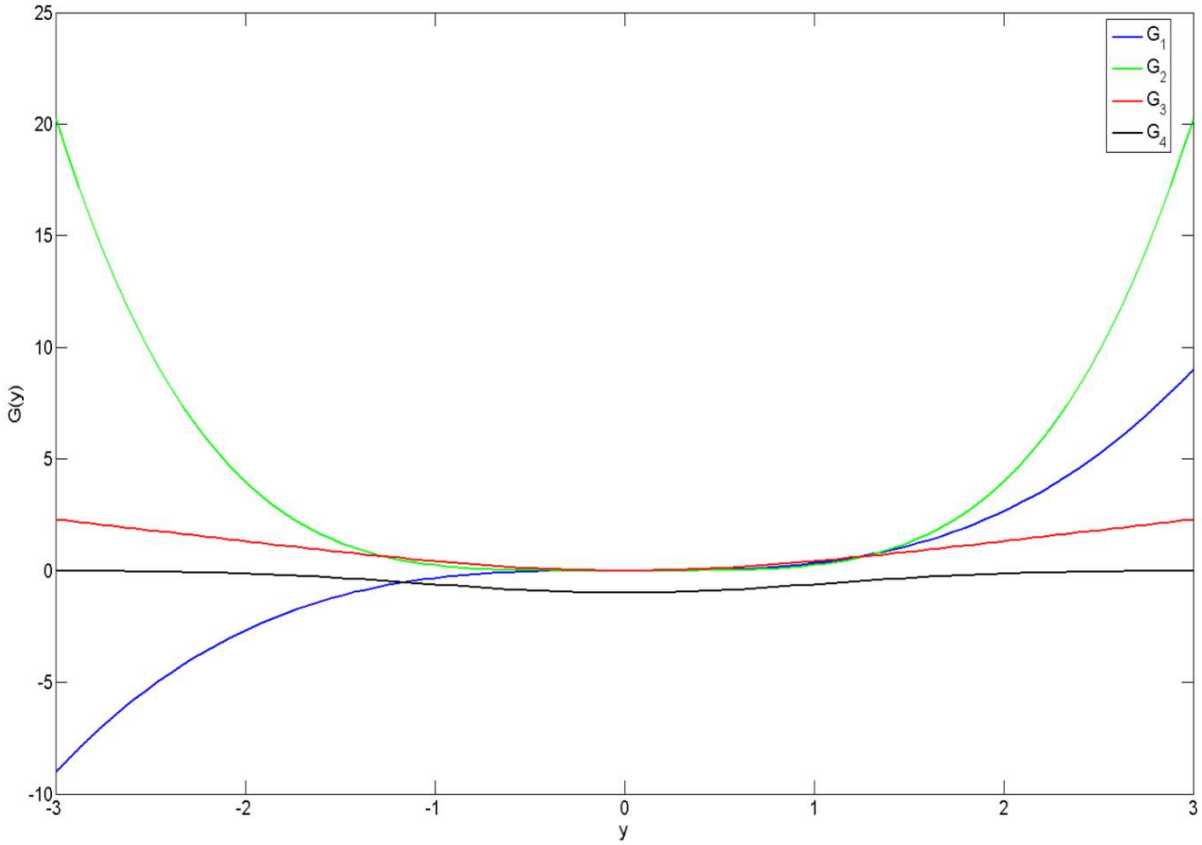

Figure 2. 4: Contrast functions used in FastICA.

Visualization of ICs

The RGB color blending is a powerful technique for visualization of the spectral decomposed seismic data (McArdle and Ackers, 2012). However, the choice of which frequencies components to be used is often an empirical task and a considerable amount of information may be lost. Additionally, depending on the frequency combination, the visualization does not show a significant difference (Guo et al., 2009). Different approaches have been proposed to better deal with the frequency components of the seismic data at the RGB color space (Stark, 2006; Liu and Marfurt, 2007b; Guo et al., 2009).

In our study, we extend the idea of Guo et al., (2009) who used the RGB channels to display the principal components. Taking advantage of the statistical properties of ICA, we display the first three independent components against RGB color channels.

CASE STUDY - F3 DUTCH OFFSHORE DATA SET

The block F3 is an offshore zone located in the Dutch sector of the North Sea. The block was acquired to explore oil and gas in the Upper-Jurassic – Lower Cretaceous strata, which consist of deposits of a large fluviodeltaic system (Sørensen et al, 1997). The original F3 seismic dataset is rather noisy (Figure 2. 5a and Figure 2. 5b). In order to enhance laterally continuous events, a dip-steered median filter with a radius of two traces was applied to the data (Figure 2. 5c) (Chopra et al., 2011; Jibrin et al., 2013).

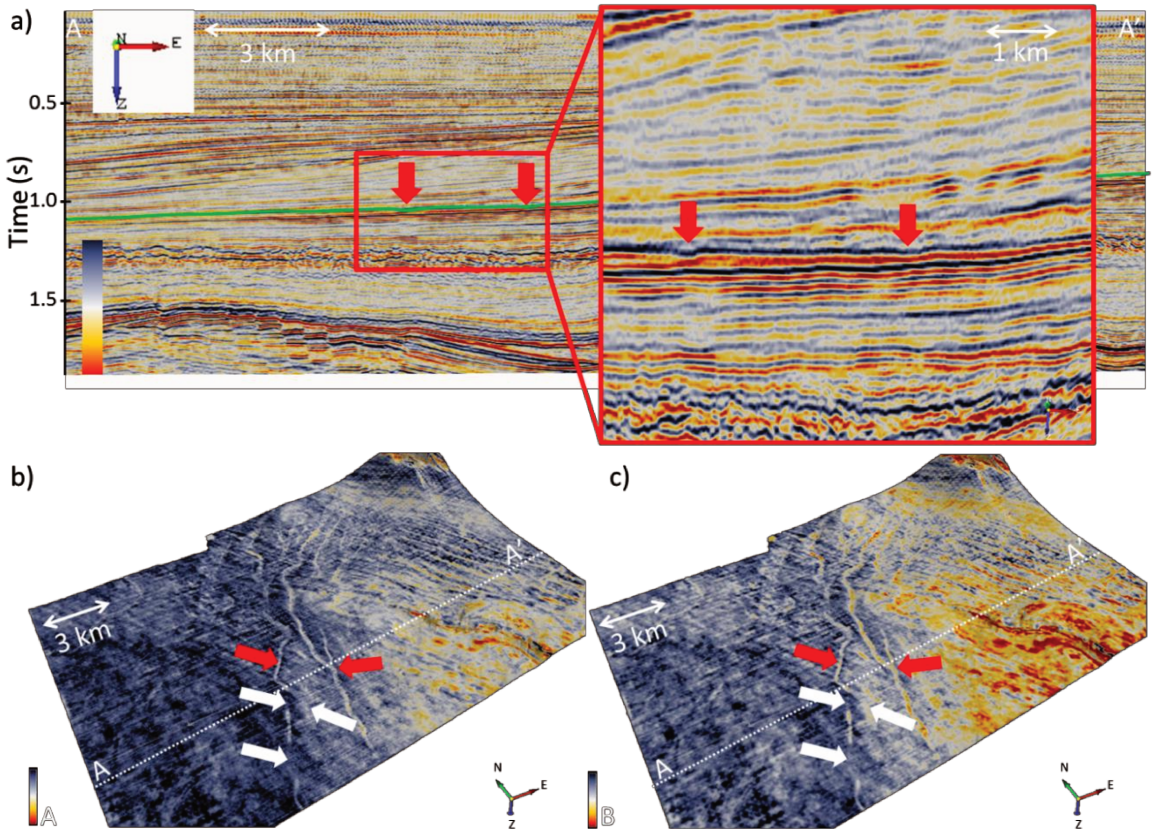

Figure 2. 5: Amplitude seismic volume from F3 Dutch offshore data set. (a) Vertical seismic section and the seismic horizon (green line) displayed in (b) Original data, and (c) Dip-steered median filtered data. The red arrows indicate the channel and white arrows indicate unclear features.

We can identify the channel system by the highlighted low amplitudes (red arrow). However, even analyzing the dip-steered median filtered data, we are unable to see the channel continuity and the entire geomorphology of the channel as the parts indicated by the white arrow.

Figure 2. 6 shows one of several possible frequency combinations to illustrate the conventional way of RGB color stack. The 20, 30 and 50 Hz components are used in this case. By doing this, we enhance the channel indicated by the red arrow and a

meandering channel (yellow arrow). However, the channel indicated by the black arrow is buried and its continuity is still hard to see. The rectangle indicates the area where the channel system is not clearly interpretable in amplitude domain as well as in the conventional RGB color stack. Therefore, our method is applied to the highlighted area.

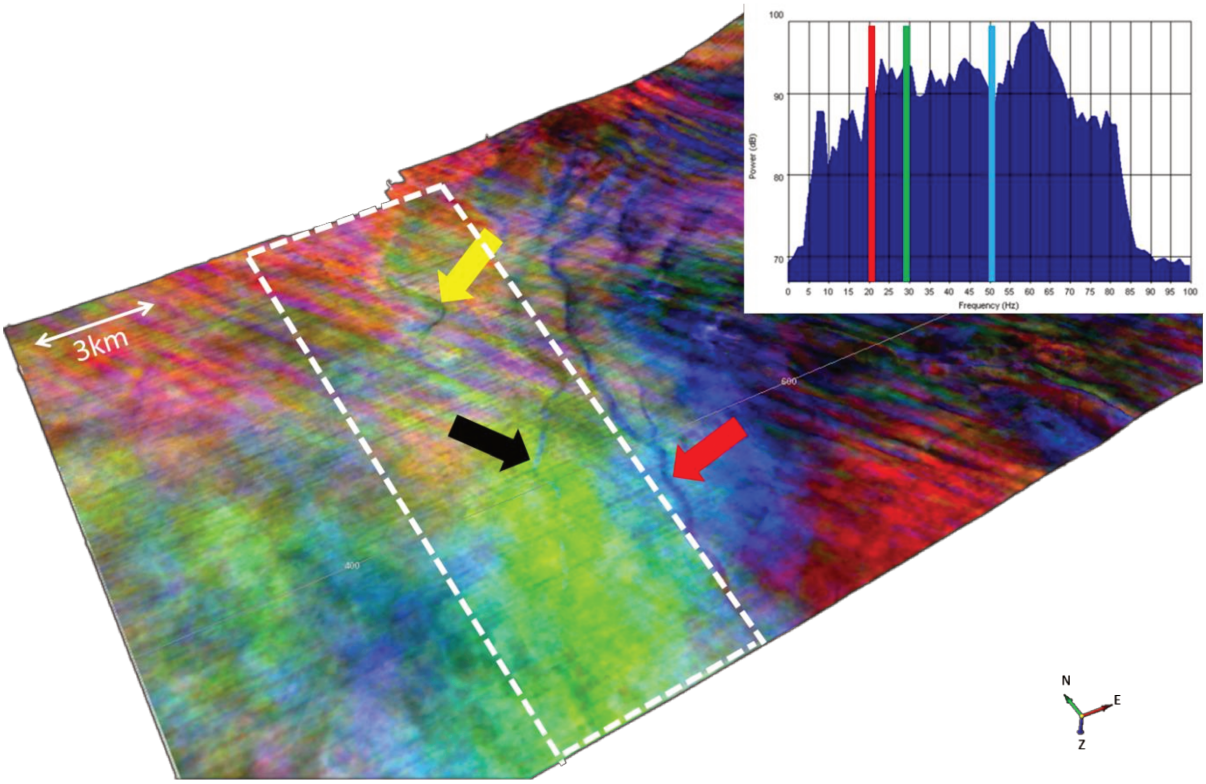

Figure 2. 6: RGB color stack of the 20, 30 and 50Hz spectral magnitude components. Upper right panel is the frequency spectrum of the data. The vertical lines represent the frequencies used in our analysis, a total of 20 isofrequency volumes. The studied area is highlighted by a white dashed line.

We begin our analysis by first evaluating the contribution of each eigenspectra (eigenvector) to be used in the DR. Based on the adopted criterion, the largest 7 of 20 eigenspectra having the largest eigenvalues are selected as our threshold.

Because the most coherent spectra are assigned to the first eigenvalues, the threshold keeps as much of the original signal content as possible. The incoherent spectral components assigned to the last eigenvalues are discarded. By retaining 7 eigenspetra we can represent 96.8% of the total variability of the data set. Therefore, the preprocessing step reduces the computational complexity and acts as a denoising procedure as well.

After DR, the outputs of FastICA are analyzed based on different contrast functions. Then, the first three independent components of each contrast function are taken to

visualize in the RGB color space (Figure 2. 7). Each independent component is assigned in one RGB channel.

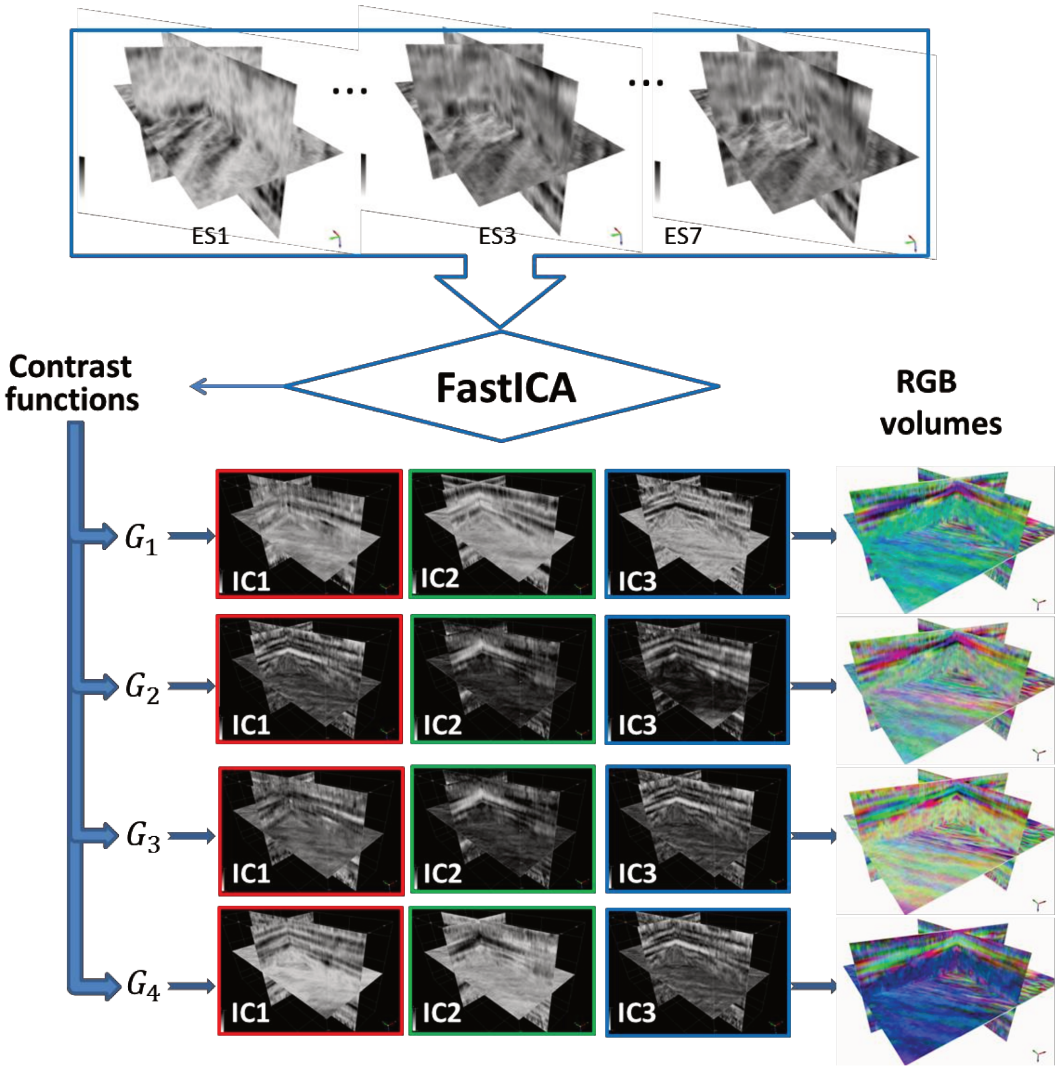

Figure 2. 7: Schematic FastICA diagram after preprocessing and RGB color stack. Top: First seven eigenspectra retained based on DR; Bottom: estimated ICs based on each contrast function G; Right: RGB composite volumes for each contrast function G.

The study area is shown in Figure 2. 8. Figure 2. 8a, shows that the ICs extracted using G_1 do not highlight properly the channel. However, the other three contrast functions provide satisfactory results. The red ellipses and yellow circles shows the channel parts that are better delineated using G_2, G_3 and G_4.

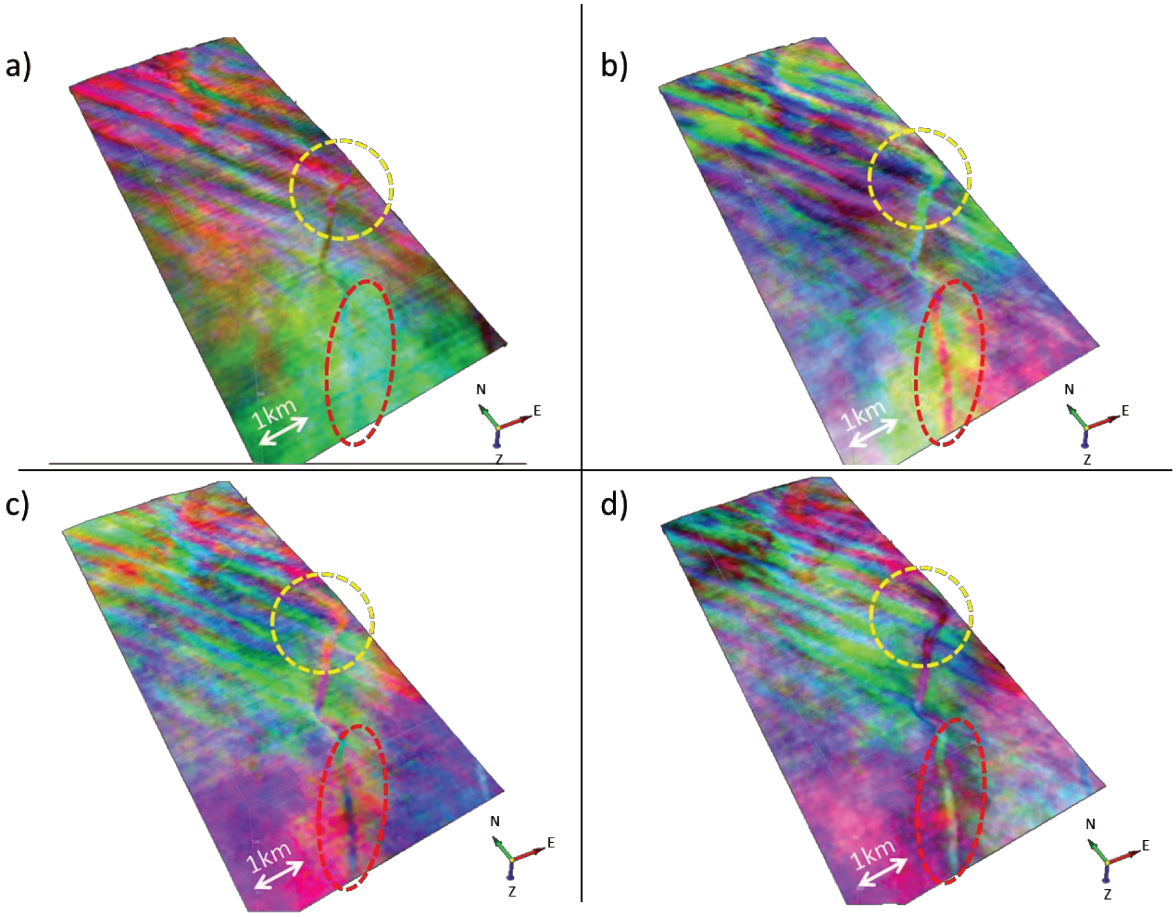

Figure 2. 8: RGB composite images of the ICs using different contrast functions:(a) G1; (b) G2; (c) G3 and (d) G4.

The results obtained by G_4 (i.e Figure 2. 8d) are then compared to those from PCA. The PCA response for the spectral components is shown in Figure 2. 9a and the ICA composite image is shown in Figure 2. 9b.

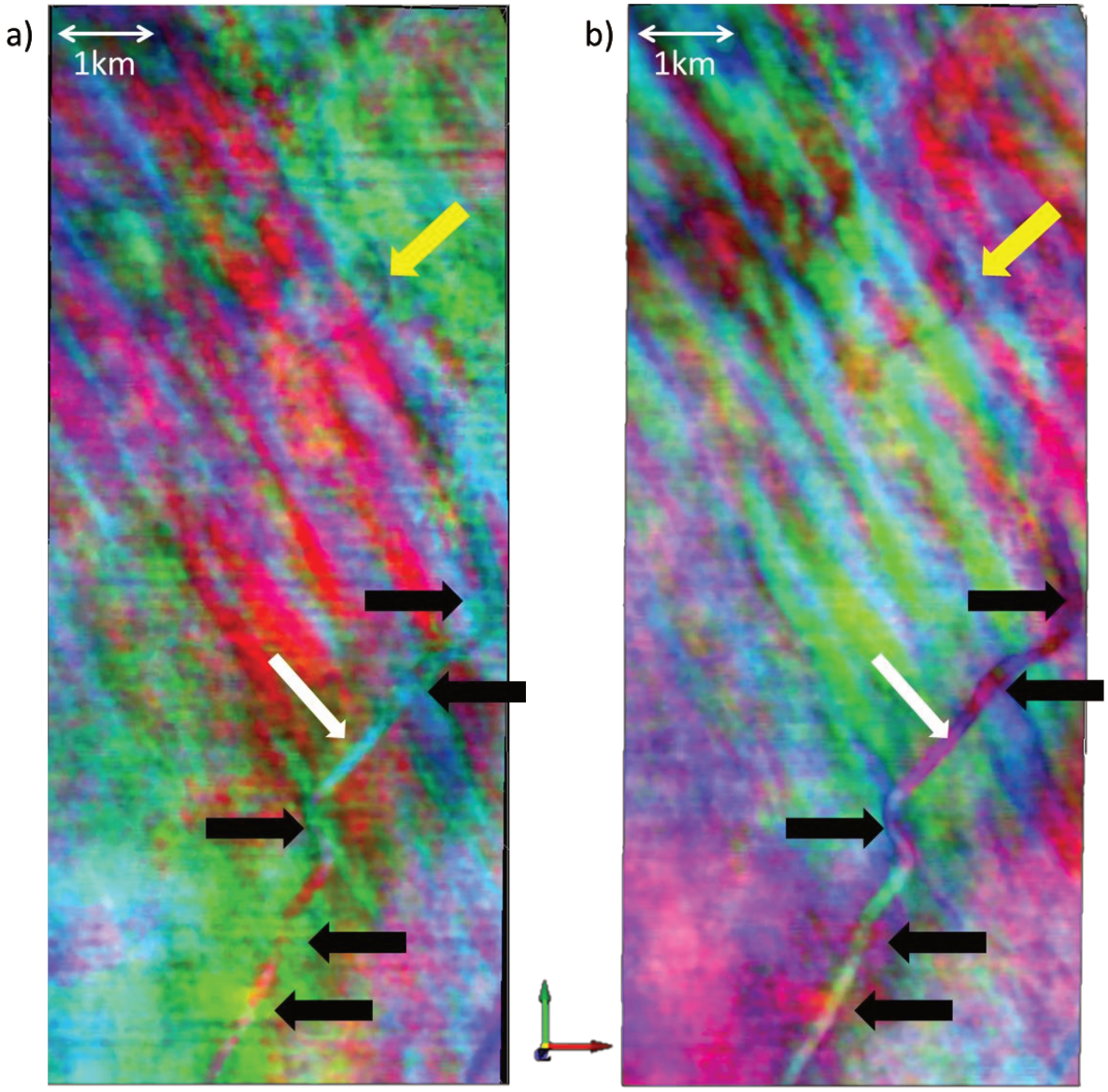

Figure 2. 9: Comparative analysis of the composite images. (a) PCA; (b) ICA.

We can see the highlighted channel (white arrow) on the southwest part of the horizon slice as well as a thin meandering channel (yellow arrow) on upper part of the horizon in both images. Although PCA could generate an interpretable image, some parts of the channel are poorly resolved when compared with the ICA image. The black arrows indicate such regions. The two right-pointed black arrows show the meandering characteristic of the channel, and the other three left-pointed black arrows show a continuity of the channel. In addition, it is important to note that the ICA image shows better acquisition footprint supression. Although the IC composite images are better for interpretation and provide superior results over the PCA based technique, there is no evidence at all of a direct connection between porosity thickness as provided by the original frequency components. In this way, ICs are as limited as PCs, the images

having to be qualitatively interpreted using principles of seismic geomorphology within a given depositional, erosional, or diagenetic framework, as pointed out by Guo et al. (2009). Another consideration is that, differently from PCA, which orders the principal components based on the eigenvalues, the independent components have no inherent order. Hyvärinen (1999b) suggested a technique for ordering the ICs using the norms of the mixing matrix **A** columns. We have tested this approach but we recommend analyzing each of the ICs before RGB color stack. Technically, the number of components set in DR limits the number of ICs. Fortunately, around 95% of the total variance was captured in 6 components for other dataset we have studied, even using 91 frequency volumes as input. Our results are based on taking the first three ICs of seven possible.

CONCLUSION

We have shown that ICA can be successfully applied in order to reduce the large data volume generated by the spectral decomposition process. By using the proposed workflow, the redundant frequency volumes could be reduced to a more manageable number of components. Taking advantage of the ICA statistical properties, we kept the most geologically pertinent information within the spectral decomposed data.

When compared with the PCA-based technique, the RGB images produced from ICs showed superior results and could better delineate the channel system present in the studied seismic volume.

Different approaches can be taken for dimensionality reduction. We recommend evaluating each of the extracted ICs in order to stack them in the RGB color space, although some criteria for ordering the ICs can be adopted.

ACKNOWLEDGMENTS

We would like to thank dGB Earth Sciences Company for providing the "OpendTtect" software used for seismic data visualization. Special thanks to Eric Bouanga from dGB Earth Sciences Company for invaluable support, and to the associate editor Dr. Marcílio Matos, Dr. Kurt Marfurt, Dr. Hao Guo, Dr. Jayaram Vikram and the anonymous reviewer, whose constructive comments helped improve the quality of the paper. We also thank PETROBRAS for financial support and Bruno

Honório thanks the Brazilian Council for Technological and Scientific Development (CNPq, Brazil) for the support to this project by means of a PhD scholarship.

REFERENCES

Chakraborty, A., and D. Okaya, 1995, Frequency-time decomposition of seismic data using wavelet-based methods: Geophysics, **60**, 1906-1916.

Cheung, Y., and L. Xu, 2001, Independent component ordering in ICA time series analysis: Neurocomputing, **41**, 145-152.

Chopra, S., S. Misra, and K. J. Marfurt, 2011, Coherence and curvature attributes on preconditioned seismic data: The Leading Edge, **30**, 386-393.

Davogustto, O., M. C. de Matos, C. Cabarcas, T. Dao, and K. J. Marfurt, 2013, Resolving subtle stratigraphic features using spectral ridges and phase residues: Interpretation, 1, SA93–SA108.

Draper, B., K. Baek, M. Bartlett, and J. Beveridge, 2003, Recognizing faces with PCA and ICA: Computer Vision and Image Understanding, **91**, 115–137.

Farge, M., 1992: Wavelet transforms and their applications to turbulence. Annual Review of Fluid Mechanics. **24**, 395–457.

Guo, H., K. J. Marfurt, and J. Liu, 2009, Principal component spectral analysis: Geophysics, **74**, 35–43.

Henderson, J; S. J. Purves; and C. Leppard, 2007, Automated delineation of geological elements from 3D seismic data through analysis of multichannel, volumetric spectral decomposition data: Fisrt Break, **25**, 87-93.

Hoyer, P. O., and A. Hyvärinen, 2000, Independent Component Analysis Applied to Feature Extraction from Colour and Stereo Images: Network: Computation in Neural Systems, **11**, 191-210.

Huber, P. J., 1985, Projection pursuit: The Annals of Statistics, **13**, 435-525.

Hyvärinen, A., 1999a, Fast and Robust Fixed-Point Algorithms for Independent Component Analysis: IEEE Transactions on Neural Networks, **10**, 626-634.

_____, 1999b, Survey of independent component analysis: Neural Computing, **2**, 94-128.

Hyvärinen, A., and E. Oja, 1997, A fast fixed-point algorithm for independent component analysis: Neural Computation, **9**, 1483-1492.

Hyvärinen, A., and E. Oja, 2000, Independent Component Analysis: Algorithms and Applications: Neural Networks, **13**, 411-430.

Hyvärinen, A., J. Karhunen, and E. Oja, 2001, Independent Component Analysis: John Wiley & Sons. New York.

Hyvärinen, A., J. Särelä, and R. Vigário, 1999, Spikes and bumps: Artefacts generated by independent component analysis with insufficient sample size: Workshop on Independent Component Analysis and Signal Separation (ICA'99), 425–429.

Jibrin, B. W., T. J. Reston, and G. K. Westbrook, 2013, Application of volumetric seismic discontinuity attribute for fault detection: Case study using deep-water Niger Delta 3D seismic data: The Leading Edge, **32**, 424-428.

Liu, J., and K. J. Marfurt, 2007a, Instantaneous spectral attributes to detect channels: Geophysics, **72**, 23–31.

_____, 2007b, Multicolor display of spectral attributes: The Leading Edge, **26**, 268–271.

Liu, C., and H. Wechsler, 1999, Comparative assessment of independent component analysis (ICA) for face recognition: International Conference on Audio and Video Based Biometric Person Authentication.

Li, Y., X. Zheng, and Y. Zhang, 2011, High-frequency anomalies in carbonate reservoir characterization using spectral decomposition: Geophysics, **76**, 47-57.

Lu, W., 2006, Adaptive multiple subtraction using independent component analysis: Geophysics, **71**, S179–S184.

Lu, W., and L. Liu, 2009, Adaptive multiple subtraction based on constrained independent component analysis: Geophysics, **74**, V1-V7.

Matos, M. C., P. L. M. Osorio, E. C. Mundim, and M. A. S. Moraes, 2005, Characterization of thin beds through joint time-frequency analysis applied to a turbidite reservoir in Campos Basin, Brazil: 75th Annual International Meeting, SEG, Expanded Abstract, 1429-1432.

Matos, M. C., O. Davogustto, C. Cabarcas, and K. J. Marfurt, 2012, Improving reservoir geometry by integrating continuous wavelet transform seismic attributes: 82nd Annual International Meeting, SEG, Expanded Abstracts, 1-5.

McArdle, N. J. and M.A. Ackers, 2012, Understanding seismic thin-bed responses using frequency decomposition and RGB blending: Fisrt Break, **30**, 57-65.

Morlet, J., G. Arens, E. Fourgeau, D. Glard, 1982, Wave propagation and sampling theory - Part I: Complex signal and scattering in multilayered media: Geophysics, **47**, 203-221.

Partyka, G. A., J. Gridley, and J. Lopez, 1999, Interpretational applications of spectral decomposition in reservoir characterization: The Leading Edge, **18**, 353–360.

Sanchis, C., and A. Hanssen, 2011, Sparse code shrinkage for signal enhancement of seismic data: Geophysics, **76**, V151–V167

Sinha, S., P. S. Routh, P. D. Anno, and J. P. Castagna, 2005, Spectral decomposition of seismic data with continuous-wavelet transform: Geophysics, **70**, P19-P25.

Sørensen, J. C., U. Gregersen, M. Breiner, and O. Michelsen, 1997, High frequency sequence stratigraphy of upper Cenozoic deposits: Marine and Petroleum Geology, **14**, 99-123.

Stark, T., 2006, Visualization techniques for enhancing stratigraphic inferences from 3D seismic data volumes: First Break, **24**, 75–85.

Sun, S., J. P. Castagna, and R. W Siegfried, 2002, Examples of wavelet transform time-frequency analysis in direct hydrocarbon detection: 72nd Annual International Meeting, SEG, Expanded Abstracts, 457-460.

Torrence, C., and G. P. Compo, 1998, A practical guide to wavelet analysis: Bulletin of the American Meteorological Society, 79, 61–78.

Van der Baan, M., 2006, PP/PS Wavefield separation by independent component analysis: Geophysical Journal International, **166**, 339–348.

Vrabie, V. D., J. I. Mars, and J.-L. Lacoume, 2004, Modified singular value decomposition by means of independent component analysis: Signal Processing Magazine, **84**, 645–652.

Walden, A., 1985. Non-Gaussian reflectivity, entropy, and deconvolution: Geophysics, **50**, 2862–2888.

Wallet, B. C., 2013, Using the image grand tour to visualize fluvial deltaic architectural elements in south Texas, USA: Interpretation, **1**, SA117–SA129.

Wang, Y., 2007, Seismic time-frequency spectral decomposition by matching pursuit: Geophysics, **72**, 13–20.

CHAPTER 3: STRUCTURAL AND STRATIGRAPHIC FEATURE DELINEATION AND FACIESDISTRIBUTION USING SEISMIC ATTRIBUTES AND WELL LOG ANALYSIS APPLIED TO A BRAZILIAN CARBONATE FIELD

Juliana Finoto Bueno[1], Bruno César Zanardo Honório[1], Michelle Chaves Kuroda[1], Alexandre Campane Vidal[1], and Emilson Pereira[1]

[1]University of Campinas–UNICAMP, Department of Geology and Natural Resources, Institute of Geosciences, Campinas, São Paulo, Brazil.

E-mail: juliana.bueno@ige.unicamp.br; brunohonorio@gmail.com; mckuroda@gmail.com; vidal@ige.unicamp.br; emilson@ige.unicamp.br;

This paper was published by SEG journal Interpretation in 2014.

doi: 10.1190/INT-2013-0087.1

ABSTRACT

Identification of structural and stratigraphic components within a hydrocarbon reservoir is essential for the construction of geologic models that represent the facies distribution as accurately as possible. Such construction may represent a challenge for ancient carbonate reservoirs, which exhibit greater heterogeneity than siliciclastic reservoirs. We developed a workflow that incorporated seismic attribute analysis and well log data to highlight structural and architectural elements with the benefit of the understanding the distribution of facies in this features in an Albian offshore carbonate reservoir in Brazil. The proposed workflow combined incoherence, sweetness, and a new approach of spectral decomposition to delineate the main structural and architectural elements in the field. Well log facies and modern analog analyses were used to support the architectural elements′ interpretation. Joulters Cays is an oolitic shoal in the Bahamas that provided a modern analog for the field in study. Three main fault systems, responsible for the rollover structure of the field, were detected with the incoherence attribute. The workflow allowed the interpretation of four main architectural elements in the field: (1) tidal channels, (2) carbonate shoals, (3) reef, and (4) lagoons. Tidal channels and lagoons are mainly composed by wackestone. Carbonate shoals are primarily composed by grainstone with secondary packstone, while the reef crest is composed by packstone. Sequential indicator simulation (SIS) of well log facies supported these observations. The highlighted architectural elements could be helpful for the construction of a conceptual model of the field or useful as a training image for multiple-point statistics because SIS of well log facies does not define geologic bodies.

INTRODUCTION

The characterization of carbonate reservoirs is challenging because carbonate reservoirs can be more heterogeneous than siliciclastic reservoirs. Carbonate reservoirs can present lateral inconsistency in rock properties, subtle facies changes, and low impedance contrasts with the surrounding rocks. Seismic attributes together with well log data can help in the understanding of these heterogeneities, which is an essential step for the construction of reliable geologic models. Seismic attributes are used in quantitative and qualitative interpretation. Quantitative interpretation includes prediction of physical properties such as porosity or lithology, whereas qualitative interpretation is focused on detection of stratigraphic and/or structural features (Hart, 2008). In this paper, a qualitative approach was used to identify the main structural and architectural elements and the related facies of an Albian carbonate field in Brazil. To achieve these goals, spectral decomposition, sweetness, incoherence, and well log facies analysis were used. Spectral decomposition is an effective method for signal analysis, commonly used in seismic interpretation and reservoir characterization. By transforming the data into the frequency domain, it often becomes easier to identify many features that are difficult to delineate in the time domain (Chakraborty and Okaya, 1995). Sweetness is an attribute that was developed for identifying sands and sandstones using 3D seismic data in clastic successions (Hart, 2008). For this reason, it is largely used to detect channels (Hart, 2008; Ahmad and Rowell, 2012; Wang et al., 2012). Sweetness and spectral decomposition have mainly been applied to clastic depositional systems in which there are significant contrasts between the homogeneous matrix and the sandy volume. Because carbonates are often grown in place rather than transported to their depositional site and therefore suffer significantly greater diagenetic alteration, intracarbonate impedance changes are subtle and may not have an easily identified spatial pattern (Matos et al., 2009). For this reason, sweetness and spectral decomposition applied to carbonate reservoirs are still challenging, and the relation between carbonate rock properties and seismic sweetness and spectral content is not very well documented. To help in the understanding of the architectural elements identified by means of the sweetness and spectral decomposition, well log facies analysis was performed for an Albian Brazilian carbonate field.

This Albian Brazilian field is an offshore field named the "A Field" for confidentiality reasons. For the same reason, no depth, time, and coordinates can be presented. The A Field is composed of oncolitic, oolitic, and peloidal calcarenites, calcirudites, and calcilutites, deposited in a shallow platform environment. The Albian reservoir is responsible for 31% of A-Field in-place oil volume, but the recovery factor is only 15.40% (Horschutz et al., 1992). This low recovery factor can be related to the difficulties for the definition of stratigraphic architecture and interrelationships of facies that control the distribution of reservoir and nonreservoir facies.

This study focuses on delineating the principal structural and architectural elements of the A Field and on understanding the relations between these features and depositional facies.

FIELD DESCRIPTION

Geologic background

The A Field is located in the Brazilian continental platform, in the south part of the Campos Basin (Figure 3. 1). The area of the Campos Basin is approximately 100,000 km2. More than 1600 wells have been drilled for oil and gas exploration for more than three decades. Campos is an important offshore basin, encompassing more than 90% of the Brazilian reserves for oil and gas (Winter et al., 2007). The Campos Basin is a passive continental margin-type basin formed during the breakup of the Gondwana supercontinent resulting in the separation of South America and Africa (Guardado et al., 1989). The basin is composed of several hydrocarbon-producing fields of Oligo-Miocene ages. Sediment starvation occurred in the basin from the Cenomanian to the Maestrichtian as a consequence of tectonic subsidence, eustatic sea level rise, and a relatively low influx of terrigenous sediments (Guardado et al., 1989). Stratigraphically, the Campos Basin has been subdivided into three megasequences (Ponte and Asmus, 1976; Horschutz et al., 1992; Rangel et al., 1994). These depositional sequences evolve from alluvial-lacustrine dominant syn-rift sediments in the Neocomian to transitional alluvial fan and evaporitic sediments in the Aptian, to postrift marine dominant sedimentation in the Albian to the Recent. The stratigraphic sequence includes Campos, Macaé, and Lagoa Feia Formations (Guardado et al., 1989, 2000). The installation of the marine environment started with carbonate deposition in shallow-water conditions,

followed by the siliciclastics of the Macaé Formation, which is a wedge-shaped structure divided into the Lower and Upper Macaé.

The Campos Basin shows two principal structural elements: (1) the high angle normal faults of the rift phase and (2) the adiastrophic structures, mostly normal listric faults that affected the postsalt sediments. The rift phase is represented by horsts and grabens involving basement and presalt sediments. The adiastrophic structures were formed due to basin tilting and differential compaction. Salt movement resulted in the formation of pillows that controlled the distribution of Albian shallow water carbonate facies and the thickness of the lowermost section of the Lower Macaé. With the continuing evolution of the salt structure, syndepositional listric faults were generated, developing structures of rollover type, which caused abrupt lateral facies changes at the top of the Lower Macaé (Spadini et al., 1988; Guardado et al., 1989).

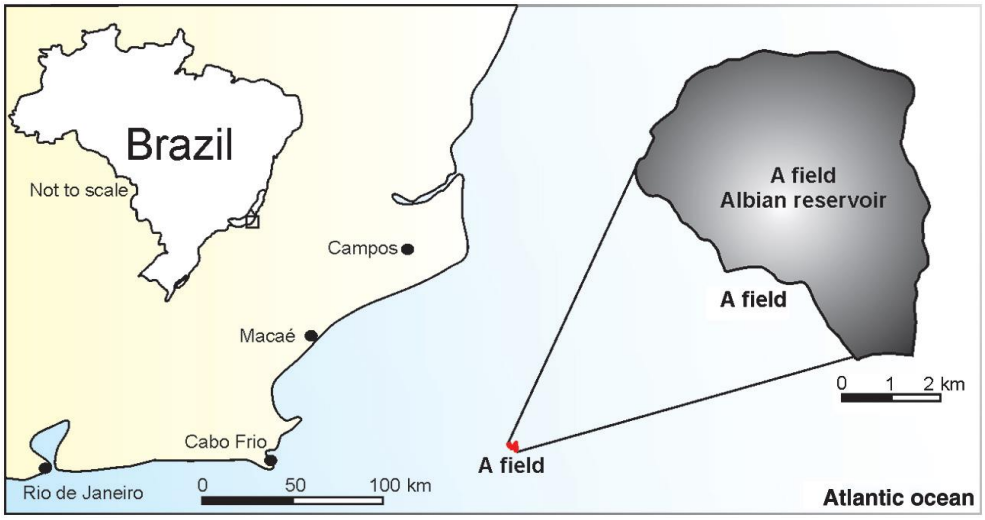

Figure 3. 1: Location map of the study area.

The Campos Basin encompasses dozens of oilproducing fields, and A is one of these fields in this basin. The Albian reservoir of the A Field covers an area of 32 km^2 in water depths of around 100 m and is responsible for 31% of A-Field in-place oil volume, but the recovery factor is only 15.40% (Horschutz et al., 1992). The A Field is composed of oncolitic, oolitic, and peloidal calcarenites, calcirudites, and calcilutites of the Quissamã Member in the Macaé Formation, deposited in a shallow platform environment. The structure consists of a smoothly dipping dome formed by rollover associated with salt tectonics, cut by small throw growth faults. The trapping of oil in this reservoir is essentially structural- stratigraphic in nature. The structural component is represented by normal growth faults and the stratigraphic components by facies variations in the upper part of the reservoir where the calcarenites and calcirudites grade

into calcilutites to the west and south-southwest of the field. The average porosity and permeability are 20% and 250 mD, respectively. The gravity of the oil is 20º API (Horschutz et al., 1992).

Spadini (1992) proposes that the Joulters Cays (JC), in the Bahamas, could be a modern analog for the sedimentation in Albian of the A Field, considering the peloidal and oolitic facies relationship and the sedimentary structures presented in both areas. Despite Spadini's efforts to characterize the A-Field reservoir, the geometries of the carbonatic bodies still remain undefined.

Database

The A Field is covered by a 3D seismic survey, from which structural and sedimentological information was derived for reservoir evaluation. A total of 26 wells drilled and logged were used in this study. The well logs presented in the data set are density (RHOB), gamma ray (GR), resistivity (ILD), neutron porosity (NPHI), and sonic (DT). Sixteen wells have a drill cuttings description, two wells were cored, and qualitative petrographic description is available.

METHODS AND PRINCIPLES

The zone of interest is the Albian reservoir of the A Feld (Figure 3. 1). Three main seismic horizons (A1, A2, and A3) were previously interpreted in the 3D seismic data and interpolated to generate continuous horizon surfaces for extracting attributes (Figure 3. 2). The A1 horizon represents the top of the Albian reservoir. A seismic geomorphology workflow (Posamantier et al., 2007) was used to highlight structural and architectural elements by means of attribute analysis and well log facies analysis (Figure 3. 3). A modern analog, represented by JC, was used to help the understanding of the architectural elements delineated in this study.

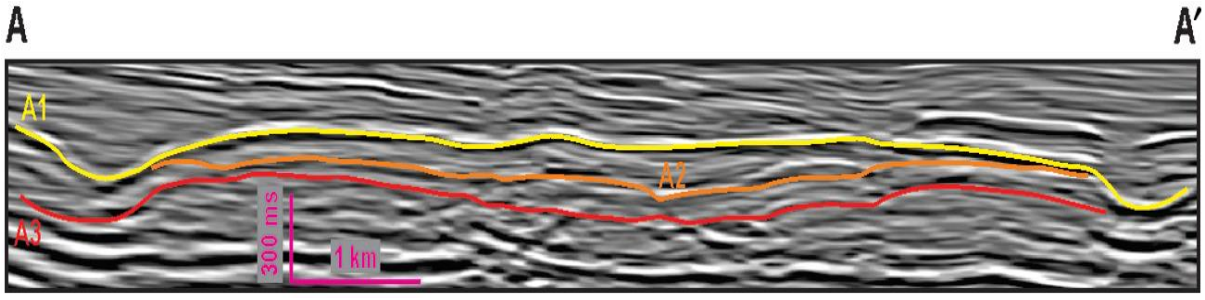

Figure 3. 2: The Albian carbonate reservoir showing three marked horizons.

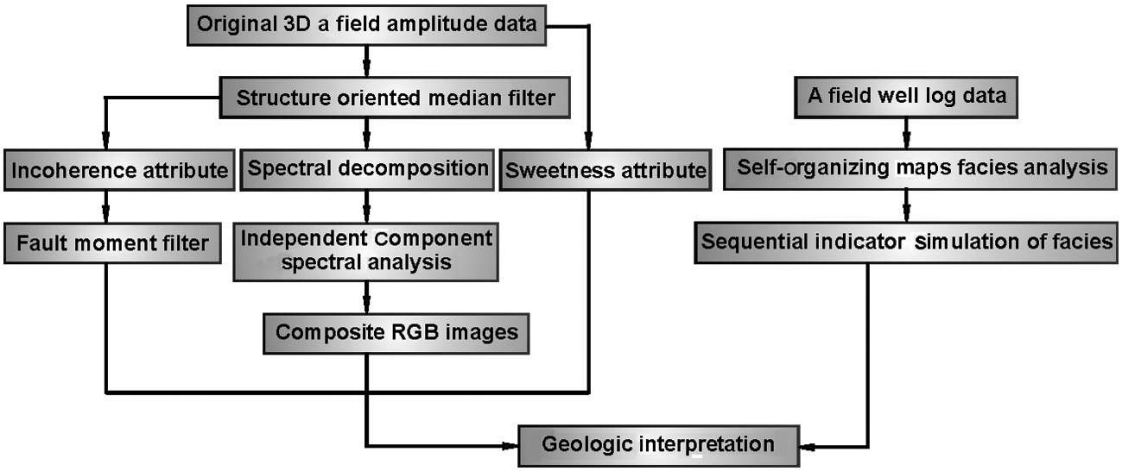

Figure 3. 3: Seismic geomorphology workflow used to highlight structural and architectural elements interpretation of the A Field.

Seismic attributes and spectral decomposition

The sweetness attribute is derived by dividing the reflection strength (or instantaneous amplitude envelope) by the square root of the instantaneous frequency (Radovich and Oliveros, 1998; Hart, 2008), and it is a useful attribute for detecting channels or other stratigraphic features when those features can be distinguished from a "background" lithology by a combination of instantaneous frequency and reflection strength (Hart, 2008). Usually, sweetness is used to map sand bodies because acoustic impedance contrasts between sands and shales tend to be high in clastic environments (Hart, 2008; Ahmad and Rowell, 2012). In the same way, sweetness also shows variability in carbonate successions. In carbonate reservoirs, sweetness can be useful qualitatively to differentiate contrasts between zones with more mud content (e.g., wackestone facies) from zones without mud (e.g., grainstone facies). The sweetness attribute was compared to well log facies distributions to check the validity of any relationship between this attribute and mud content in the A-Field carbonate reservoir.

The structure-oriented median filter (median SOF) was used to enhance seismic continuity for faults and channel delineation. This filter enhances seismic continuity by selecting the median values of multiple time samples along estimated local dip from adjacent traces in the inline and crossline directions. The filter picks up samples within the chosen aperture along the local dip and azimuth replacing the amplitude of the central sample position with the median value of the amplitudes (Chopra and Marfurt, 2008).

Incoherence and the fault moment filter are attributes that highlight geologic structures like faults and channels. Seismic trace values within a window of scale

length, in samples, will be compared with surrounding seismic traces. An estimate of local dip is made at every spatial and temporal location, and incoherence is estimated along these dips (Marfurt et al., 1999). The fault moment filter creates an attribute volume that accentuates the seismic trace-to-trace discontinuities estimated with incoherence. By using image processing techniques, the fault moment filter detects and enhances regions of high incoherence exhibiting high spatial and vertical correlation. The fault moment filter is actually a cascade of two filters. The first filter is $cp*(1-nz^2)$, where cp is the local measure of planarity and nz is the vertical component of the local unit-length normal vector. The second filter is 1-rsq, where rsq is the second moment of the function with respect to the plane defined by the local orientation.

To delineate geometric features of the A Field, a spectral decomposition technique was applied to the median SOF 3D data. Spectral decomposition is a powerful tool to identify and map temporal bed thickness and geologic discontinuities over large 3D seismic surveys (Partyka et al., 1999). For broadband seismic data, an interpreter might generate and analyze dozens of somewhat redundant amplitude and phase spectral components. B. C. Z. Honório (personal communication, 2013) propose a new algorithm called independent component spectral analysis (ICSA) to reduce the multiplicity of spectral data and enhance the most energetic trends inside the data. Like principal component analysis (Guo et al., 2009), ICSA converts the 10–80 Hz frequency components into a much smaller suite of narrowband spectra that can be conveniently visualized using the three primary colors of red, green, and blue (RGB) in a single image.

Well log facies interpretation

The facies were defined by means of the self-organizing maps (SOM) algorithm. Developed by Kohonen (2001), SOM is an unsupervised neural network method, with no a priori information required to train the algorithm. The technique is based on neuron (also called prototype vector) mapping, in which nodes are updated according to input similarity. Not only the nearest neuron but also its neighborhood is updated to be statistically closer to the desired input, thereby preserving the topological structure of mapping.

Ten lithofacies were identified from the core samples, ranging from grainstone to wackestone. These lithofacies were grouped into four major lithotypes according to their depositional texture and petrophysical properties: coarse- to medium-grained

grainstone, medium-grained packstone, fine-grained wackestone, and cemented facies. For the SOM classification, 151 prototypes vectors were used and clustered into four groups using a k-means algorithm. For each cluster, the core samples were identified and the histogram for the facies distribution of these samples was performed. The facies with the highest frequency in the histogram was selected to label the cluster. More details about the facies classification can be found in Kuroda et al. (2012).

The A1, A2, and A3 time seismic horizons (Figure 3. 2) were converted into depth units and used to build the structural model for the A Field. The A1 and A3 horizons represent the top and the base of the Albian reservoir, respectively. To capture the reservoir heterogeneities, a geostatistical grid cell resolution of 50 × 50 × 1 m was defined inside the physical limits of the A Field Albian reservoir. The geostatistical grid is a corner- point-based, layered geocellular grid, which means that each cell of the grid honors the structural model and the seismic horizons. The facies log defined in the wells using the SOM algorithm was upscaled and discretized to the geostatistical grid resolution without any loss of heterogeneity. The facies model was built by using a sequential indicator simulation (SIS) algorithm and the vertical trends obtained with vertical proportion curves. The vertical proportion curve gives the proportion of each facies per level in the flattened space, integrated laterally over the whole field. It reflects the vertical variations of the facies proportions and confirms the depositional process that governed the facies distribution (Ravenne et al., 2002).

SIS is an algorithm used to generate a discrete 3D facies parameter for the current geostatistical realization. A facies code is assigned to each cell inside the geostatistical grid, defining the facies (grainstone, packstone, wackestone, or cemented facies) in that cell, based on probabilities calculated from well data and user-defined input (Srivastava, 1994; Seifert and Jensen, 1999). Although SIS does not define geologic bodies, it can help to support the geologic interpretation made by the use of the sweetness attribute and spectral decomposition.

RESULTS AND DISCUSSION

Fault delineation

The fault moment filter (Figure 3. 3), computed from the incoherence volume, highlights three main discontinuity fault systems (Figure 3. 4). The more pronounced fault system in the A Field is the boundary F1 faults that are clearly seen on the fault moment filter horizon slice (Figure 3. 4) and mark the reservoir limit. The F1 are normal faults that exhibit a listric style creating a rollover anticline formed during the halokinesis syndepositional in the A Field (Figure 3. 5). The main F1 fault direction is northwest–southeast, which is the regional main fault direction (Albertão et al., 2011) that forms the overall structure and palaeotopography of the Albian reservoir.

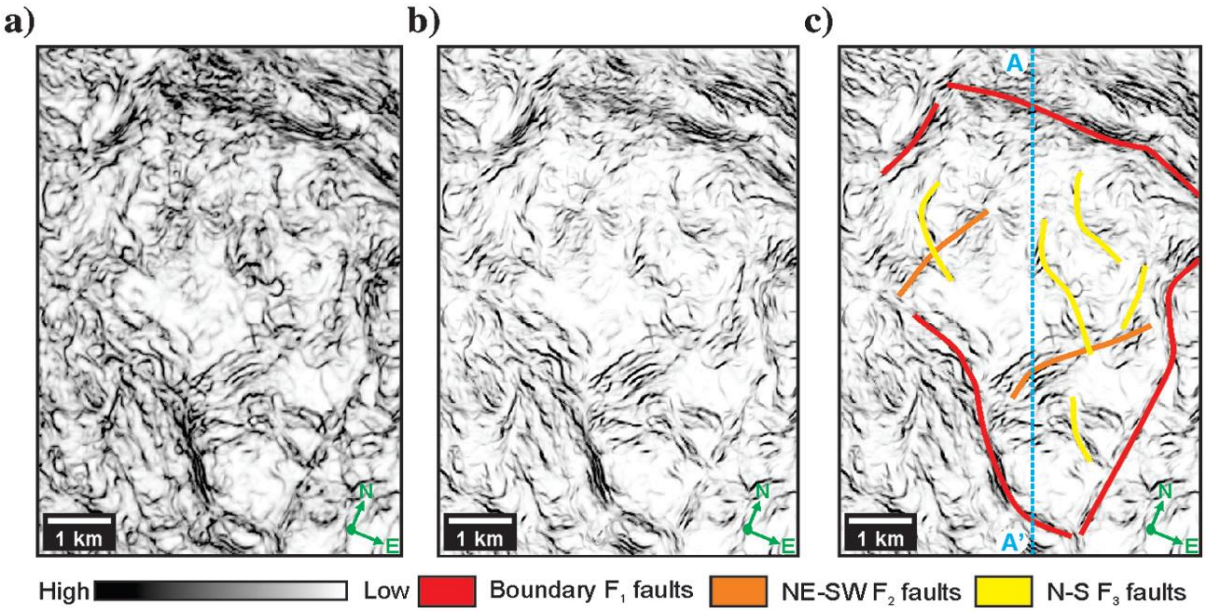

Figure 3. 4: Horizon slices along the A1 horizon shown in Figure 2 through the (a) incoherence and (b) fault moment filter volumes. (c) Same horizon slice through the fault moment filter with interpreted faults showing location of line AA' displayed in Figures 2, 5, and 8.

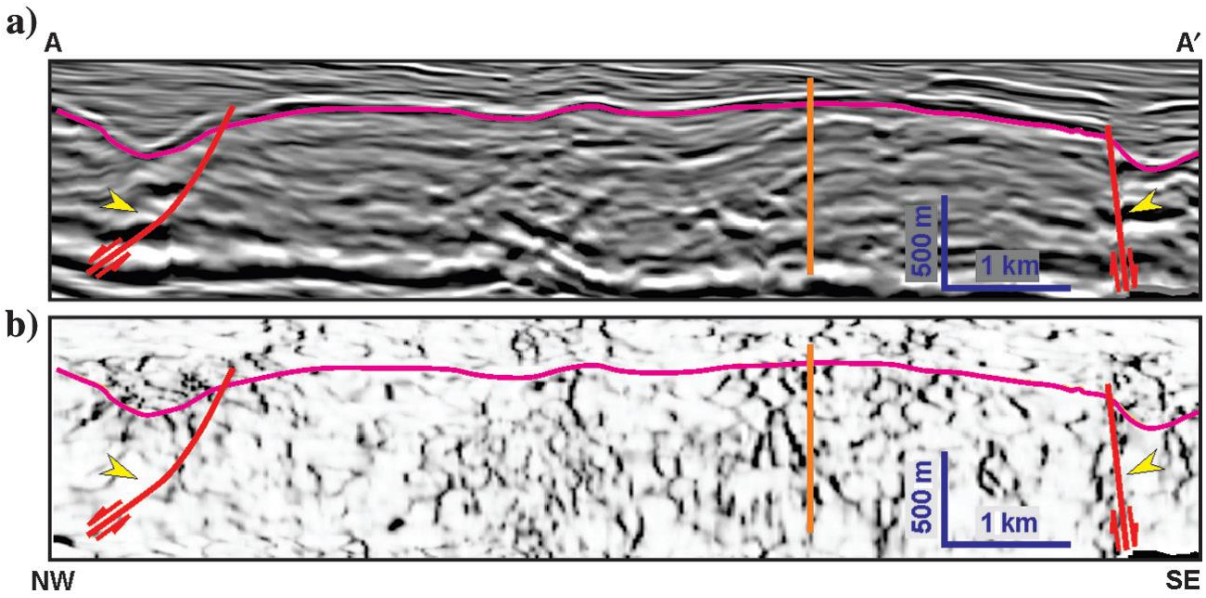

Figure 3. 5: AA′ seismic line showing the A1 horizon and faults (F1 in red and F2 in orange) in (a) amplitude data and (b) fault moment filter. Note the rollover structure marked by F1 faults (yellow arrows).

The F2 and F3 are northeast–southwest and north– south normal faults, respectively (Figure 3. 4). They represent a secondary set of less significant faults.

Architectural elements

The identification of architectural elements in the A Field is not possible to map on conventional full spectrum seismic data (Figure 3. 6a). To delineate these features, ICSA was applied to the spectral decomposition data. Discrete frequency cubes were computed with the continuous wavelet transform technique of spectral decomposition for the frequency bandwidth of 10–80 Hz. ICSA identifies seven main components of the spectral decomposition energy, and these components were extracted along the seismic horizons (Figure 3. 6b). After qualitative analysis, the independent components IC-2, IC-6, and IC-7 were chosen for the composite RGB image (Figure 3. 6c).

We used sweetness (Figure 3. 7a), spectral decomposition (Figure 3. 7b), and simulation of facies analysis (Figure 3. 7c) to help delineate the architectural elements. We interpret these geomorphological features to indicate the (1) tidal channel, (2) carbonate shoals, (3) reef, and (4) protected lagoons (Figure 3. 7). More details about these features are shown in the following subsections.

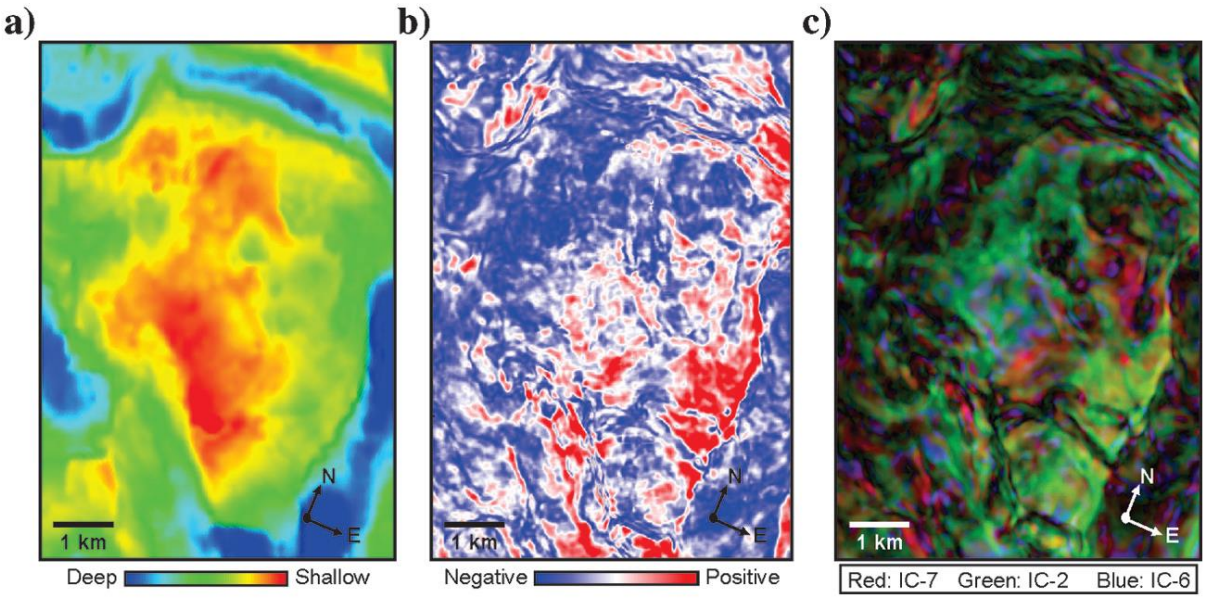

Figure 3. 6: (a) Depth-structure map of the A1 horizon and corresponding horizon slices through (b) seismic amplitude and (c) ICSA components 2, 6, and 7 co-rendered using a composite RGB display.

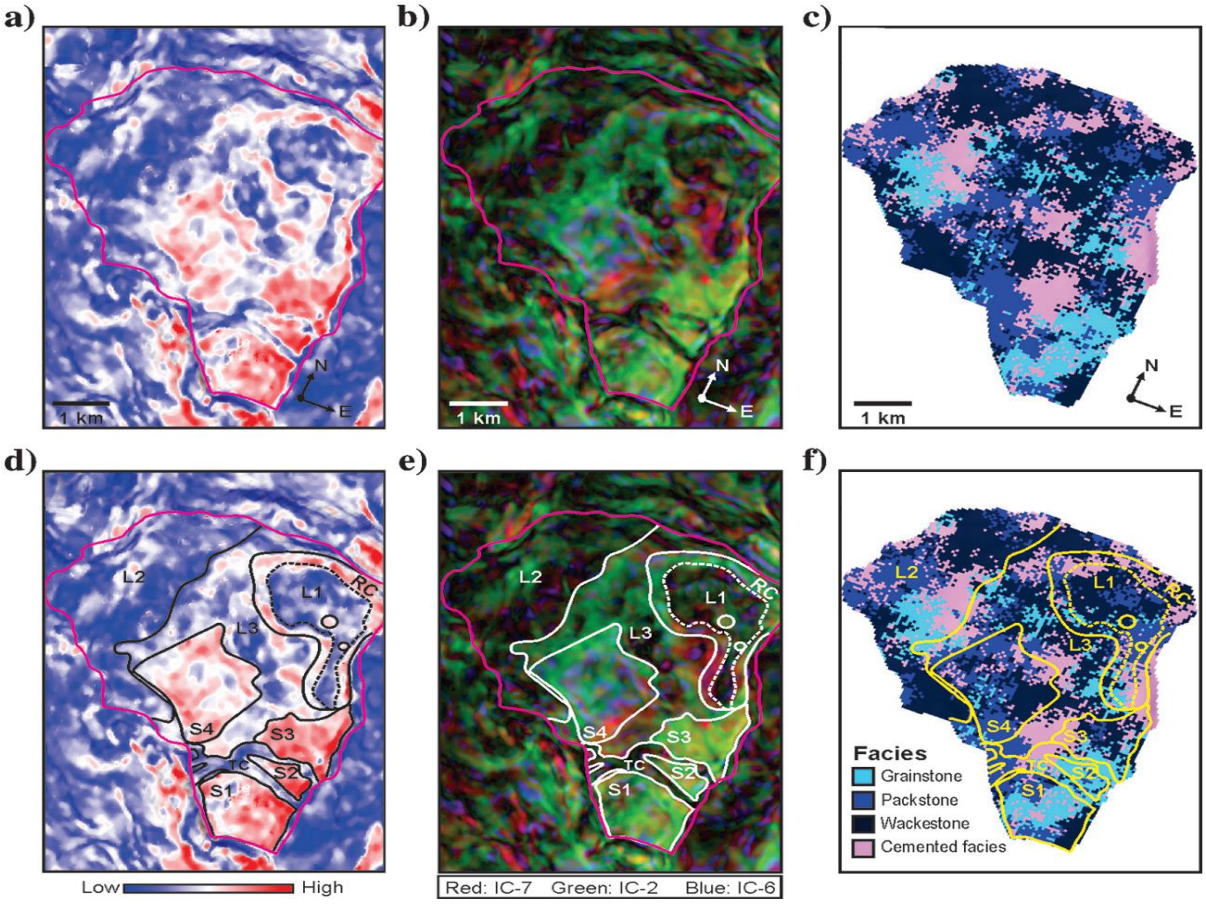

Figure 3. 7: Horizon slices along horizon A1 through (a) sweetness, (b) co-rendered ICSA components 2, 6, and 7, and (c) a realization of facies simulation. (d-f) Same images with interpretation showing shoals (indicated by S), a reef crest (indicated by "RC"), a lagoon (indicated by "L"), and a tidal channel (indicated by "TC"). The pink polygon represents the physical limit of the A Field Albian reservoir. A more detailed description is in the text.

Tidal channel and delta identification

The composite RGB image of the A1 horizon slice (Figure 3. 8a) reveals two interpreted channels in the southern area of the A Field. The fault moment filter horizon slice of the A1 horizon (Figure 3. 8b) also shows the channels but not as clearly as the composite RGB image. Other possible geologic processes, such as faults, can also produce discontinuity detectable by incoherence and fault moment filter attributes. However, we interpret the discontinuity under discussion as channels because (1) the observed discontinuities are not straight, which is expected by faults, (2) the vertical slice through seismic amplitude (Figure 3. 8c) shows a channel feature, and (3) the composite RGB image shows that the sedimentary filling has a different spectral component compared with the neighboring areas, which is not expected if the discontinuity represents a fault system.

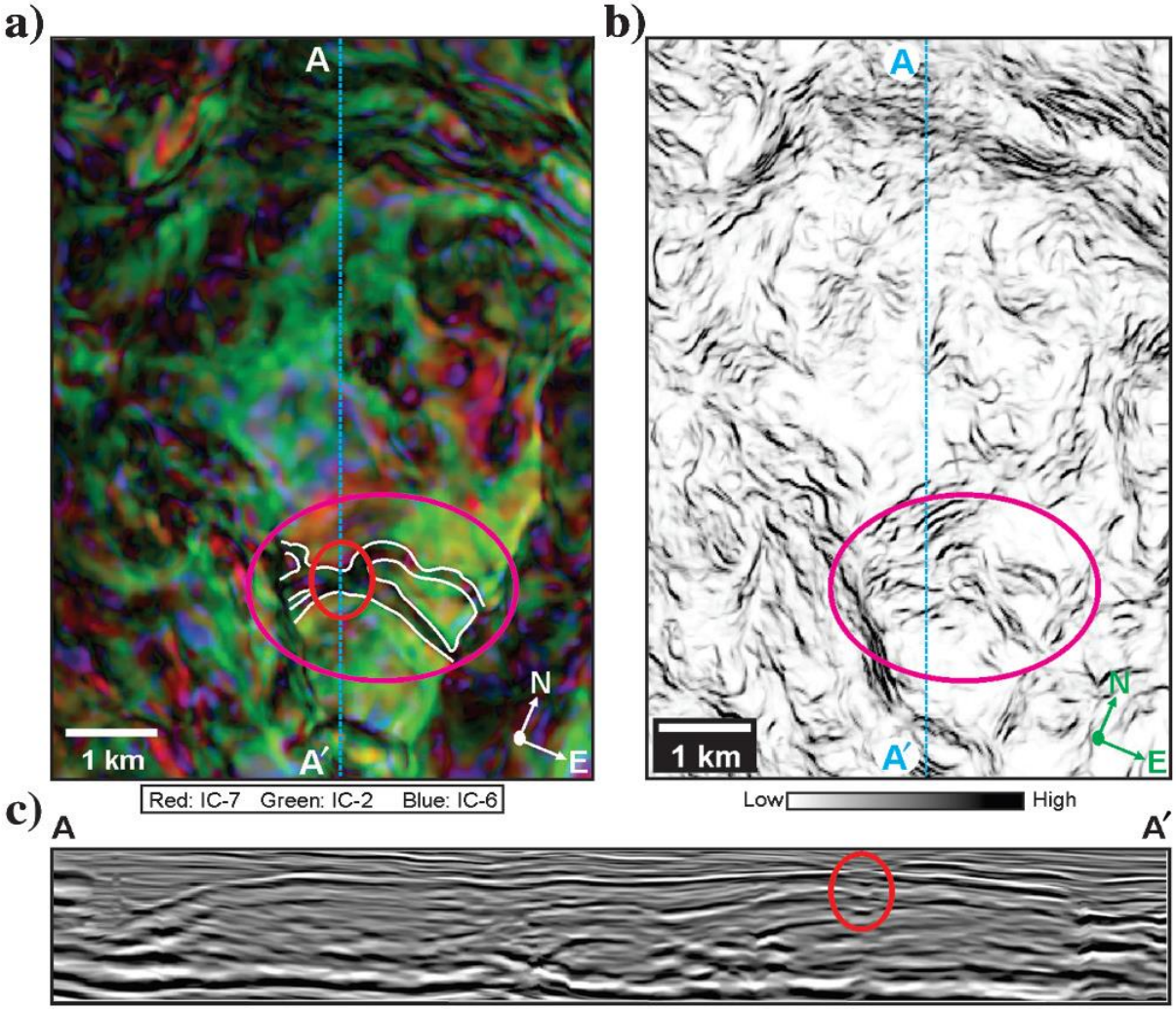

Figure 3. 8: Interpreted channel features extracted from (a) the composite RGB image of the A1 horizon slice, (b) the fault moment filter horizon slice of the A1 horizon, with the dashed blue line showing the location of the AA′ seismic line, and (c) AA′ seismic line. Red and pink ellipses show the interest features.

Partyka et al. (1999) propose that amplitude spectra delineate thin-bed variability via spectral notching pattern, which is related to local rock mass variability. This concept can be applicable to the interpreted tidal channels. The interior of interpreted tidal channels revealed a spectral content different that presented by the surrounding areas (Figure 3. 8a), and this difference could have been related to differences in the sedimentary infill from the interior of the channels compared to the surrounding areas.

Spadini (1992) proposes that the JC could be a modern analog for the sedimentation in Albian of the A Field, considering the peloidal and oolitic facies relationship and the sedimentary structures presented in both areas. However, Spadini (1992) does not consider geometrical relationships between the two fields. Our study indicates that the

proposed channel for the A Field (Figure 3. 9a) is similar to those present in the JC (Figure 3. 9b).

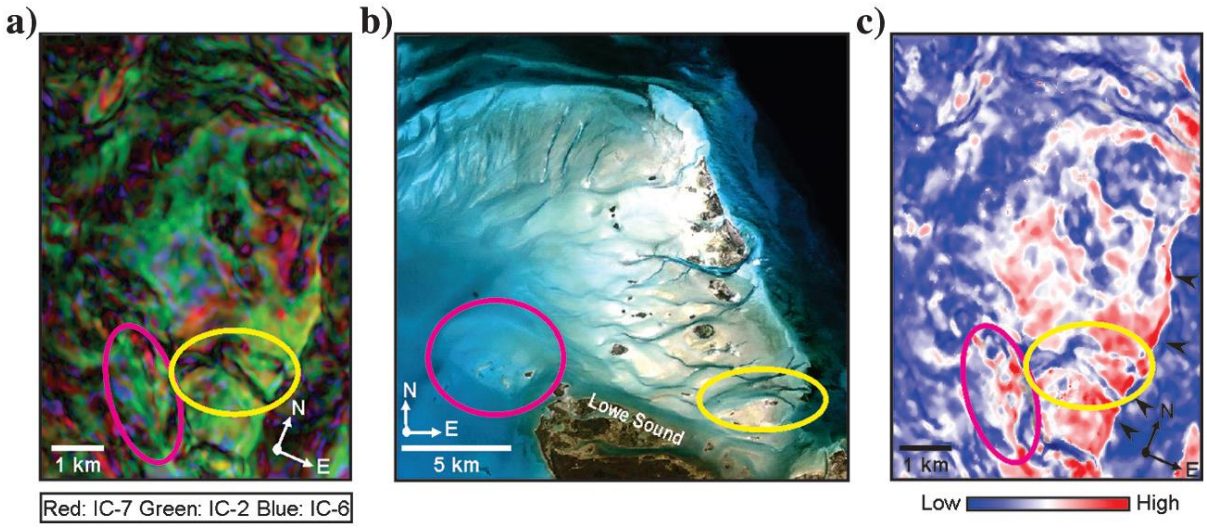

Figure 3. 9: (a) Composite RGB image of A1 horizon slice, (b) JC satellite image (NASA-Johnson Space Center, 2013); (c) sweetness attribute extracted from A1 horizon slice. Yellow ellipses show channels and pink ellipses show flood tidal delta lobes in the A Field and JC. Black arrows show the areas with high sweetness.

The JC is a Holocene island, immediately north of Andros Island on Great Bahama Bank, and it is interpreted as a modern shoal complex that extends over 400 km2 and varies on average 4 m in thickness. The JC is a shoal formed by a sand flat, partly cut by numerous tidal channels and fringed on the ocean-facing borders by mobile sands (Harris, 1979, 1983). The tidal channels occur in the east–west and northeast–southwest directions and are not completely opened in the seaward and bankward sides.

In the A Field, the proposed channel occurs in east–west direction (Figure 3. 9a) and differently from the JC, the channel is open in the seaward and bankward sides. Another difference of the A Field compared to JC is the amount of tidal channels. In the A Field, spectral decomposition allowed the interpretation of two channels, while in the JC, there are several tidal channels. This difference in amount of tidal channels could be explained by the variance in area; while the JC is a 400-km2 area, the A Field is only a 32-km2 (Figure 3. 9).

The A Field tidal channels length range from 1.5 to 2.0 km, which is close to the 3 km average for the Bahamas tidal channels (Harris, 2010), and they have their seaward ends terminate abruptly in a paleo seaward-facing, similar to those present in the JC (Figure 3. 9). In the bankward side, the A Field tidal channels join to form one wide channel that divides into three branches forming a flood tidal delta lobes in a more

gradual open ending (Figure 3. 8a). In the JC area, the bankward channels shoal and divide into several interconnected depressions within the sand flat (Harris, 1979).

The bankward end of the A Field tidal channels forms a flood tidal delta lobe (Figure 3. 9a), although this presents an elongated geometry. The geometry of the flood tidal delta lobes tends to be more circular, similar to that observed in the bankward end of the Lowe Sound in JC (Figure 3. 9b). Lowe Sound is a wide channel that separates JC from the Andros Island in the south. The anomalous elongated geometry of the flood tidal delta lobe in the A Field can be explained by the F1 faults (Figure 3. 4) that affected the region as a consequence of syndepositional halokinesis, forming a slope in the bankward end of the tidal channels.

The sweetness attribute shows that the filling of the flood tidal delta lobe is similar to that presented in the seaward part of the A Field (Figure 3. 9c). In general, sweetness is useful for mapping sand bodies because acoustic impedance contrasts between sands and shales are high in clastic environments (Ahmad and Rowell, 2012). In the same way, in carbonate reservoirs, sweetness can be useful qualitatively to show contrasts between zones with more mud content such as wackestone facies and zones without mud content such as grainstone facies.

If in a siliciclastic depositional environment high sweetness is correlated to sand content (Ahmad and Rowell, 2012), in the A Field, carbonatic reservoir high sweetness can be associated to grainstone facies and low sweetness can be associated to wackestone facies. Tidal channels are clearly marked by low sweetness (Figure 3. 9c) representing a facies with more mud content, such as wackestone facies, which is the opposite of that observed for the flood tidal delta lobe. The flood tidal delta lobe presents a high sweetness associated with grainstone facies that could be transported to this area by the tidal channels. The tidal channels transported the ooid/oncoid sediments, to form grainstone, from the seaward part of the A Field to the flood tidal delta lobe, which could explain the high sweetness presented only in these areas of the field. In the Bahamas, Reeder and Rankey (2008) show that the tidal channels are able to transport oolitic sediments.

Carbonate shoal identification

The composite RGB image, sweetness attribute, and facies distribution for the A1 horizon slice reveal four areas with potential for shoal development (Figure 3. 7). In the shoal areas, “S” sweetness is high (Figure 3. 7a and Figure 3. 7d) compared to the tidal

channel area. As described above, high sweetness in carbonate reservoirs can be associated to areas with low mud content such as those formed by grainstone. The same high sweetness areas are marked in the composite RGB image of A1 horizon slice (Figure 3. 7b and Figure 3. 7e), and these areas have a different spectral signature compared to that shown by the tidal channels. In area S4, the sweetness is lower than in areas S1, S2, and S3. The A1 horizon slice in this area shows a mixture of RGB components.

The facies distribution in the A Field (Figure 3. 7c and Figure 3. 7f) confirms that in areas S1, S2, and S3 (Figure 3. 7a and Figure 3. 7d), high sweetness values and IC spectral component 2 (Figure 3. 7b and Figure 3. 7e) are associated with grainstone facies, while medium sweetness content and a mixture of spectral component are associated with packstone facies in area S4.

Grainstone facies are characteristics of environments of high hydraulic energy (Wright, 2008), while in the packstone area the energy is moderate. The variation of depositional environments and facies distribution in carbonate reservoirs can be explained by water depth variation in the area or by changing the level of agitation of the grains caused by ocean currents.

Ocean currents currents are produced by tides and waves and are concentrated at major topographic features, such as along ramp and rimmed shelf margins, islands, and shorelines (Lucia, 2007). In the JC area, Harris (1979) proposes that the variations in depositional environment are a result of changing the level of agitation of the grains. If the same idea is used to explain the facies variation in the A Field, the areas S1, S2, and S3 represent a paleo high in the field where high energy, with constant wave action, grainstone facies were deposited. By analogy, area S4 represents a lower area of ancient relief where moderate energy packstone facies were deposited.

At present, these observations are reversed as shown by Figure 3. 6b. The high area in the A Field is the area S4, while areas S1, S2, and S3 represent low structural areas. These features can be explained by the F2 and F3 faults that affected the area and can be responsible, together with the F1 faults, for the current anatomy of the A Field.

Reef identification

The composite RGB image, sweetness attribute, and facies distribution for the A1 horizon slice reveal an area with potential reef development (Figure 3. 7). Matos et al. (2009), using wavelet transform Teager-Kaiser energy, propose that the same area can be associated to bioconstructions. The available drill cuttings descriptions for wells in this area reveal a large amount of carbonate bioconstructed fragments.

In the circular area presented in Figure 3. 7, according to the same reasoning presented above, medium sweetness content (Figure 3. 7a and Figure 3. 7d) and a mixture of spectral component (Figure 3. 7b and Figure 3. 7e) are associated with packstone facies that can be associated to the developing of reef crest (RC) in an area of moderate relief (Figure 3. 6b). According to Tucker and Wright (2008), reefs will preferentially develop on topographic highs because shallow-water corals grow faster than deeper forms and sedimentation will be reduced on higher areas. Facies simulation (Figure 3. 7c and Figure 3. 7f) shows that in the RC area, the cemented facies are predominant. Cementation is a major process and is partly responsible for the steep, wave-resistant profiles of many reefs and occurs abundantly in ancient reefs (Tucker and Wright, 2008).

The dashed circular area presented in Figure 3. 7 shows the same characteristics presented by the tidal channels with low sweetness content (Figure 3. 7a and Figure 3. 7d) that can be associated to wackestone facies with a high amount of mud. The spectral signature (Figure 3. 7b and Figure 3. 7e) is quite similar to that presented by the tidal channels. The dashed circular area presented in Figure 3. 7 represents a relief lower (Figure 3. 6b) than the RC area and is interpreted as a lagoon area (L1) in the inner part of the reef. Facies simulation (Figure 3. 7c and 7f) confirms that the L1 area has much more wackestone facies than the RC area.

In the inner area of the lagoon, there are some circular bodies (Figure 3. 7) with the same sweetness and spectral behavior as that presented by the RC area, with high sweetness content and a mixture of spectral component that was interpreted as characteristics of packstone facies. The circular bodies can represent small reefs rising up from the lagoon floor analogous to modern Bermuda Patch Reefs (Garret et al., 1971), although we do not have enough control to classify the reef in the A Field as a patch reef.

Protected areas

The L2 and L3 areas (Figure 3. 7) are potential areas to the formation of a lagoon in the A Field. In these areas, the sweetness attribute is low (Figure 3. 7a and Figure 3. 7d) and the spectral signature (Figure 3. 7b and Figure 3. 7e) is similar to that presented in the L1 area. These features can be associated to a lagoon environment protected from the ocean swell and storms by the shoal barrier system. Packstone to lime mudstone are the typical sediments in protected carbonate lagoons. However, there can be significant variation in sediment type depending on the circulation within the lagoon, which in turn is largely controlled by the frequency of tidal channels and by the climate (Tucker and Wright, 2008). The low sweetness and the spectral signature shown by the L2 and L3 areas can be associated with wackestone facies with high amounts of mud, similar to that observed by the lagoon in the inner part of the reef. Facies simulation (Figure 3. 7c and Figure 3. 7f) indicates that the predominant facies are packstone and mudstone in regions L2 and L3. Cemented facies and a small percentage of grainstone are secondary facies.

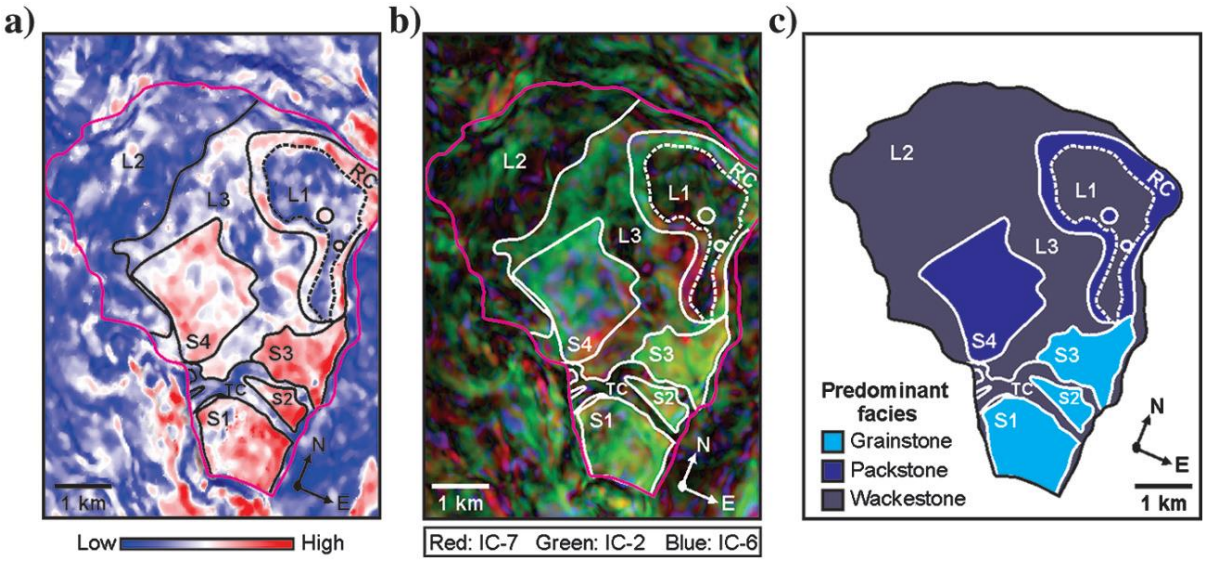

Figure 3. 10: The A Field showing principal structures in the A1 horizon slice from the (a) sweetness attribute and (b) composite RGB image. (c) Predominant facies distribution according to the main structures in the field. Areas: S, shoals; RC, reef crest; L, protected lagoons, and TC, tidal channel. The pink polygon represents the physical limit of the A Field Albian reservoir.

CONCLUSIONS

The seismic geomorphology workflow used in this study successfully integrated seismic interpretation, attribute analysis, geostatistical simulation of well log facies, and modern analog analysis to build a geologic scenario for the A1 top horizon of the A Field Albian reservoir.

The fault moment filter applied to incoherence volume identifies three main discontinuities fault system, F1, F2, and F3. The F1 faults are responsible for the rollover structural anatomy of the reservoir.

Previous facies simulation in the A Field showed that the sweetness attribute can be used to qualitatively distinguish different architectural elements and lithological patterns in a carbonate reservoir in association with composite RGB images, in this case. The sweetness volume may help to assist facies prediction as a trend function during the geostatistical simulation.

JC in the Bahamas may represent a modern analog for the Albian A Field. Using this analog, the composite RGB image of independent spectral components delineates the reservoir into four main architectural elements (Figure 3. 10): (1) tidal channel, (2) carbonate shoals, (3) reef, and (4) lagoons.

The sweetness attribute (Figure 3. 10a) together with composite RGB images (Figure 3. 10b) provide a means to estimate the predominant facies for each architectural element (Figure 3. 10c). The tidal channel and lagoons are sites of wackestone deposition, mainly. Carbonate shoals are primarily composed by grainstone with some packstone subordinately, while the reef crest is composed by packstone. SIS of facies supported these observations, and the highlighted architectural elements can be helpful for the construction of a conceptual model of the field or useful as a training image for multiple-point statistics, because SIS does not define geologic bodies.

ACKNOWLEDGMENTS

The authors wish to thank Petrobras for their financial support, cooperation in providing the data, and the authorization to publish this work. Transform and Roxar are acknowledged for providing the seismic interpretation and reservoir modeling software, respectively. M. Cornetti and K. J. Marfurt are greatly appreciated for their useful suggestions. We also thank G. Castilho for providing the time horizons used in this work. We benefited from the positive comments of two referees.

REFERENCES

Ahmad, M. N., and P. Rowell, 2012, Application of spectral decomposition and seismic attributes to understand the structure and distribution of sand reservoirs within Tertiary rift basins of the Gulf of Thailand: The Leading Edge, 31, 630–634.

Albertão, G. A., T. Mulder, and R. Eschard, 2011, Impact of salt-related palaeotopography on the distribution of turbidite reservoirs: Evidence from well-seismic analyses and structural restorations in the Brazilian offshore: Marine and Petroleum Geology, 28, 1023–1046,

Chakraborty, A., and D. Okaya, 1995, Frequency-time decomposition of seismic data using wavelet-based methods: Geophysics, 60, 1906–1916.

Chopra, S., and K. Marfurt, 2008, Gleaning meaningful information from seismic attributes: First Break, 26, 43–53.

Garret, P., D. L. Smith, A. O. Wilson, and D. Patriquin, 1971, Physiography, ecology, and sediments of two Bermuda Patch Reefs: Journal of Geology, 79, 647–668.

Guardado, L. R., L. A. P. Gamboa, and C. F. Lucchesi, 1989, Petroleum geology of the Campos basin, Brazil: A model for a producing Atlantic-type basin, in J. D. Edwards, and P. A. Santogrossi, eds., Divergent/passive margin basins: AAPG, vol. 48, 3–80.

Guardado, L. R., A. R. Spadini, J. S. L. Brandão, and M. R. Mello, 2000, Petroleum system of the Campos Basin, in M. R. Mello, and M. B. Katz, eds., Petroleum systems of South Atlantic Margins: AAPG, vol. 73, 317–324.

Guo, H., K. J. Marfurt, and J. Liu, 2009, Principal component spectral analysis: Geophysics, 74, no. 4, P35– P43.

Harris, P. M., 1979, Facies anatomy and diagenesis of a Bahamian ooid shoal: Miami, Florida: University of Miami Comparative Sedimentology Laboratory.

Harris, P. M., 1983, The Joulters ooid shoal, Great Bahama Bank, in T. M. Peryt, ed., Coated grains: Springer- Verlag, 132–141. Harris, P. M., 2010, Delineating and quantifying depositional facies patterns in carbonates reservoir: Insights from modern analogs: AAPG Bulletin, 94, 61–86.

Hart, B. S., 2008, Channel detection in 3-D seismic data using sweetness: AAPG Bulletin, 92, 733–742.

Horschutz, P. M. C., L. C. S. Freitas, C. V. Stank, A. S. Barroso, and W. M. Cruz, 1992, The Linguado, Carapeba, Vermelho, and Marimbá Giant Oil Fields, Campos Basin, Offshore Brazil, in M. T. Halbouty, ed., Giant oil and gas fields of the decade 1978–1988: AAPG, vol. 54, 137–156.

Kohonen, T., 2001, Self-organizing maps: Springer-Verlag.

Kuroda, M. C., A. C. Vidal, E. P. Leite, and R. D. Drummond, 2012, Electrofacies characterization using self-organizing maps: Revista Brasileira de Geofísica, 30, 287–299.

Lucia, F. J., 2007, Carbonate reservoir characterization: Springer.

Marfurt, K. J., V. Sudhaker, A. Gersztenkorn, K. D. Crawford, and S. E. Nissen, 1999, Coherency calculations in the presence of structural dip: Geophysics, 64, 104–111.

Matos, M. C., K. J. Marfurt, P. R. S. Johann, J. A. Rosseto, A. T. A. Lourenço, and J. L. Diniz, 2009, Wavelet transform Teager-Kayser energy applied to a carbonate field in Brazil: The Leading Edge, 28, 708–713.

Partyka, G., J. Gridley, and J. Lopez, 1999, Interpretational applications of spectral decomposition in reservoir characterization: The Leading Edge, 18, 353–360.

Ponte, F. C., and H. E. Asmus, 1976, The Brazilian marginal basins: Current state of knowledge: Anais da Academia Brasileira de Geociências, 48, 215–239.

Posamentier, H. W., R. J. Davies, J. A. Cartwright, and L. J. Wood, 2007, Seismic geomorphology: An overview, in R. J. Davies, H. W. Posamentier, L. J. Wood, and J. A. Cartwright, eds., Seismic geomorphology: Applications to hydrocarbon exploration and production: Geological Society London Special Publication, 277, 1–14.

Radovich, B. J., and R. B. Oliveros, 1998, 3-D sequence interpretation of seismic instantaneous attributes from the Gorgon field: The Leading Edge, 17, 1286–1293

Rangel, H. D., F. A. L. Martins, F. R. Esteves, and F. J. Feijó, 1994, Bacia de Campos: Boletim de Geociências da Petrobras, 8, 203–217, http://vdpf.petrobras.com.br/vdpf/index.jsp.

Ravenne, C., A. Galli, B. Doligez, H. Beucher, and R. Eschard, 2002, Quantification of facies relationships via proportion curves, in M. Armstrong, C. Bettini, N. Champigny, A. Galli, and A. Remacre, eds., Geostatistics Rio 2000: Springer, 19–39.

Reeder, S. L., and E. C. Rankey, 2008, Interactions between tidal flows and ooid shoals, northern Bahamas: Journal of Sedimentary Research, 78, 175–186

Seifert, D., and J. L. Jensen, 1999, Using sequential indicator simulation as a tool in reservoir description: Issues and uncertainties: Mathematical Geology, 31, 527–550

Spadini, A. R., 1992, Processos deposicionais e ciclicidade em carbonatos albianos de plataforma rasa da Bacia de Campos: M.S. thesis, Universidade Federal do Rio de Janeiro.

Spadini, A. R., F. R. Esteves, D. Dias-Brito, R. L. M. Azevedo, and R. Rodrigues, 1988, The Macaé Formation, Campos Basin, Brazil: Its evolution in the context of the initial history of the South Atlantic: Revista Brasileira de Geociências, 18, 261–272.

Srivastava, R. M., 1994, An overview of stochastic methods for reservoir characterization, in J. M. Yarus, and R. L. Chambers, eds., Stochastic modeling and geostatistics: Principles, methods, and case studies: AAPG, Computer Applications in Geology, no. 3, 3–16.

Tucker, M. E., and V. P. Wright, 2008, Carbonate sedimentology: Blackwell Science. Wang, Z., Y. C. Yin, T. Fan, and X. Lei, 2012, Seismic geomorphology of a channel reservoir in lower Minghuazhen Formation, Laizhouwan subbasin, China: Geophysics, 77, no. 4, B187–B195.

Winter, W. R., R. J. Jahnert, and A. B. França, 2007, Bacia de Campos: Boletim de Geociências da Petrobras, 15, 511–529, http://vdpf.petrobras.com.br/vdpf/index.jsp.

Wright, P., 2008, Carbonate sediments and limestones: Constituents, in W. Tucker, and V. P. Wright, eds., Carbonate sedimentology: Blackwell Science, 1–27.

CHAPTER 4: SIMILARITY ATTRIBUTES FROM DIFFERENTIAL RESOLUTION COMPONENTS

Bruno César Zanardo Honório[1], Ulisses Correia[2], Marcílio Castro de Matos[3] and Alexandre Campane Vidal[1]

[1] University of Campinas – UNICAMP, Department of Geology and Natural Resources, Campinas, Brazil; E-mail: brunohonorio@gmail.com; vidal@ige.unicamp.br

[2] University of Campinas – UNICAMP, Department of Petroleum Engineering, Campinas, Brazil; E-mail: ulisses@dep.fem.unicamp.br

[3] SISMO Research & Consulting, Rio de Janeiro, Brazil and The University of Oklahoma, Norman, Oklahoma, USA. E-mail: marcilio@matos.eng.br

This paper is accepted and will be published by SEG journal Interpretation in February 2017.

doi: 10.1190/INT-2015-0211.1

ABSTRACT

Seismic resolution plays an important role in the delineation of structural and stratigraphic features. The resolution improvement directly affects the seismic attributes and, consequently, the interpretation of a given feature. However, the broadband data do not necessarily provide the best insight for seismic attribute evaluation. Particularly, geological discontinuities, such as karsts, faults and fractures, can have different seismic expressions according to their intrinsic scales and, therefore, they are better illuminated in a given frequency range. To extract dissimilar characteristics in different frequency bands, we have combined a recently developed spectral enhancement method based on differential resolution (DR[1]) and similarity attribute. The DR algorithm is simultaneously used for frequency enhancement and as a pseudo-filter, allowing us to compute similarity attribute at different frequency bands. The similarity computation follows the reflector dip of each DR sub-band and adjusts its analysis window accordingly to the dominant frequency within the sub-bands. Then, the sub-band similarities are combined in the red-green-blue-alpha (RGBα) color space, allowing a more detailed view of the geology under investigation. Although more expensive in terms of processing time because of all the steps needed for each sub-band, the proposed strategy proved to be a great improvement over the conventional procedure of detecting and delineating discontinuities in fault and karst structures, when treating seismic data from an offshore carbonate field in Campos Basin, Brazil.

[1] DR here is used with a different meaning from the chapter 2, which states for “dimension reduction”

INTRODUCTION

The relatively low dominant frequency of conventional amplitude seismic data limits the visualization of structural details. In general, as greater bandwidth implies higher resolution, the application of processing techniques to broaden the seismic record spectrum is a common and useful approach to resolve subtle features, such as minor faults and karsts. Nowadays, resolution enhancement has become a hot topic in this field of seismic research. Enhancing seismic resolution allows a more refined structural and stratigraphic interpretation. Such refinement is vital in complex geologic settings, as the ones encountered on carbonate reservoirs, but it is equally true for any scenario where a detailed analysis is needed.

Broadly speaking, resolution improvement algorithms fall into spectral balancing and inverse Q-filtering approaches (Fraser and Neep, 2004; Puryear and Castagna, 2008; Matos and Marfurt, 2011; Wang, 2006; Braga and Moraes, 2013; Zhou et al., 2015). Regardless of the technique applied to this finality, the seismic resolution improvement will affect directly the quality and reliability of the seismic attributes extracted from it. Chopra and Marfurt (2007) show that the seismic attribute calculated from a data set with limited resolution can overlook the delineation of subtle reservoir features. On the other hand, Zhou et al. (2015) demonstrate how resolution improvements have a positive impact on seismic data when it comes to coherence, energy, curvature, and frequency attributes, allowing a more accurate interpretation of fault and channel edges.

Usually, the most broadband data is preferred for interpretation. However, the broadband data do not necessarily provide the best insight for seismic attribute evaluation. In fact, the seismic response of a given geologic structure and, consequently, the seismic attributes calculated from it, has a different seismic expression at different frequency bands (Li and Lu, 2014). Al-Dossary and Marfurt (2006), for example, evaluated how long- and short-wavelength curvature attributes impact the delineation of geologic features of different scales. Sun et al. (2010) showed how discrete frequency coherence cubes can detect faults and fracture zones not easily seen through the full spectrum coherence data, particularly when focusing on the high frequency band of the data. Hardage (2015), on the other hand, demonstrate a better fault illumination considering only the lowest octave of the seismic spectrum (8-16Hz). Thus, spectral decomposition and red-green-blue (RGB) color-stack have been proven to be useful techniques to extract and display geological features at different spectral bands.

Although there is useful information in the instantaneous spectral attributes, the exact frequency range that produces an optimal image of a target varies according to target size, depth, thickness and impedance properties (Hardage, 2009). Additionally, it is not easy for interpreters to individually evaluate all possible iso-frequency volumes, making the choice of optimum components subjective and unclear (Liu and Marfurt, 2007). There are techniques that circumvent this "problem" somehow by using mathematical approaches, such as the average of three non-overlapping spectral bands (Stark, 2006); the use of three predetermined basis functions, producing a more continuous and overlapped spectral bands (Liu and Marfurt, 2007); or the use of projections in a multidimensional space (Guo et al., 2009; Honório et al., 2014).

In the present work, we demonstrate how a recently developed spectral enhancement method based on differential resolution (DR- Sajid and Ghosh, 2014) can be used as a pre-processing technique to compute similarity attribute at different frequency bands, which we call Differential Resolution Similarity (DRS). To do so, we first review the concepts of the DR method. Then, we propose an approach to compute and combine the similarity attribute from different spectral bands honoring their frequency content as a guide for windowing. Finally, we apply the proposed strategy to enhance delineation of geological features using seismic data from an offshore carbonate field in Campos Basin, Brazil.

DIFFERENTIAL RESOLUTION AND SIMILARITY

In this section, we introduce the proposed method and briefly highlight the parameters involved. The DR method adds different versions of the seismic trace to the original one. In order to keep the main behavior of the signal, the first term to be added is the smoothed version Y^S of the normalized original signal Y, which is obtained by 10 passes of a three-point smoother with weights [1 2 1]. The normalization is discussed in the sequence. Then, the normalized second-, fourth-, and sixth-order differentiated version of the trace, denoted by Y^{II}, Y^{IV} and Y^{VI}, respectively, are added:

$$r = Y + Y^S - Y^{II} + Y^{IV} - Y^{VI}, \quad (1)$$

where r is the non-normalized DR. The negative signal in equation 1 is to correct the phase shift introduced by differentiation. The fourth order difference has normal polarity while the second and the sixth order differences have reverse polarity. The effect of adding the smoothed trace is to boost low frequencies, while adding the three

difference traces highlights higher frequencies successively. The combination of these components enhances the entire bandwidth of the data.

Using the Fourier properties and theorems, we can better understand the effect of differentiation in the DR method. Denoting $F(\omega)$ as the Fourier transform of the differentiable signal $f(t)$, prime to the derivative with respect to time and i as the imaginary unit, the successive derivatives of $f(t)$ are:

$$\begin{aligned} f'(t) &\Leftrightarrow i\omega F(\omega), \\ f''(t) &\Leftrightarrow -\omega^2 F(\omega), \\ &\cdots \\ f''''(t) &\Leftrightarrow \omega^4 F(\omega), \\ &\cdots \\ f''''''(t) &\Leftrightarrow -\omega^6 F(\omega), \end{aligned} \tag{2}$$

which progressively boosts the higher frequencies according to the derivative order. Additionally, it is straightforward to understand the negative signals in the sub-bands stacking in equation 1.

The amplitude normalization for each version of the trace X is performed according to its median of the absolute value $|\tilde{X}|$:

$$Y = \frac{X}{|\tilde{X}|}, \tag{3}$$

where Y is the normalized seismic trace. To obtain a normalized DR, denoted by R, r is also normalized according to equation 3.

The differentiation is obtained by difference operators for efficiency. In the algorithm proposition, a combination of one forward and one backward difference is done in order to not introduce a time shift. Although the algorithm works well in terms of computational efforts and precision, we have refined this procedure by performing a forward difference for the first sample, a backward difference for the last sample and the central difference for all the intermediate samples:

$$y'_j \cong \frac{y_{j+1} - y_j}{\Delta t} \left(j \in R(j = 1)\right). \quad forward \tag{4}$$

$$y'_j \cong \frac{y_j - y_{j-1}}{\Delta t} \left(j \in R(j = n)\right). \quad backward \tag{5}$$

$$y'_j \cong \frac{y_{j+1} - y_{j-1}}{2\Delta t} \left(j \in R(1 < j < n - 1)\right). \quad central \tag{6}$$

The reason for this is that the truncation error for the backward and forward difference is $O(\Delta t)$, while the truncation error for the central difference is $O(\Delta t^2)$, which

yields a more accurate approximation. Although the truncation error can drop to $O(\Delta t^2)$, after one backward and one forward differentiation by applying the central difference, we reduce by half the number of calculations and the computing time, which can be significant when working with large 3D seismic volumes. The n^{th}-order difference is approximated by applying n successive differences on the signal $y(t)$.

Figure 4. 1 shows a synthetic signal and the results of the main steps of the DR method. In Figure 4. 1a, the event I is a single interface transition, while events II-VI represent thin-beds from 6 to 14 ms thicknesses (2 ms-thickness increments). The representation of the seismic trace generated by applying a 35Hz Ricker wavelet is shown in Figure 4. 1b. The output of the DR algorithm, R, is shown in Figure 4. 1c. The corresponding spectra for the signals in Figure 4. 1a and Figure 4. 1b are illustrated in Figure 4. 1f.

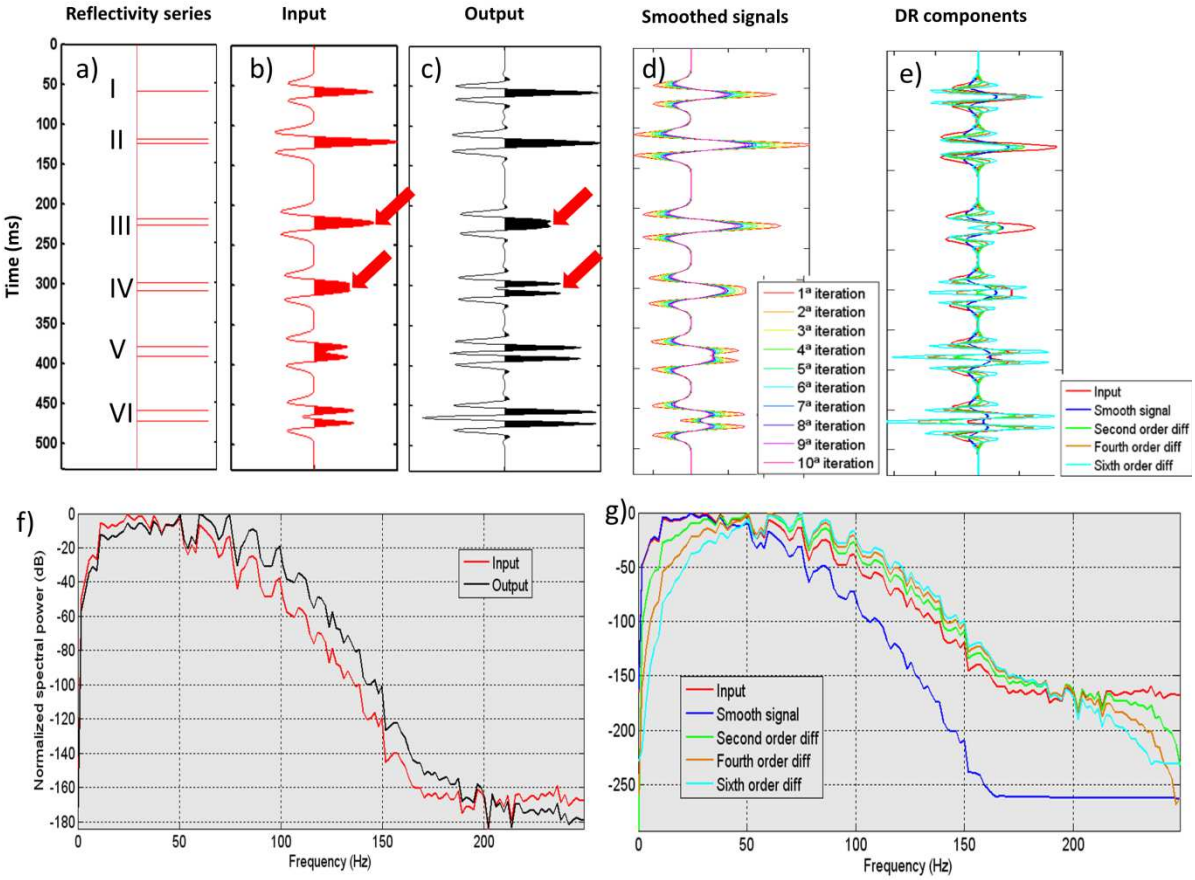

Figure 4. 1: Illustration of the DR method. (a) Reflectivity series; b) seismic trace; (c) DR output; (d) and (e) are the components used for signal reconstruction in the DR method; (f) spectra from (b) and (c); (g) spectra from (e).

It is clear from Figure 4. 1c the resolution improvement obtained from DR algorithm. The constructive interference that occurs between the top and base of thin-beds III and IV in the original seismic trace (red arrows) could suggest a single interface transition, which is not true. From checking the output of the DR algorithm, we can clearly discriminate the two interfaces in IV (separated by 5 samples or 10 ms thickness), and get a glimpse about the thin-bed III (four samples or 8 ms thickness). Also, note the frequency shift that occurs as we move from Y^S to Y^{VI} (Figure 4. 1g), which is the base for our algorithm.

As mentioned before, the seismic response of a given geologic structure is expressed differently at different spectral bands. Thus, instead of reconstructing the signal with extended bandwidth according to equation 1 and 3 as the DR algorithm does, we extract the similarity attribute for each DR component. In this way, the DR algorithm is used as a pre-processing procedure and acts as a pseudo-filter to be used for similarity computation. Because we want to combine the attributes in the RGBα color-space, we are limited to four variables. Thus, we can combine Y and Y^S as a new variable Y^{NS} according to equation 3, what accounts to the general behavior of the data, i.e, the low frequency content. Next, in a step called dip-steering, we extract the local dip information at every sample position for each DR component in order to guide the attribute extraction along the reflectors.

Considering that each derivative shifts the frequency spectrum to higher frequencies, the seismic wavelets become tighter as we move to higher order differences. Therefore, we can use a different analysis window honoring the peak frequency of each DR component to extract the similarity attribute, in a similar way as proposed by Lin et al. (2014). In our case, we determine the peak frequency f_{peak} for each time sample inside a 400 ms interval, 200 ms above and below the key horizon. Then, we calculate the mean peak frequency $\overline{f_{peak}}$ of each DR component to determine the half-window height H_{gate} for the similarity computation:

$$H_{gate} = \frac{\beta}{2\,\overline{f_{peak}}}\ , \tag{7}$$

where β is a refinement parameter that can be used to adjust the actual window size, depending on data quality, thus giving a flexibility to the workflow. In our simulations, we set the β-value as 1, but it can be adjusted to greater values if signal-to-noise is judged to be too low or, equivalently, if the detected discontinuity is noise-influenced.

The final step is to compute the similarity for each sub-band and combine them in the RGBα color-space. The α-channel (transparency) of the RGBα color-space goes from 0 (fully transparent) to 255 (fully opaque), so the lowest similarity or completely dissimilar feature appears as the background color, which is black in our case. The proposed workflow is summarized in Figure 4. 2.

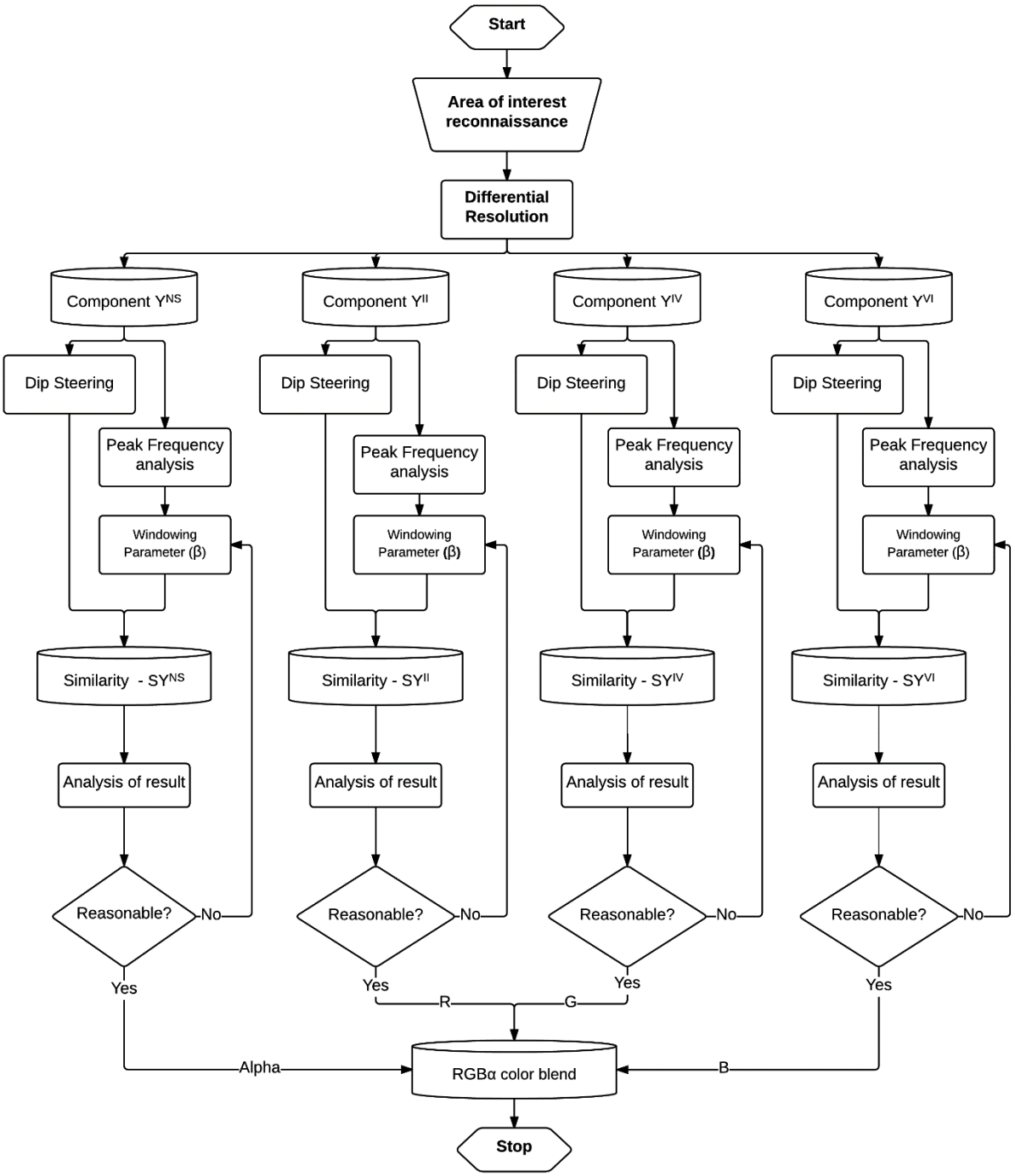

Figure 4. 2: Differential resolution similarity workflow.

RESULTS AND DISCUSSION

We start our study by first analyzing the effect of applying the DR algorithm and how the frequency content varies within each DR component. Figure 4. 3 displays a random seismic section and the average spectra for the corresponding volume. The green line represents a key horizon (H1) in our study. Comparing the spectrum of the original (plus curve) and the R data (circle curve), we can see a considerable gain in the frequencies above 30Hz. Additionally, note how the spectrum of each DR component (solid lines) fit in the R spectrum. The high frequency gain seen in the R volume spectrum helps to delineate some subtle features not properly seem in the original data, as the features highlighted by the white arrows in Figure 4. 3a and Figure 4. 3b. By evaluating the subsequent sections of Figure 4. 3, we can track back which DR component or sub-band better illuminates a given feature. Because the derivatives operations make the seismic wavelets progressively tighter, the tuning effects migrate to thinner thickness, helping to discriminate reflections previously merged in the original data, as the one pointed by the white ellipses in Figure 4. 3. Thus, considering that each DR component highlights slightly different information, we can adjust the similarity computation accordingly and get a final image with improved discontinuity detection and delineation.

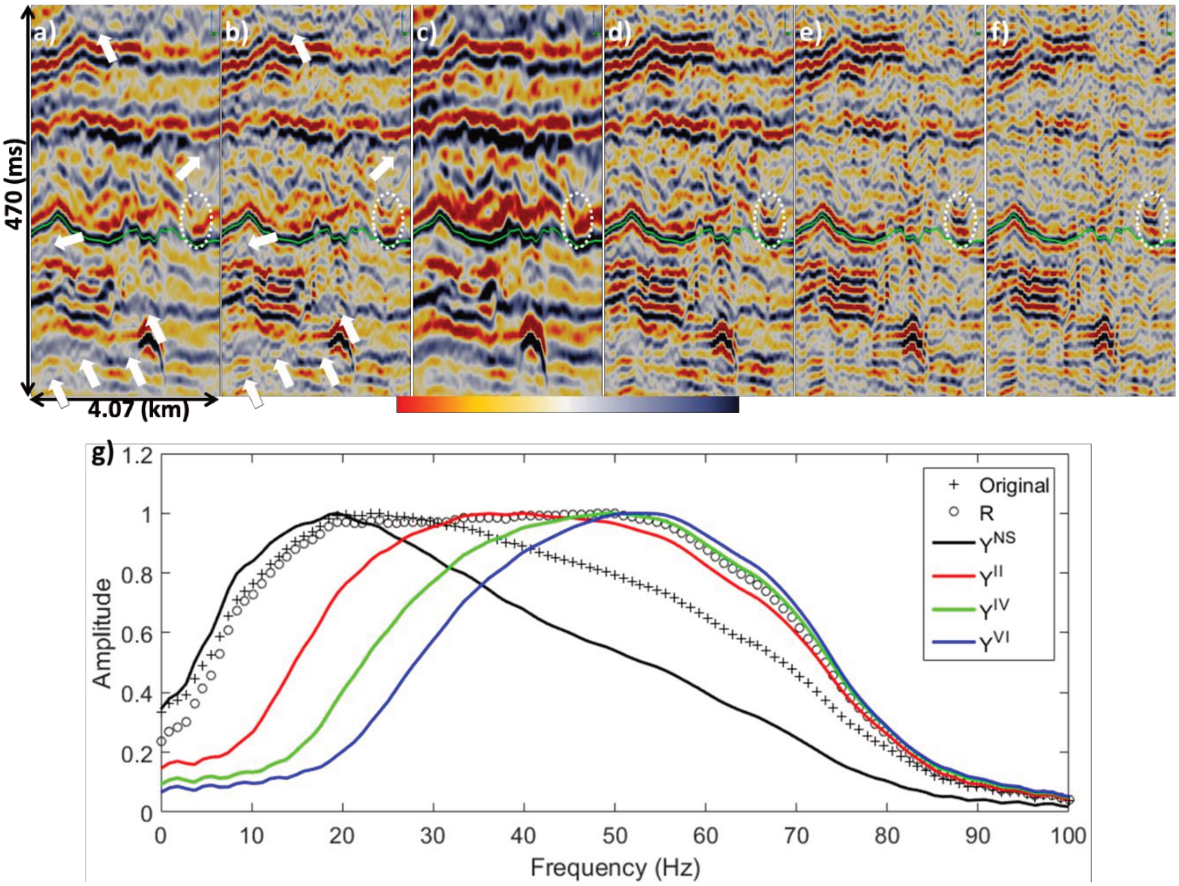

Figure 4. 3: Seismic sections and spectra: (a) original amplitude; (b) DR output; (c-f) are the components Y^{NS}, Y^{II}, Y^{IV}, Y^{VI}, respectively; (g) corresponding spectra from a-f. The green line represents the key horizon H1.

Figure 4. 4 shows the application of DRS to a real seismic data from a Brazilian carbonate offshore field in Campos Basin. Figure 4. 4a-d display the horizon H1 through the similarity attribute extracted from the DR components (SY^{n}) separately, while Figure 4. 4e displays its RGBα color-stack. The time window for the similarity computation varies from 22 ms for SY^{VI} to 40 ms for SY^{NS}. The red arrows in Figure 4. 4a-d show features that are better seen in the derivatives components, which suggest that they have smaller scale. The green arrows, on the other hand, show features that are more evident in the lower frequency band (SY^{NS}). We can see a slight noise increase as we go from SY^{NS} to SY^{VI}, but this is justified by the gain we have in the definition and resolution of some subtle structures. The color interpretation in the RGBα also gives us an idea about the scale of the features. For example, note the subtle feature highlighted by the blue arrow in Figure 4. 4. In the RGBα display, this feature is slightly red, which means that the discontinuity is captured mostly in the green and blue channel (see Figure 4. 4c-d), but poorly seen in the red-channel (see Figure 4. 4b) and not seen at all

in the α-channel (see Figure 4. 4a). In other words, this suggests a small feature that is not detected by SY^{II} and SY^{NS}, thus appearing continuous in the red- and α-channels.

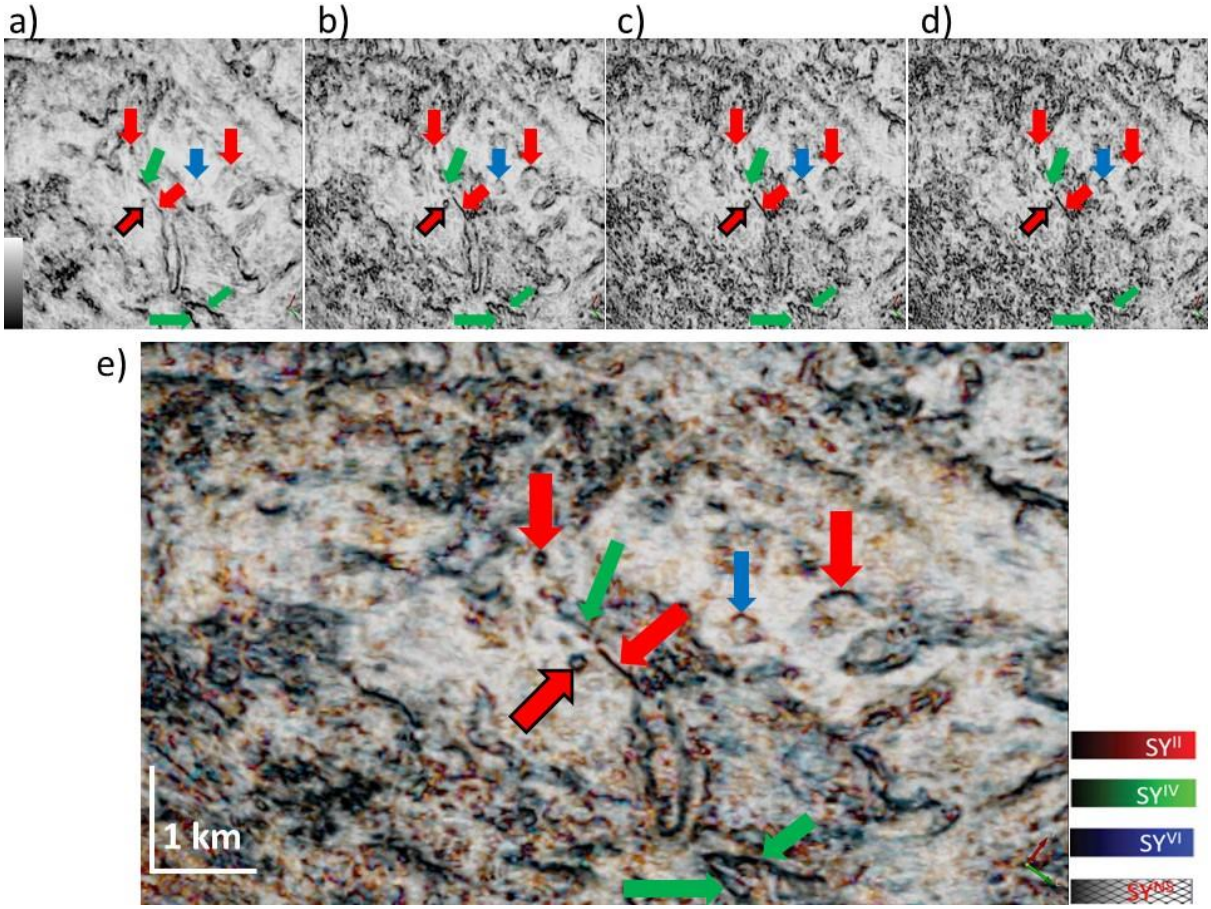

Figure 4. 4: Differential Resolution Similarity computed for H1. (a-d) Similarity from Y^{NS}, Y^{II}, Y^{IV}, Y^{VI}, respectively; (e) RGBα color-stack of SY^{II}, SY^{IV}, SY^{VI} and SY^{NS}.

For comparison, in Figure 4. 5 we show the similarity attribute computed directly using the original seismic volume, which we call base model, and by applying the proposed strategy. We also evaluate the effect of computing the similarity directly in the bandwidth extended volume, R, to demonstrate the effect of not considering the scale of each DR sub-band separately as we do in DRS. To make the comparison accordingly, for the computation of similarity attribute through the original and R volumes, the dip information is also extracted and the window size follows the peak frequency as described in equation 7, in accordance with what we do in DRS.

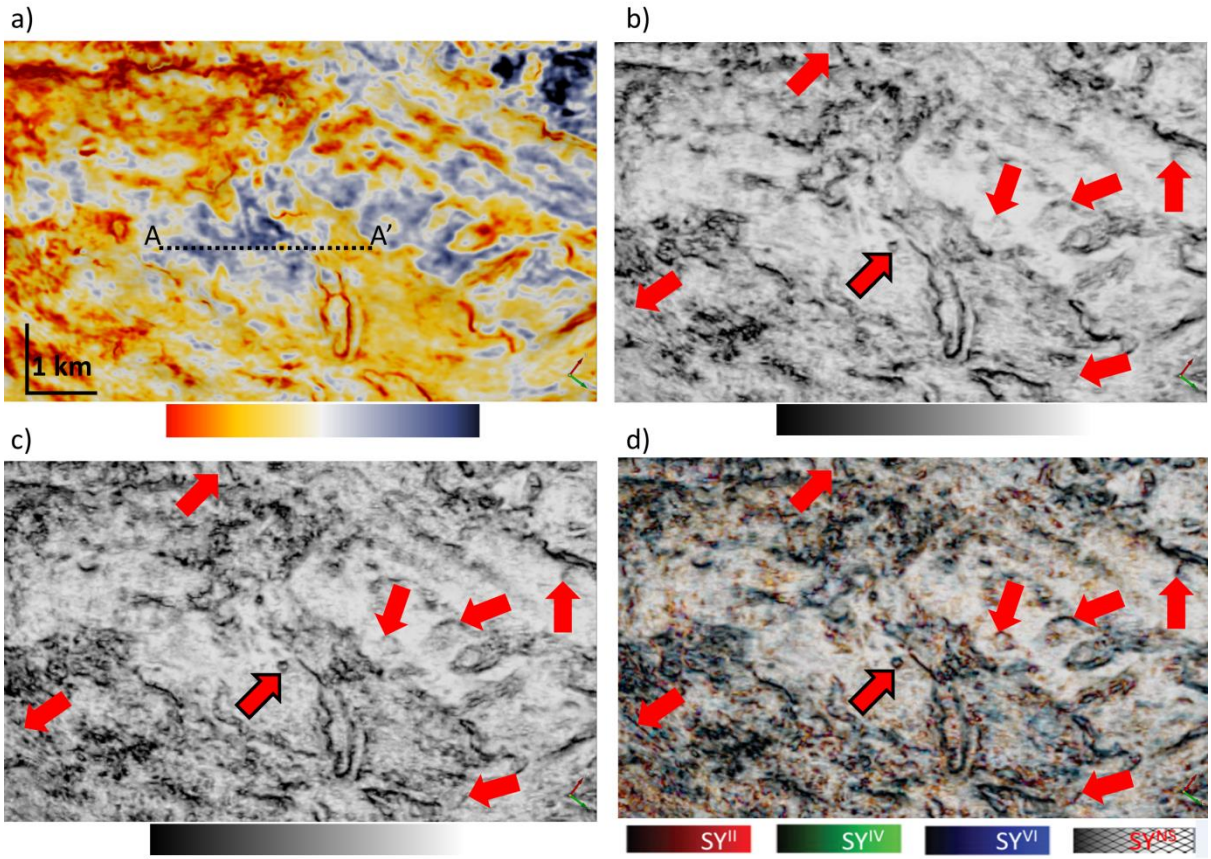

Figure 4. 5: Comparison of similarity attributes. Horizon H1 through (a) original seismic amplitude and the corresponding similarity attribute in (b); (c) Similarity from R; and (d) DRS.

A particular improvement occurs in the definition of the features pointed by the red arrows. The similarity extracted from the R volume (Figure 4. 5c) enables the detection of different features slightly over the original data (Figure 4. 5b). However, through the DRS, we can see a much better detection and definition of features in Figure 4. 5d. The leftmost arrow, for example, shows a subtle discontinuity that is well captured in DRS, poorly seen in similarity from R, and not seen at all in the similarity from the original data. The red arrow with black outline in the center is another similar example that pinpoints to a karst structure which is clearly seen in the DRS. A vertical section along A-A' profile in Figure 4. 5a crossing this structure through the base model and DRS data is shown in Figure 4. 6 and Figure 4. 7. Note that, although correlated, each DRS component illuminates and detects different structures. In the particular case of the pointed karst, its boundary is better detected in the SY^{II} (Figure 4. 6c2), a sub-band dominated by approximately 40Hz in the amplitude data. Also note the discontinuities pointed by the blue arrows in the center column of Figure 4. 6. In the base model, such discontinuities are quite blurred. As we move down in the figure, we are able to see a

progressive better definition of the two fractures, which attests the DRS ability to illuminate features at different scales.

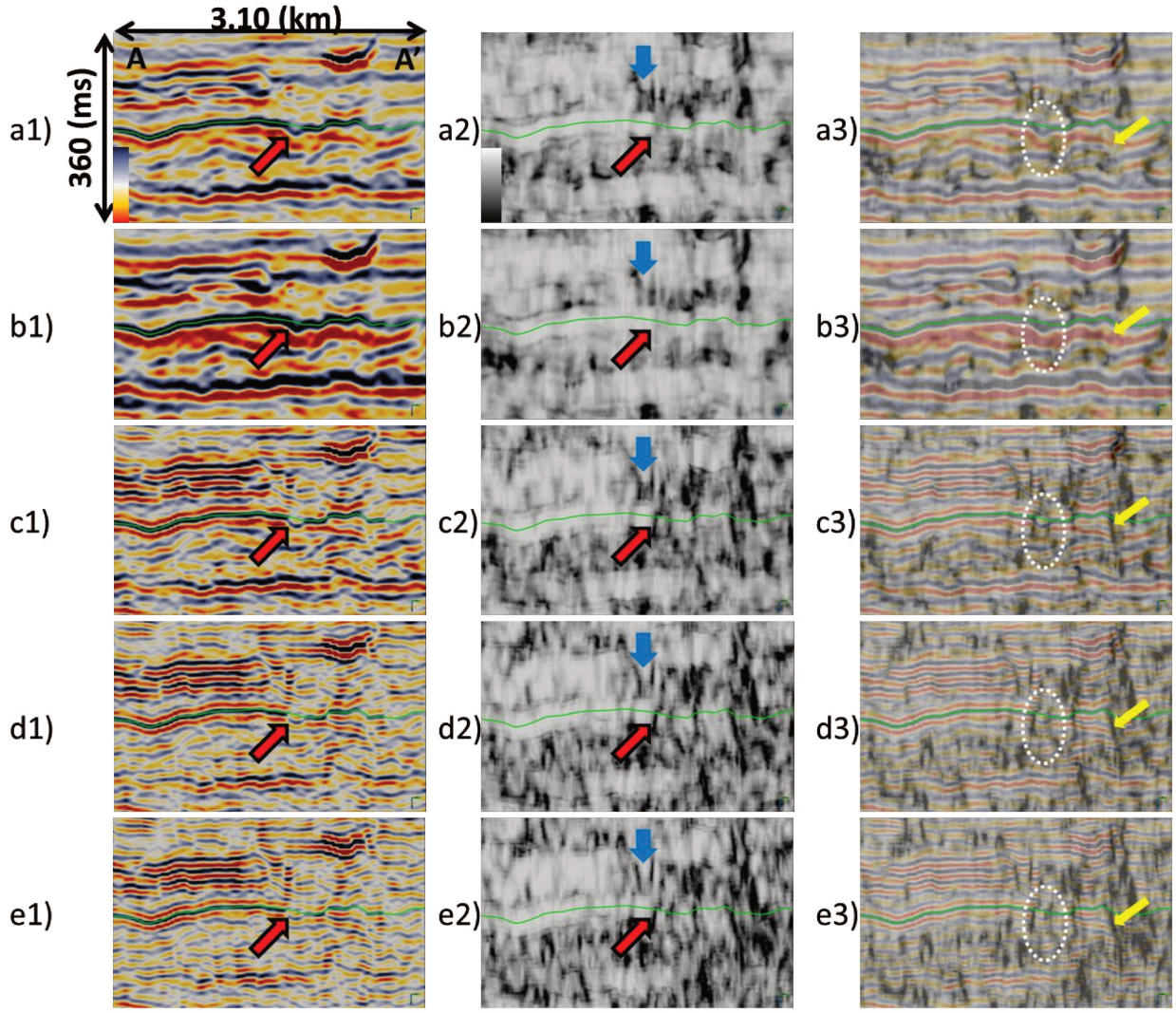

Figure 4. 6: Seismic section through amplitude data (left), similarity (middle) and amplitude/similarity co-rendered (right) from: (a) original; (b-e) DR components (Y^{NS}, Y^{II}, Y^{IV}, Y^{VI}), respectively. See Figure 5a for section reference location.

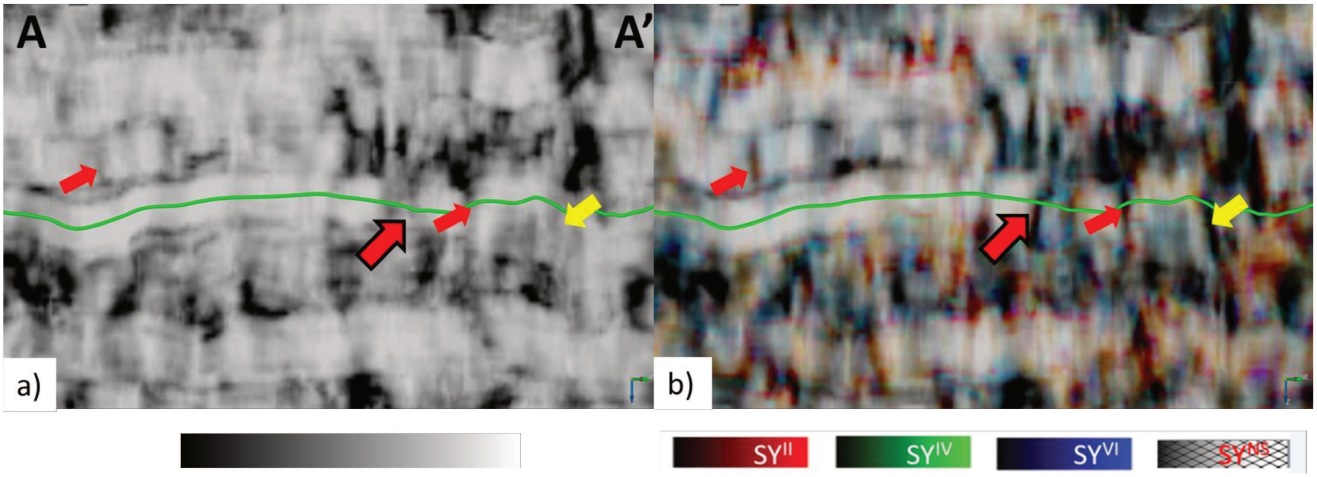

Figure 4. 7: Similarity comparison through (a) base model and (b) DRS.

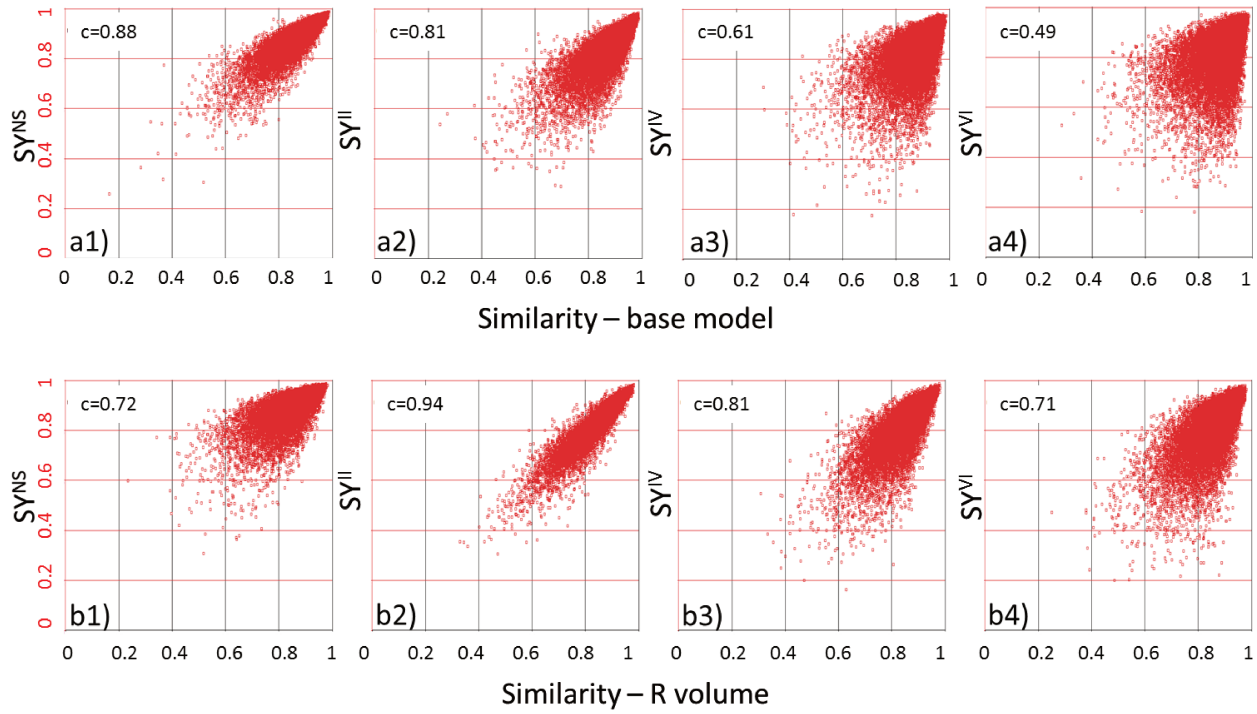

Figure 4. 8: Crossplots derived from the attribute maps of Figure 5. (a) DRS *versus* base model, and (b) DRS *versus* similarity from R volume.

In order to get a quantitative evaluation regarding the different procedures applied, we extracted the cross correlation between the DRS components and the base model (Figure 4. 8a), and between the DRS components and the similarity from R (Figure 4. 8b). Basically, the sample correlation coefficient (c) denotes the quality of least square regression fit between any two attribute vectors, and it is equivalent to a windowed zero-lag cross-correlation, where the window length is the entire attribute vector length. In Figure 4. 8a, the highest correlation occurs between the similarity from base model and SY^{NS}, which is related to the lowest frequency component in the DRS algorithm. As we move to higher frequency components in the DRS and, consequently, looking to smaller scale features, the cross correlation with the base model drops close to 50%. The components share half of information, but also another 50% of different information is present in SY^{VI}. Obviously, some noise can be accounted for this equation. Therefore, it is important to verify if such new information is geologically feasible, as the feature pointed by yellow arrows in the Figure 4. 6a3- 4.6e3 and Figure 4. 7, which clearly suggests a fault that is poorly seem in the base model but is well illuminated in DRS. A similar reasoning is drawn to the cross correlation between DRS components and the similarity from R. Except for the low frequency component, their correlation is higher than between the DRS components and the base model. Such analysis is in accordance

and is justified because of the intrinsic relationship between R and its components, which will impact the higher correlation between the attributes extracted from them. Note, for example, the high correlation between SY^{II} and the similarity from R (c = 0.94, Figure 4. 8b2), which occurs mainly because the corresponding amplitude data have almost the same dominant frequency (~40Hz, see Figure 4. 3g) and, consequently, the same window size is applied to similarity computation in both cases. This reinforces the importance of considering the scale of the feature we are dealing with and interested in. For the other sub-bands, their cross correlation drops close to 70%, suggesting that they are capturing different information.

CONCLUSIONS

If on one hand broadening the seismic spectrum is a logical step for seismic resolution improvement, on other hand we have to consider that such image is a composite of various geological structures which may have different scale ranges. Thus, if the scale of observation is not appropriate to the scale we are interested in, we risk an improper interpretation. An interpretation in a structurally complex setting, such as karst - or fault-related regions, can be very challenging to co-render different seismic attributes to highlight seismic features of interest. The scale range plays an important role in defining and identifying whether we are seeing a simple seismic feature or a subtle geologic structure.

In this way, we have combined a seismic spectral enhancement method based on differential resolution and similarity attribute in order to extract dissimilar features at different spectral bands. Because each DR component has a different frequency content, we can use different analysis windows to evaluate the discontinuity at a given frequency range. The combination of the DRS components in the RGBα color space helps to group the sub-bands discontinuities, allowing a more detailed definition of the structures under investigation.

Although more expensive in terms of processing time because of all steps needed in DRS, it proved to be a great improvement in discontinuity detection and delineation over the base model. Such improvement is especially important in complex scenarios where the discontinuities can vary in many different scales and be associated either with reservoir compartmentalization or migration pathways.

ACKNOWLEDGMENTS

We would like to thank Statoil for financial support and for allowing us to publish this study. We also thank the Brazilian Council for Technological and Scientific Development (CNPq, Brazil) for the support to this project by means of a Ph.D. scholarship for the first author and dGB Earth Sciences Company for providing OpendTect software through an academic license agreement. We are grateful for the multi-client seismic data provided by PGS. Sinochem is also acknowledged for the permission of this publication.

REFERENCES

Al-Dossary, S., and K. J. Marfurt, 2006, 3-D volumetric multispectral estimates of reflector curvature and rotation: Geophysics, **71** (5), P41–P51.

Braga, I. L. S. and F. S. Moraes, 2013, High-resolution gathers by inverse Q filtering in the wavelet domain: Geophysics, **78** (2), V53-V61.

Chopra, S. and K. J. Marfurt, 2007, Seismic attributes for prospect identification and reservoir characterization: SEG.

Fraser, G. B. and J. Neep, 2004, Increasing seismic resolution using spectral blueing and colored inversion: Cannonball field: Trinidad, 4th Annual International Meeting, SEG, Expanded Abstracts, 1794–1797.

Guo, H., K. J. Marfurt, and L. Liu, 2009, Principal component spectral analysis: Geophysics, **74** (4), P35-P43.

Hardage, B. A., 2009, Frequencies are fault finding factors: Looking low aids data interpretation: AAPG Explorer, **30** (9), 34.

Hardage, B. A., 2015, Pitfall experiences when interpreting complex structure with low-quality seismic images: Interpretation, **3** (1), SB29–SB37.

Honório, B. C. Z., A. C. Sanchetta, E. P. Leite, and A. C. Vidal, 2014, Independent component spectral analysis: Interpretation, **2** (1), SA21-SA29.

Li, F. and W. Lu, 2014, Coherence attribute at different spectral scales: Interpretation, **2** (1), 1–8.

Lin, T., B. Zhang, Z. Zhan, Z. Wan, F. Li, H. Zhou and K. J. Marfurt, 2014, Seismic attributes of time-vs. depth-migrated data using self-adaptive window: 84th Annual International Meeting, SEG, Expanded Abstracts, 1659-1663.

Liu, J. and K. J. Marfurt, 2007, Multicolor display of spectral attributes: The Leading Edge, **6** (3), 268-271.

Matos, M. C. and K. J. Marfurt, 2011, Inverse continuous wavelet transform "deconvolution": 81st Annual International Meeting, SEG, Expanded Abstracts, 1861–1865.

Puryear, C. I. and J. P. Castagna, 2008, Layer-thickness determination and stratigraphic interpretation using spectral inversion: theory and application: Geophysics, **73** (2), R37–R48.

Sajid, M. and D. Ghosh, 2014, A fast and simple method of spectral enhancement: Geophysics, **79** (3), V75–V80.

Stark, J., 2006, Visualization techniques for enhancing stratigraphic inferences from 3D seismic data volumes: First Break, **24**, 75-85.

Sun, D. S., Y. Ling, X. Y. Guo, J. Gao, and J. X. Lin, 2010, Application of discrete frequency coherence cubes in the fracture detection of volcanic rocks in full-azimuth seismic data: 80th Annual International Meeting, SEG, Expanded Abstracts, 1342–1346.

Wang, Y., 2006, Inverse Q-filter for seismic resolution enhancement: Geophysics, **71** (3), V51–V60.

Zhou, H., Y. Wang, T. L., F. Li, and K. J. Marfurt, 2015, Value of nonstationary wavelet spectral balancing in mapping a faulted fluvial system, Bohai Gulf, China: Interpretation, **3** (3), SS1–SS13.

CHAPTER 5: PROGRESS ON EMPIRICAL MODE DECOMPOSITION BASED TECHNIQUES AND ITS IMPACTS ON SEISMIC ATTRIBUTES

Bruno César Zanardo Honório[1], Marcílio Castro de Matos[2] and Alexandre Campane Vidal[1]

[1] University of Campinas – UNICAMP, Department of Geology and Natural Resources, Campinas, Brazil; E-mail: brunohonorio@gmail.com; vidal@ige.unicamp.br

[2] SISMO Research & Consulting, Rio de Janeiro, Brazil and The University of Oklahoma, Norman, Oklahoma, USA. E-mail: marcilio@matos.eng.br

This paper is accepted and will be published by SEG journal Interpretation in February 2017.

doi: 10.1190/INT-2016-0079.1

ABSTRACT

Spectral decomposition plays a significant role in seismic data processing and is commonly used to generate seismic attributes that are useful for interpretation and reservoir characterization. Among several techniques that are applied to this finality, the complete ensemble empirical mode decomposition (CEEMD) is an alternative procedure that has proven higher spectral-spatial resolution than the short-time Fourier transform or wavelet transform, thus offering potential to highlighting subtle geologic structures that might otherwise be overlooked. In this paper we analyze a recent development in CEEMD, which we call improved CEEMD (ICEEMD), and its impacts on seismic attribute analysis commonly used in the empirical mode decomposition (EMD) framework. By replacing the estimation of modes by the estimation of local means, the mode mixing and the presence of noise in the modes are reduced. Application on a synthetic and real data demonstrates that ICEEMD improve the signal decomposition and the energy concentration in the time-frequency domain, producing a better understanding of the analyzed signal and, consequently, of the geology under investigation.

INTRODUCTION

This paper aims to be the continuation and an update of Han and van der Baan (2013) work, which discuss the empirical mode decomposition method for seismic signal analysis and its suitability for seismic interpretation. The EMD (Huang et al., 1998) is an effective technique for nonstationary and nonlinear signal analysis. The EMD is an entirely data-driven process, decomposing the analyzed signal into elementary amplitude/frequency modulated harmonics, called intrinsic mode functions (IMFs), or simply modes. The IMFs are based on direct extraction of the energy associated with various intrinsic scales, which means that each IMF has different frequency content. The first IMF corresponds to the highest frequency harmonic in the signal, with decreasing frequency content in the subsequent IMFs. In terms of seismic signals analysis, such characteristic potentially highlights different structural and stratigraphic information. If signal reconstruction is needed, it can be done by simply summing the IMFs plus a final monotonic trend.

Due to the local nature of EMD method, it can produce oscillations with disparate amplitude in a mode or the presence of very similar frequency content in different modes. Such characteristic is known as mode mixing and can be viewed as a limitation of this method. To overcome this problem, some noise-assisted versions of EMD were proposed. Wu and Huang (2009) introduced the ensemble EMD (EEMD), which performs the decomposition over an ensemble of noisy versions of the original signal. Then, the IMFs are estimated simultaneously as the mean of all the correspondents IMFs. Although the EEMD aids better modes separation, different number of modes can be generated for different realizations of the noisy signal and the reconstructed signal does not perfectly reproduce the original one. In order to address these limitations, Torres et al., (2011) proposed the complete ensemble EMD with adaptive noise (CEEMD). For the first IMF, CEEMD performs as in EEMD. Then, a unique signal residual is obtained and treated as a new signal which is again perturbed with noisy realizations. In this way, the modes are extracted sequentially for subsequent decomposition stage. The resulting decomposition is complete in the sense that it provides an exact reconstruction of the original data (Torres et al., 2011).

Despite CEEMD can be considered an important improvement on EEMD and has encountered applications in many different fields, its modes can contain residual noise and the existence of spurious modes (Colominas et al., 2014) and, like other methods, it

still has limitations when the components are not well separated in the time-frequency plane. Although the residual noise can be canceled when summing the IMFs, thus leading to a reconstruction error about machine precision in CEEMD (Han and van der Baan, 2013), if we intend to use the modes separately as a preprocessing step for further applications (Matos and Marfurt, 2013; Du et al., 2015) or to compute instantaneous attributes, the presence of such noise in the IMFs can impact negatively.

First introduced in the biomedical signal processing context, an improved version of CEEMD (here named as ICEEMD) (Colominas et al., 2014) tries to reduce the presence of residual noise in the IMFs while keeping or even improving the reconstruction ability and the "unmixed modes" characteristic inherent to CEEMD method. By estimating the local mean of the noisy versions of the target signal and defining the true mode as the difference between the current residue and the average of its local means to estimate the IMFs, the ICEEMD generates modes with less residual noise and better mode separation. This property can be useful for seismic attributes calculation using the IMFs, generating more interpretable structural and stratigraphic framework. In fact, seismic waveform and attributes values are the most commonly used inputs in classification process. Because, in general, seismic facies analysis is sensitive to noise when waveform and its attributes serve as the input data to clustering analysis, extracting modes with less noise can aid more physical meaning to them and impact positively on the classification process. Additionally, time-frequency representation with good resolution is always desirable in a sort of geophysical application (Tary et al., 2014). This transformation can be done combining the modes of EMD (and variants) with complex signal analysis (Taner et al., 1979), which is known as Hilbert-Huang Transform (HHT) (Huang et al., 1998), or by any other time-frequency representation such as wavelet-based methods (Matos and Marfurt, 2013; Zhang et al., 2015). In this way, IMFs with less noise and well-conditioned in the time-frequency domain will be more physically meaningful, allowing a more realistic post-processing and a better understanding of the analyzed signal and, consequently, of the geology under investigation.

In terms of exploration geophysics, the EMD-based techniques are mostly applied for signal feature extraction and for seismic denoising. Magrin-Chagnolleau and Baraniuk (1999) call attention to the potentiality of obtaining time-frequency seismic attributes based on EMD. Huang and Milkereit (2009) use the EEMD to analyze the depth varying spectrum function of well logs to simulate locally stationary

heterogeneous petrophysical models. Liu et al. (2015) use the EMD and instantaneous frequency calculation to access the sedimentary cycle patterns in seismic data. Bekara and Van der Baan (2009) use the EMD to attenuate random and coherent seismic noise by eliminating the first IMF in the frequency-offset (*f-x*) domain. Similar to them, Chen et al. (2014) use the EMD in *f-x* domain to design a predictive filtering scheme for random noise attenuation in complex scenarios. By smoothing the seismic data via EMD in the flattened domain, Chen et al. (2015) improve the continuity of reflections events for both pre- and post-stack seismic data. Han and van der Baan (2015) use the EEMD and an adaptive thresholding scheme for microseismic denoising. Du et al. (2015) combine the EMD and self-organizing maps (SOM) for seismic denoising and waveform classification.

In this way, any improvement in the EMD-based techniques can impact positively this relatively new and vast field. Therefore, the present study has the main goal of evaluating the ICEEMD method in the context of seismic signal analysis and its impacts on attributes conventionally used in EMD-based framework, such as instantaneous amplitude, instantaneous frequency and peak frequency. The paper is structured as follow. First, we review the concepts of CEEMD and ICEEMD methods and some considerations regarding the instantaneous attributes calculation. Then, we have applied both techniques to a synthetic signal which has been previously used to evaluate the time-frequency representations from various methods (Tary et al., 2014). Finally, we have compared CEEMD and ICEEMD on a real seismic data from an offshore field in Campos Basin, Brazil.

THEORY

Brief recap on EMD and EEMD

The EMD extracts the IMFs recursively, from the most oscillatory one to the final monotonic trend. The decomposition scheme is based on the identification of the local maxima and minima of the analyzed signal, where a spline is fitted to define the upper and lower envelope, respectively. Then, the mean envelope is subtracted from the initial signal and the process repeat on the residual signal until the mean envelope is close enough to zero in the entire time series. This procedure is called sifting and defines the first IMF. The first IMF is then subtracted from the original signal and the same sifting process is applied to the residual signal to define the subsequent IMF. The stopping

criteria is reached when the extracted IMF has a small amplitude or becomes monotonic (Huang et al., 1998).

One of the attractiveness of the EMD is that there is no need to define a basis function to decompose the analyzed signal, contrary to Fourier and S-transform (sines and cosines), or wavelet transform (mother wavelet), which unavoidably "colors" the signal decomposition and the time-frequency representation, influencing the interpretation of the signal properties.

As stated earlier, EMD also suffers from its own limitations: mode mixing (one IMF containing different scales), mode splitting (the spread of one scale over different IMFs), aliasing (overlapping of IMF spectra caused by a sub-Nyquist nature of extrema sampling), and end-point artefacts (energy spreading due to the lack of extrema at the very beginning and end of a data) (Mandic et al., 2013).

Trying to accomplish the aforementioned limitation, the EEMD (Wu and Huang, 2009) is essentially a EMD combined with noise stabilization. The addition of white Gaussian noise artificially inserts new extrema points to the signal, enabling the EMD algorithm to evaluate all possible solutions in a finite neighborhood of the final answer. Thus, the IMFs are computed as the mean of each decomposition level through all the noise realizations. Although such procedure effectively reduces the mode mixing, it does not guarantee a perfect signal reconstruction. Additionally, there is no guarantee about the number of IMFs extracted for each noise realization, which complicates the calculation of the mean IMFs. Thus, the need of a more effective signal decomposition led to the development of different noise-assisted versions of the EMD.

Complete ensemble empirical mode decomposition

As our main goal is to evaluate and compare the CEEMD with its improved version, we will not further discuss the details and particularities of EMD and EEMD. The superiority of CEEMD over EMD and EEMD for seismic data analysis is demonstrated in Han and van der Baan (2013).

Let´s consider $x^{(i)} = x + w^{(i)}$ as a noisy version of x under the ith realization of white Gaussian noise $w^{(i)}$, and $E_k(.)$ the operator which produces the kth mode through EMD. Thus, the first CEEMD mode is estimated as:

$$IMF_1 = \frac{1}{I}\sum_{i=1}^{I} E_1(x + \varepsilon w_i), \quad (1)$$

where I is the number of realizations and ε is a fixed percentage of the injected Gaussian white noise. Then, the first residue r_1 is calculated as:

$$r_1 = x - IMF_1. \tag{2}$$

Now, r_1 plus different noise realizations are treated as an ensemble of the new signals and the first EMD mode is extracted from each noisy r_1. Then, the second CEEMD mode is estimated as the average of these modes:

$$IMF_2 = \frac{1}{I}\sum_{i=1}^{I} E_1\left(r_1 + \varepsilon E_1(w^{(i)})\right), \tag{3}$$

and the second residue is calculated as $r_2 = r_1 - IMF_2$. In this way, the IMFs are extracted sequentially, contrary to EEMD. This procedure continues until a stopping criterion is reached, usually when the last residue R has no more than two extrema and can be viewed as a monotonic trend. Thus, the signal reconstruction can be done by simply stacking the *K*-IMFs and the final residue R:

$$x = \sum_{k=1}^{K} IMF_k + R. \tag{4}$$

Improved Complete ensemble empirical mode decomposition

Let us recall the operator $E_k(.)$ and define the operator which produces the local means of the signal as $M(.)$. By recognizing that $E_1(x) = x - M(x)$ and defining $\langle . \rangle$ as the average of different realizations, the first CEEMD mode (equation 1) can be rewritten as:

$$IMF_1 = \langle E_1(x^{(i)})\rangle = \langle x^{(i)} - M\left(x^{(i)}\right)\rangle = \langle x^{(i)}\rangle - \langle M\left(x^{(i)}\right)\rangle \tag{5}$$

By estimating only the local means and subtracting it from the original signal, we can reduce the presence of noise in the modes, making them more feasible for further processing. In this way, the estimation of modes is replaced by estimation of local means and first ICEEMD mode is defined as:

$$IMF_1 = x - \langle M\left(x^{(i)}\right)\rangle \tag{6}$$

In the original formulation of CEEMD, the first IMF is calculated as the average of first modes of signal plus different white noise realizations, exactly as in the EEMD. The main difference is that, for CEEMD, a unique residue is calculated (equation 2) and the subsequent components are extracted in a deflationary way, contrary to EEMD

which extracts all the IMFs and then averaging each IMF. Although this elegant solution generates better performance of CEEMD over EEMD, a strong overlap occurs for the successive CEEMD modes. For example, to extract IMF_2, we decompose different versions of $r_1 + \varepsilon E_1(w^{(i)})$ (see equation 3). Thus, a better mode separation can be achieved if we consider to use $E_k(w^{(i)})$ to extract the *k*th mode instead.

Another point is that, because the energy of the noise in the *k*th residue (for *k*>1) is only a fraction of the noise injected in the beginning of the algorithm, the signal-to-noise ratio (SNR) between added noise and the residue increases with *k*. Thus, we can set our noise as *k*-level dependent $\beta_k = \varepsilon_k \, std(r_k)$.

Thus, the ICEEMD algorithm is structured as follow:

1) Calculate by EMD the local means of I noise realizations of $x^{(i)} = x + \beta_0 E_1(w^{(i)})$ to obtain the first residue $r_1 = \langle M(x^{(i)}) \rangle$.
2) For *k*=1, calculate the first mode as: $IMF_1 = x - r_1$
3) Calculate the second residue as the average of local means of $r_1 + \beta_1 E_2(w^{(i)})$, and define the second mode as: $IMF_2 = r_1 - r_2 = r_1 - \langle M\left(r_1 + \beta_1 E_2(w^{(i)})\right) \rangle$.
4) For *k*=3,…, *K*, calculate the *k*th residue as: $r_k = \langle M\left(r_{k-1} + \beta_{k-1} E_k(w^{(i)})\right) \rangle$,
5) Define the *k*th mode as: $IMF_k = r_{k-1} - r_k$ and go to step 4 for the next *k*.

Instantaneous Frequency

The frequency content of any signal plays a fundamental role in the understanding of the signal characteristics. For seismic data, such information is very important for processing and interpretation. In this way, in order to get an in-depth view on how the IMFs behaves for the two methods, we evaluate the dominant frequency from each IMF. Among many different methods for this finality, the instantaneous frequency (IF) has been widely used due to its fast calculation and superior vertical resolution. Although IF is a very common used concept in signal analysis, there are several different approaches to compute it (Huang et al., 2009) and new approaches are continuously developed (Huo, 2015), not being the main scope of the present work to contrast and compare those different techniques. In general, for EMD-based methods, the IF is computed using a combination of complex signal analysis through Hilbert transform of constituents IMFs and a differentiation of the estimated phase $\theta(t)$. For any signal $x(t)$ with its Hilbert transform $y(t)$, the analytic signal $z(t)$ is given by:

$$z(t) = x(t) + iy(t) \ = R(t)\, exp[i\theta(t)], \tag{7}$$

where $R(t)$ and $\theta(t)$ refer to the instantaneous amplitude and instantaneous phase, respectively. Instantaneous amplitude is also known as reflection strength or trace envelope and can be defined as:

$$R(t) = \sqrt{x^2(t) + \ y^2(t)}. \tag{8}$$

The IF is mathematically defined as the first derivative of $\theta(t)$ and, in order to prevent ambiguities due to phase unwrapping, a more stable form can be obtained by:

$$\omega_x(t) = \frac{1}{2\pi}\frac{d\theta(t)}{dt} = \frac{1}{2\pi}\frac{x(t)y'(t) \ - x'(t)y(t)}{x^2(t) + \ y^2(t)}, \tag{9}$$

where prime denotes derivative with respect to time.

Equations 8 and 9 are used to instantaneous amplitudes and frequencies computation for each IMF, producing a very sparse time-frequency representation of the analyzed signal. The complete operation is broadly known as Hilbert-Huang Transform (HHT).

Individual frequency components analysis remains possible. In a similar way as proposed by Marfurt and Kirlin (2001), the mean-frequency attribute summarizes the information contained in a spectral decomposition to generate the isofrequency volumes.

Application

Synthetic data

In this section, we compare CEEMD and ICEEMD to evaluate their performance for a synthetic signal $s\ (t)$ (Figure 5.1) composed by: two spectral harmonics with 35 and 15Hz (s1 and s2), one frequency-modulated harmonic of 65Hz (s3), one gliding harmonic between 15 and 155Hz (s4), and one Morlet atom with 113Hz as central frequency (s5). This signal has 8000 samples, recorded at 800 samples per second and have been previously evaluated in Tary et al. (2014), where specific equations to create it can be found.

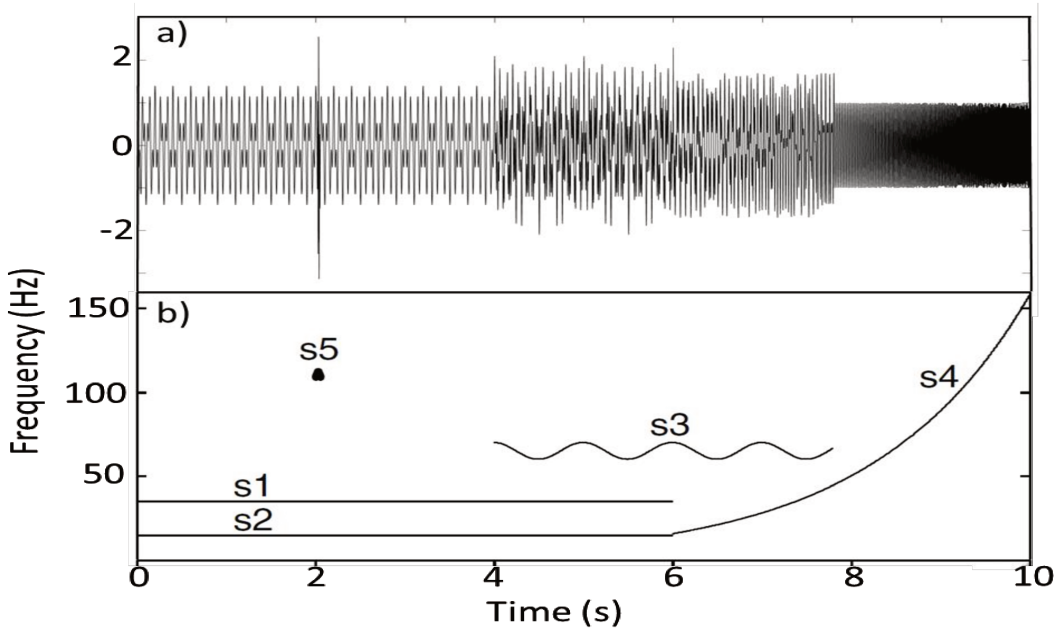

Figure 5.1: Synthetic signal for CEEMD and ICEEMD evaluation. (a) Signal; (b) Instantaneous frequency. (After Tary et al. 2014)

The first analysis we carried out is a qualitative evaluation in the IMFs extracted from $s\ (t)$, which are displayed on Figure 5.2. We have used 1000 noise-realizations and Gaussian white noise injection with 10% of the signal maximum amplitude for the two parameters needed for both methods. We can notice an expressive mode-mixing/splitting in the first three IMFs in the CEEMD method. The Morlet atom (s5 in Figure 5.1b) is captured mainly in the IMF1, but is also very consistent in IMF2 and less expressive but still present in IMF3. In the ICEEMD, the Morlet atom is mainly concentrated in the IMF1 with very low influence in subsequent ones. In addition, we can notice that the harmonic s3, which mainly captured in IMF3 for CEEMD, also perturbs the components IMF1 and IMF2. Those behaviors are consistent with the theoretical assumptions we did in the previous section. It is interesting to note that the IMFs are extracted in different frequency-dependent order for the two methods. For example, IMF3 from CEEMD is related with IMF2 from ICEEMD; IMF5 from CEEMD resembles the IMF4 from ICEEMD, but with more interference at the edge of the signal (between 6 and 7 seconds) for CEEMD. Also, note the interference between IMF4 and IMF5 in this time interval for CEEMD, which does not occur in ICEEMD.

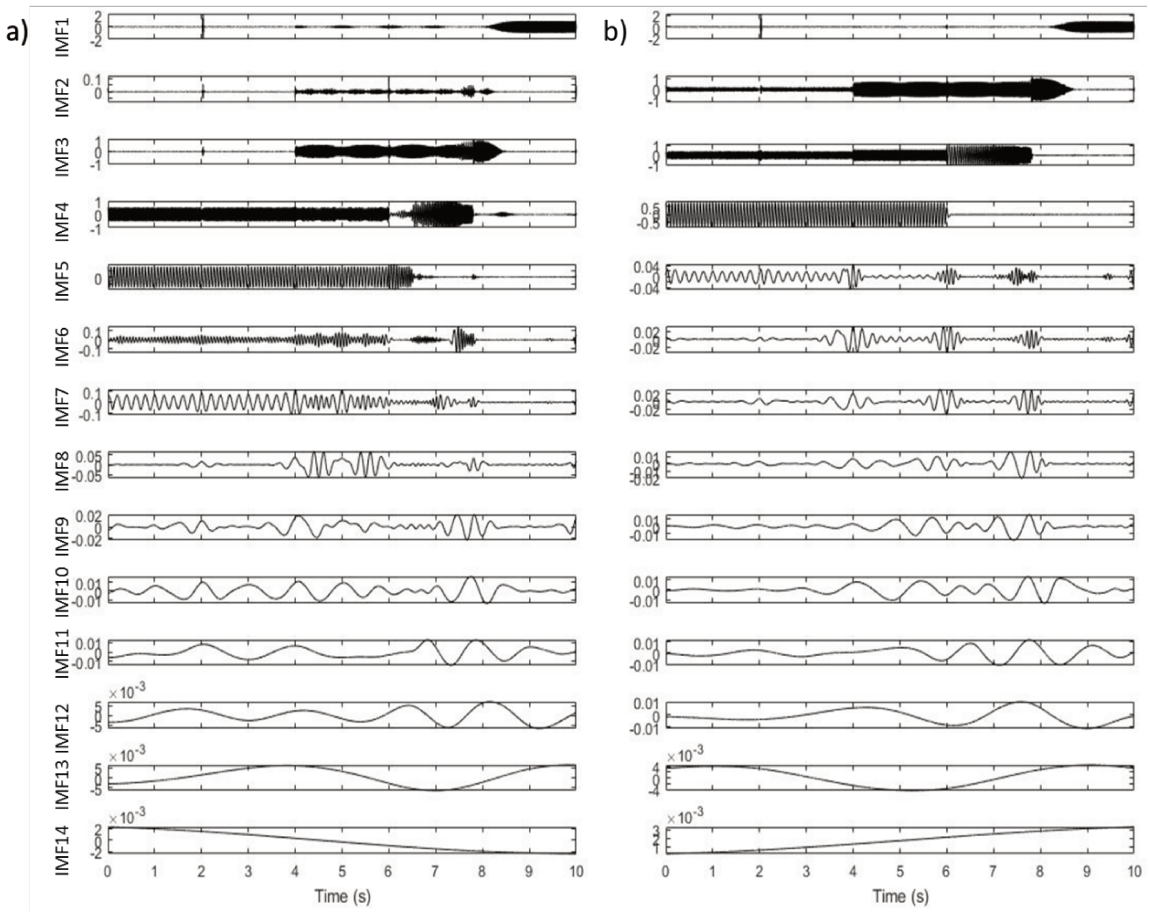

Figure 5.2: IMFs extracted from the synthetic signal $s(t)$, using (a) CEEMD; (b) ICEEMD.

Next, we evaluate the time-frequency representation through the HHT (Figure 5.3). We can note an improved IF detection and definition for the components extracted via ICEEMD. The colored boxes highlight time intervals where we can see the most expressive differences between the two methods. For CEEMD, the energy spreading is quite significant in some cases. For example, the red box highlights part of the 35Hz harmonic s1. In the CEEMD case, its energy spreads from 20Hz to 50Hz, while for ICEEMD, the IF is well localized in 35Hz ± 3Hz. Similar behavior can be identified for the green and blue highlighted boxes.

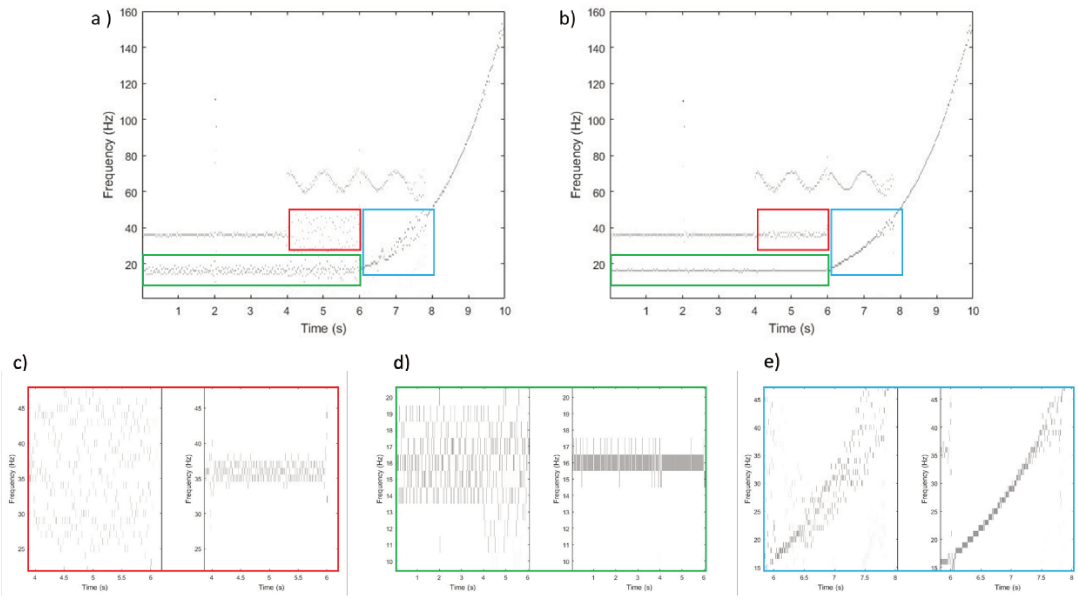

Figure 5.3: Time-frequency representation through HHT. (a) CEEMD; (b) ICEEMD. (c-e) zoom in the box-highlighted area, *left* for CEEMD, *right* for ICEEMD.

A more detailed visualization can be achieved by evaluating the time-frequency representation of each IMF separately (Figure 5.4). In order to facilitate our interpretation, we partially reconstruct the signal, i.e., we stacked the last nine components (IMF6 to IMF14). The components 1 to 5 are kept untouched. We can see some of the interferences we pointed out previously and new interpretations are also possible. For example, although the energy of s3 is more evident and better defined in IMF3 (Figure 5.4a3), it strongly interferes IMF2 (Figure 5.4 a2) and weaker energy can still be seen in Figure 5.4a1 (right-pointed arrows). A more critical influence of s3 occurs on IMF4, where it perturbs drastically the signal s1 around 5 seconds (down-pointed arrow) and the signal s4 (highlighted by the ellipse), responsible to the energy spreading around 30Hz. IMF2 from CEEMD is quite problematic. It poorly detects s3 and also receive some influence from part of s4. The left-pointed arrow shows the mode-mixing in IMF5 and IMF6 (Figure 5.4 a5 and Figure 5.4 a6). Additionally and more critical, note how noisy is the energy from the signal s2 in Figure 5.4 a5. For ICEEMD, the components are consistently captured and the influence on each other is very weak, which can lead to an improved signal characterization.

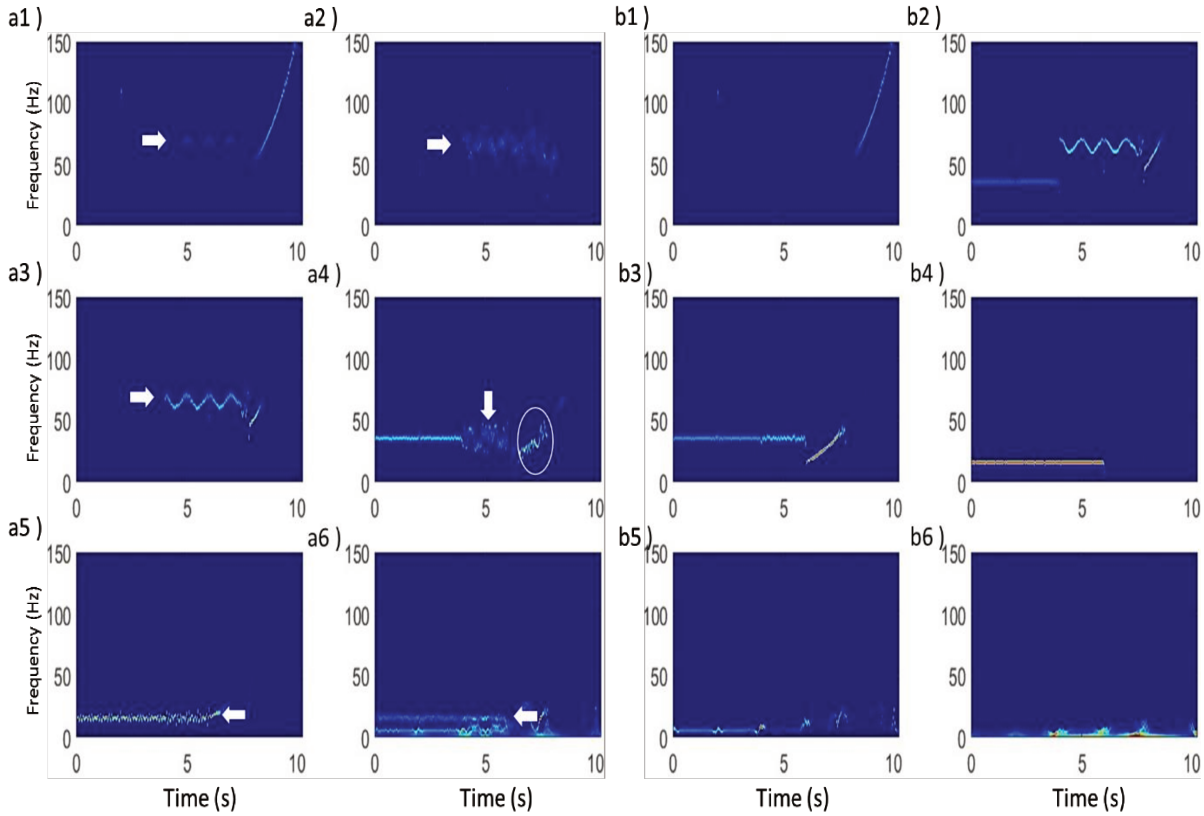

Figure 5.4: Time-frequency representations of each IMF. (a*i*) *i*th-IMF of CEEMD; (b*i*) *i*th-IMF of ICEEMD. (a6) and (b6) are extracted from the partially reconstruct signals using IMFs from 6 to 14; see text for details.

The next analysis we investigate is related to the reconstruction ability of the two methods. As can be noticed from Figure 5.5, both reconstructed signals are equally accepted with error about the machine precision, with an order of magnitude less in the error of ICCEMD method.

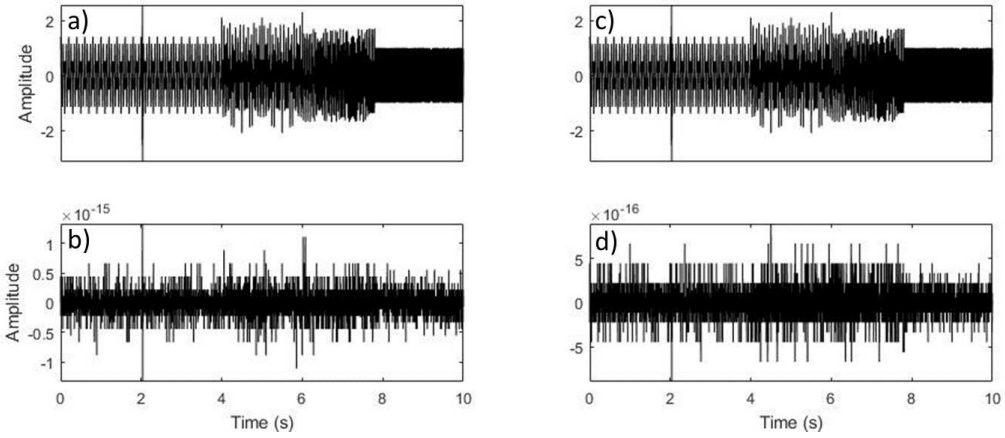

Figure 5.5: Reconstructed signal and error for (a-b) CEEMD and (c-d) ICEEMD, respectively.

Real data

Case study 1:

The next study we carried out is the analysis of the seismic trace on the common mid point (CMP) 81 from the Han and van der Baan (2013) work (Figure 5.6a). Because this signal is already analyzed by the EMD point of view, this approach aims to facilitate and promote a fairer comparison between the two methods. The same parameters are used for them, 50 realizations of 10% Gaussian white noise. Usually, it is useful to apply a 2-D Gaussian smoothing filter in order to better display the time-frequency representation. We have used a 5x5 Gaussian filter to this finality.

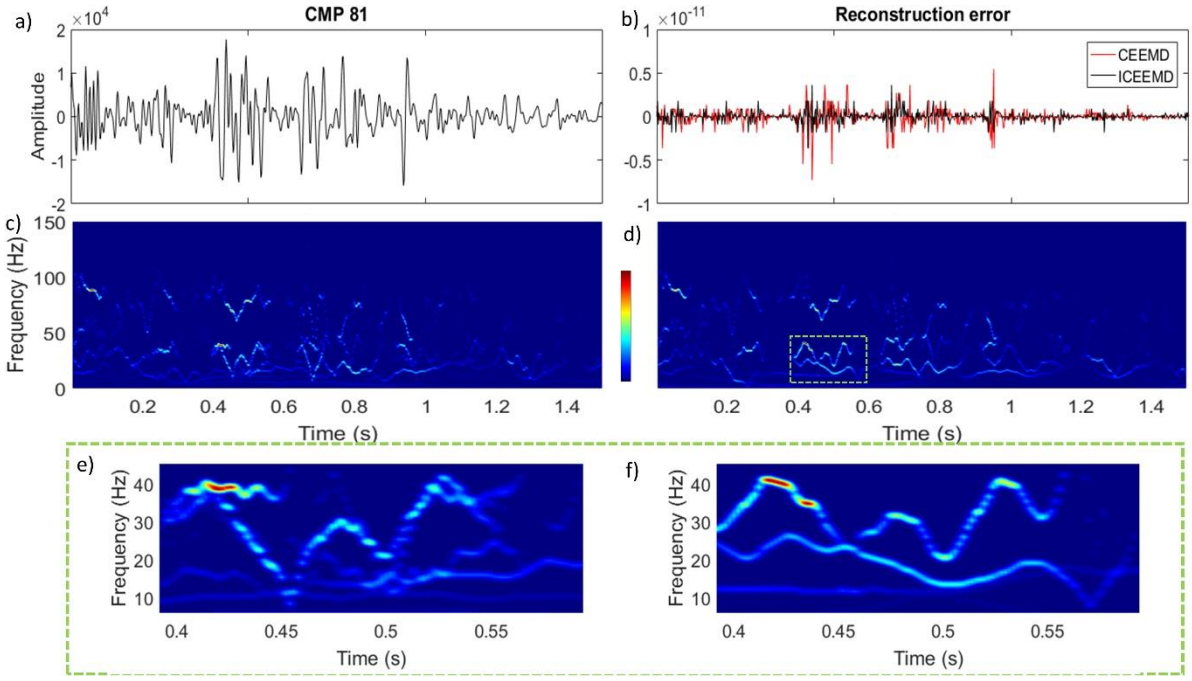

Figure 5.6: Analysis on CMP 81 seismic trace taken from Han and van der Baan (2013). (a) seismic signal; (b) reconstruction error; (c-d) time-frequency representation through HHT using CEEMD and ICEEMD; (e-f) zoom in the highlighted box for both techniques.

The reconstruction error is again equally accepted for both methods, although it is little less intense the for ICEEMD (Figure 5.6b). The seismic trace on CMP 81 crosses a Cretaceous meandering channel at 0.42 s, where a strong anomaly is evident around 40Hz in both methods (Figure 5.6c and Figure 5.6d). By zooming around this area (Figure 5.6e and Figure 5.6f) one can note a smoother and more consistent IFs detection and delineation for ICEEMD. Additionally, note the IFs crossing against each other around 0.45s and 0.50s for CEEMD, which does not occur for the ICEEMD. This is especially true in this zoomed area but also occurs in others time intervals, for example around 0.7s.

Case study 2:

We have applied both decomposition methods for a real seismic data from an offshore field in Campos Basin, Brazil. In seismic data particularly, it is hard to identify the physical meaning of the lasts components. Specifically, after IMF4, the components are at the very low end in the frequency spectrum (<10Hz in our 4ms sampled data). In this way, in order to better evaluate, compare and analyze the methods in our seismic data, we grouped the components from IMF4 until the final one, in a similar way we did for the synthetic signal case. This is additionally justified by mostly two reasons: (i)

because the decomposition is directly related to the signal complexity and may result into an unknown number of components, if we intend to use them for seismic attributes calculation, it is interesting to have a fixed number of components; (ii) the number of components will impact directly the size on disk and can unnecessarily overload both, machine and the interpreter, with no geological and physical gain. With this in mind, the components extracted using CEEMD and ICEEMD are shown in Figure 5.7 and Figure 5.8.

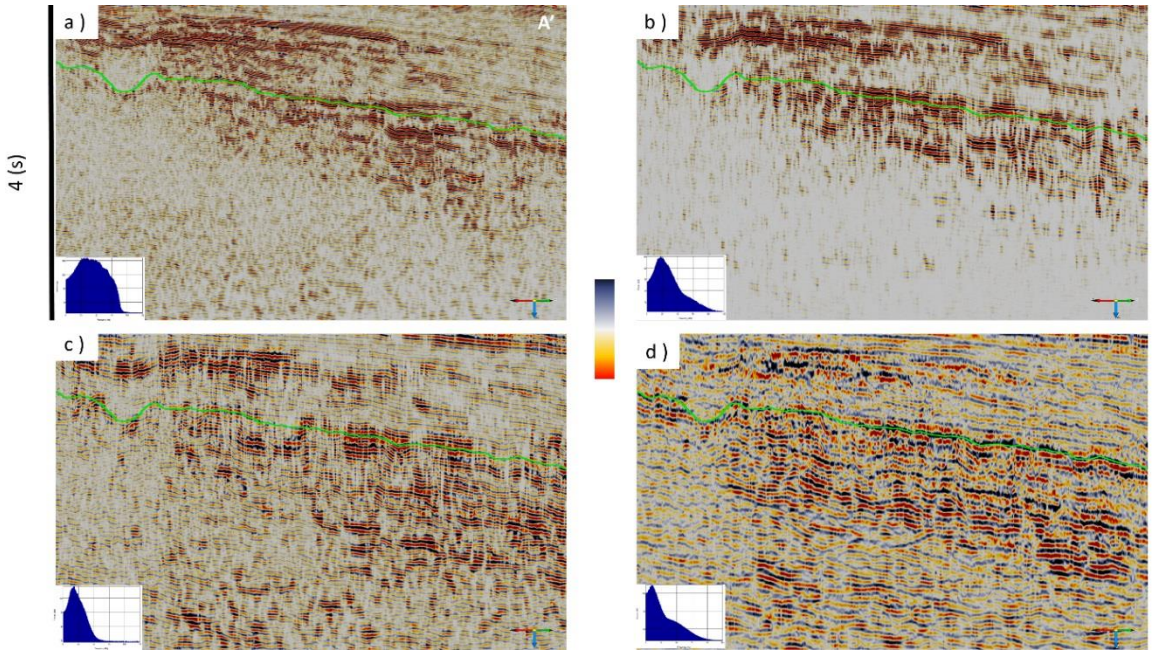

Figure 5.7: CEEMD components. (a-d) IMF1-4 with corresponding frequency spectrum (inset).

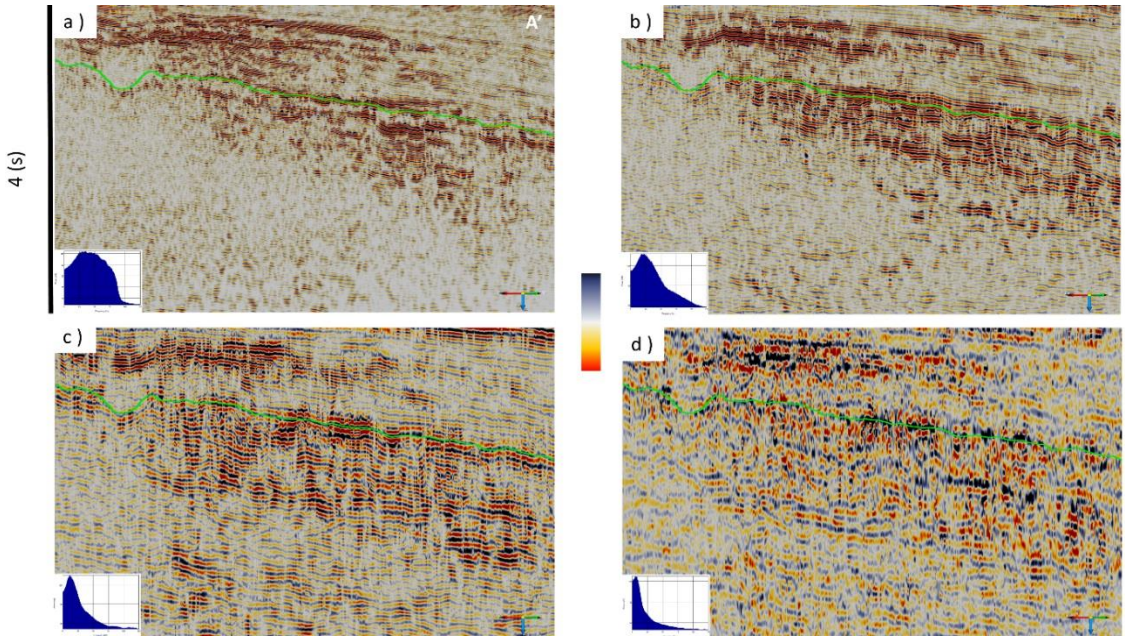

Figure 5.8: ICEEMD components. (a-d) IMF1-4 with corresponding frequency spectrum (inset).

The most evident difference between the two methods is related with IMF2 (Figure 5.7b and Figure 5.8b). In the CEEMD, IMF2 is quite obscure in the second half of time direction and its geological meaning is not straightforward. Additionally, the lateral continuity is considerable impaired, mostly in IMF2 but well expressed in the IMF3 too.

A good way to verify the main differences in the IMF2 from the two methods is by evaluating the cosine of instantaneous phase attribute (Figure 5.9). Barnes (2007) call attention for some redundant attributes which does not provide any interpretational gain over one another. Cosine of instantaneous phase, for example, can be seen as a strong amplitude gain or an amplitude normalization, which can be considered as a processing rather than an attribute. Basically, such processing removes the amplitude contrast, retaining the amplitude of peaks and troughs in their position and pushing the weak events to exhibit equal strength. Such processing highlights the content and characteristics intrinsic in the IMFs. Note the expressive artifacts in the left side below the horizon H1 in the CEEMD-based processing, which does not occur for the ICEEMD. Figure 5.9c and Figure 5.9d show a zoomed area highlighted by the rectangle in Figure 5.9a which exemplifies such observation. By this point of view, we can obtain a more stable and consistent decomposition by the ICEEMD.

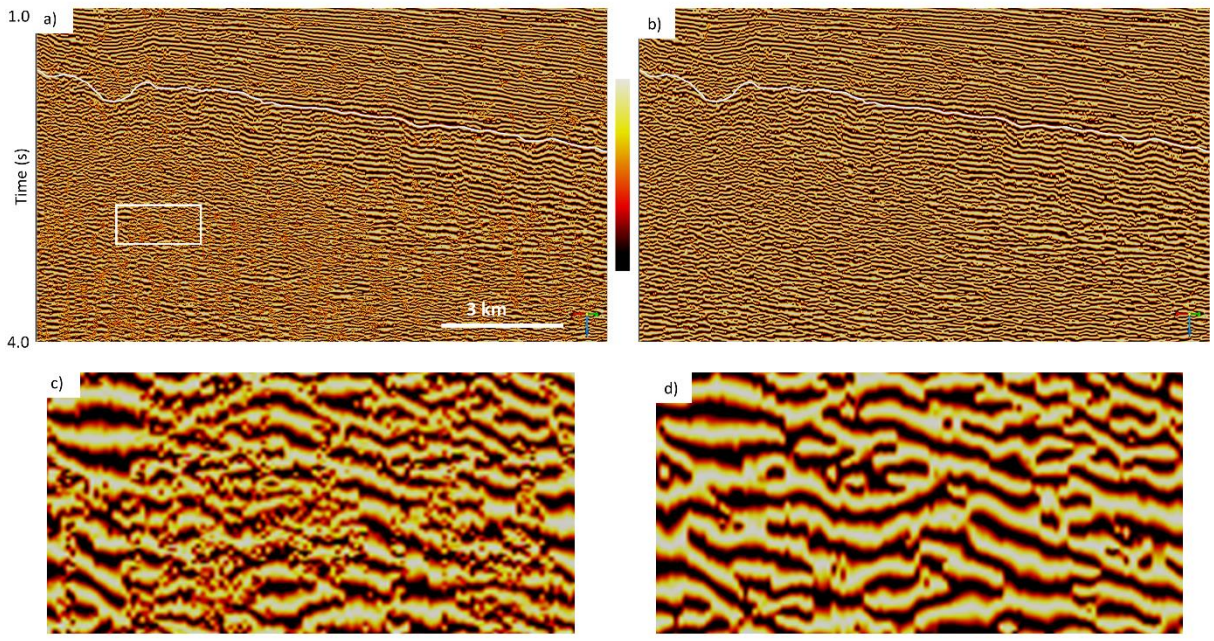

Figure 5.9: Cosine of instantaneous phase of IMF2 from (a and c) CEEMD and (b and d) ICEEMD. The highlighted box in (a) is the zoomed area.

As an example of the time-frequency distribution through CEEMD and ICEEMD, we picked a seismic trace pointed by the red arrow in Figure 5.10a. At the first glance, the time-frequency distributions look like the same (Figure 5.10c and Figure 5.10d). However, a careful inspection shows some considerable differences. In Figure 5.10e and Figure 5.10f we can see in detail the behavior of IFs for each method. The colormaps are adjusted to emphasize the differences. In the Figure 5.10e, the IF starting in 1.1s and 15Hz is well behaved along the entire time interval in the ICEEMD-based method, with little noise influence on it and consistent amplitude value, contrary to CEEMD-based IF, where this component is quite noisy and considerable discontinuous. The low frequency component starting around 7 Hz in the ICEEMD peak frequency is continuous and smooth along the time entire interval displayed in Figure 5.10e. For CEEMD, this component is poorly detected. A similar analysis can be verified in Figure 5.10f, where the most expressive component is well defined in ICEEMD and very segmented and noisy in CEEMD.

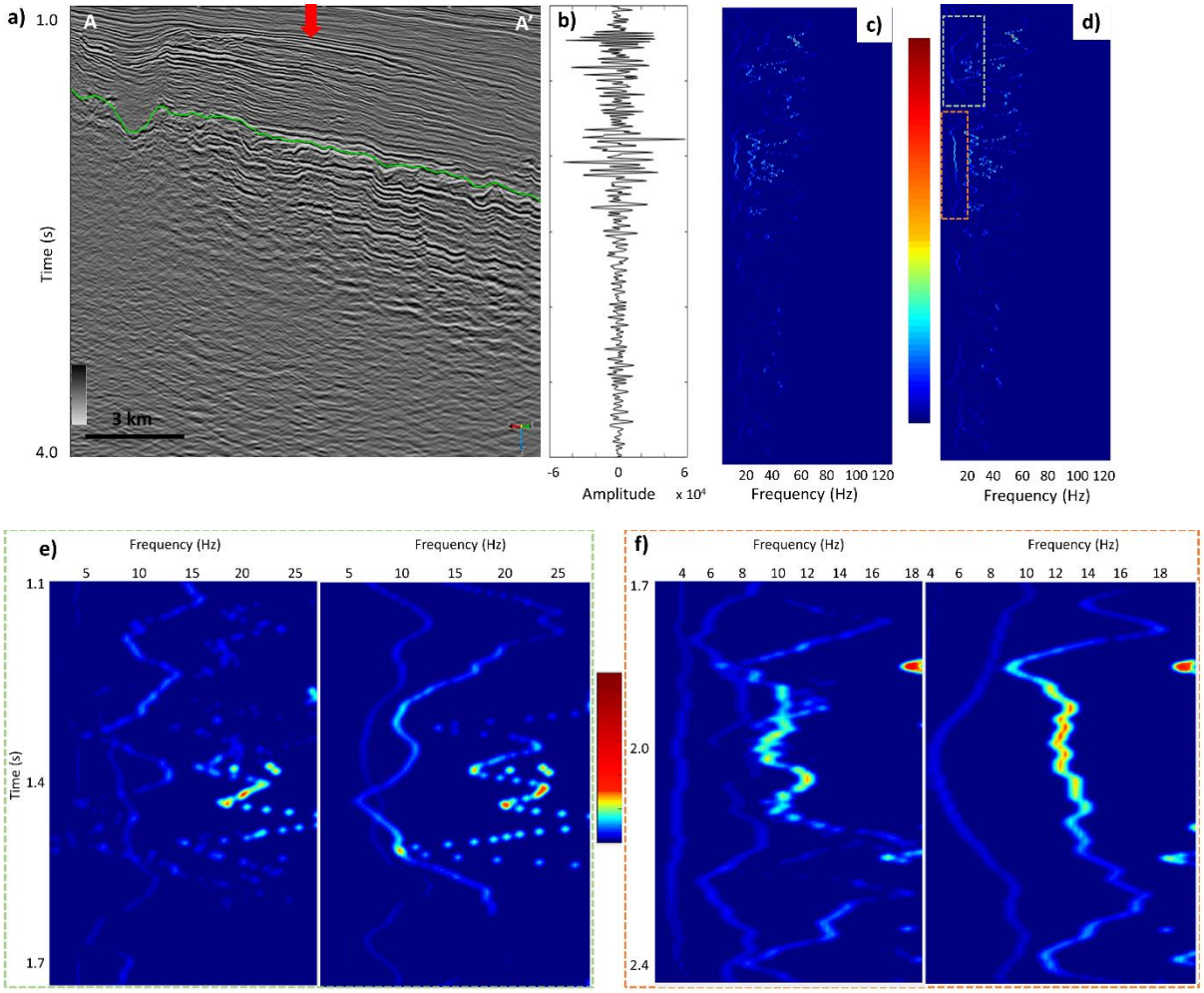

Figure 5.10: Instantaneous spectrum on seismic signal. (a) seismic section; (b) seismic trace with its time-frequency distribution through (c) CEEMD and (d) ICEEMD; (e-f) zoom in the highlighted areas in (d).

The peak frequency attribute, which is the frequency with the largest amplitude among all IMF components, captures the information from the spectral decomposition, generating a single attribute which is related to tuning effects at varying thicknesses. Figure 5.11 shows the peak frequency overlaid onto the original seismic data. Because it varies rapidly, spatially and temporally, the interpretation of EMD-based peak frequency seismic attribute is known to be challenging (Han and van der Baan, 2013). The highlighted white boxes show some regions where we can verify a higher energy concentration and less noise-affected peak frequency in ICEEMD over CEEMD. The box I, for example, shows that this energy spreading in CEEMD mix two neighbor transitions (Figure 5.11c), while in ICEEMD they are well separated. The arrow in the box II shows a good high-frequency energy concentration exactly in the layer transition in ICEEMD, while in CEEMD-based peak frequency, the energy spreads up in its left

side, indicating a possible noise-related pattern (Figure 5.11). Similar pattern can be seen in the up-pointed arrow. Overall, the peak frequency attribute obtained by the two methods are quite similar. Their cross-correlation is relatively high (r = 0.87) and the differences relies mainly in the 5-35Hz band of ICEEMD-based peak frequency which spread up to 80Hz in the CEEMD (Figure 5.11e, green box). Therefore, a noiseless and a lower energy spreading in the peak frequency is achieved by ICEEMD, which can lead to an improved resolution and better definition of the frequency inherent to a specific layer.

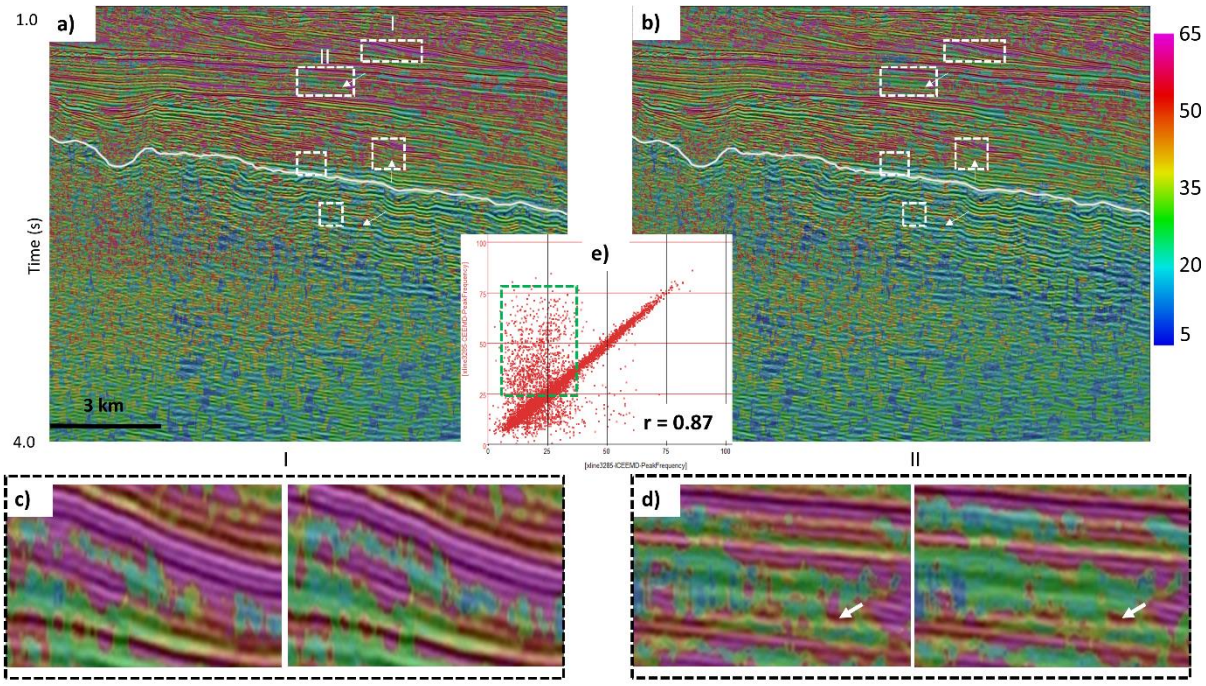

Figure 5.11: Peak frequency attribute computed from (a) CEEMD; (b)ICEEMD overlaid onto the original seismic data. (c) and (d) is the zoomed areas I and II in (a); (e) cross-correlation between CEEMD- and ICEEMD-based peak frequency

It is important to emphasize that, by definition, the IF is only physically meaningful when $z(t)$ just has one single frequency component present at any time instant. Because we have as many IF as the number of IMF, the peak-frequency will capture the most expressive IF between all IMFs. Therefore, if $z(t)$ consists of two frequency components with equal amplitudes, the IF will be the mean of the two frequencies, consequently smoothing the peak-frequency attribute, possibly merging and not resolving close interfaces (compare Figure 5.11c). If the amplitudes are not equal, the IF will vary periodically with the difference frequency of the two. As the number of

components increase, the behavior turns more and more chaotic and noisy (compare Figure 5.11d).

Next, we extract the 15, 30 and 50Hz frequency components through both techniques (Figure 5.12). For comparison purpose, we also evaluate those frequencies slices from short-time Fourier transform using 148ms (37 samples). The differences between Fourier- and EMD-based methods are evident. As already noticed in the Han and van der Baan work (2013), a much sparser output is achieved by EMD-based results, which resolves the spectral characteristics of the various reflections more clearly than the short-time Fourier. Regarding the isofrequency components for CEEMD and ICEEMD methods, the differences are not straightforward. Their cross-correlation are 0.86, 0.95 and 0.97 for the 15Hz, 30Hz and 50Hz components, respectively. Therefore, in this particular case both methods are equally accepted for this specific attribute.

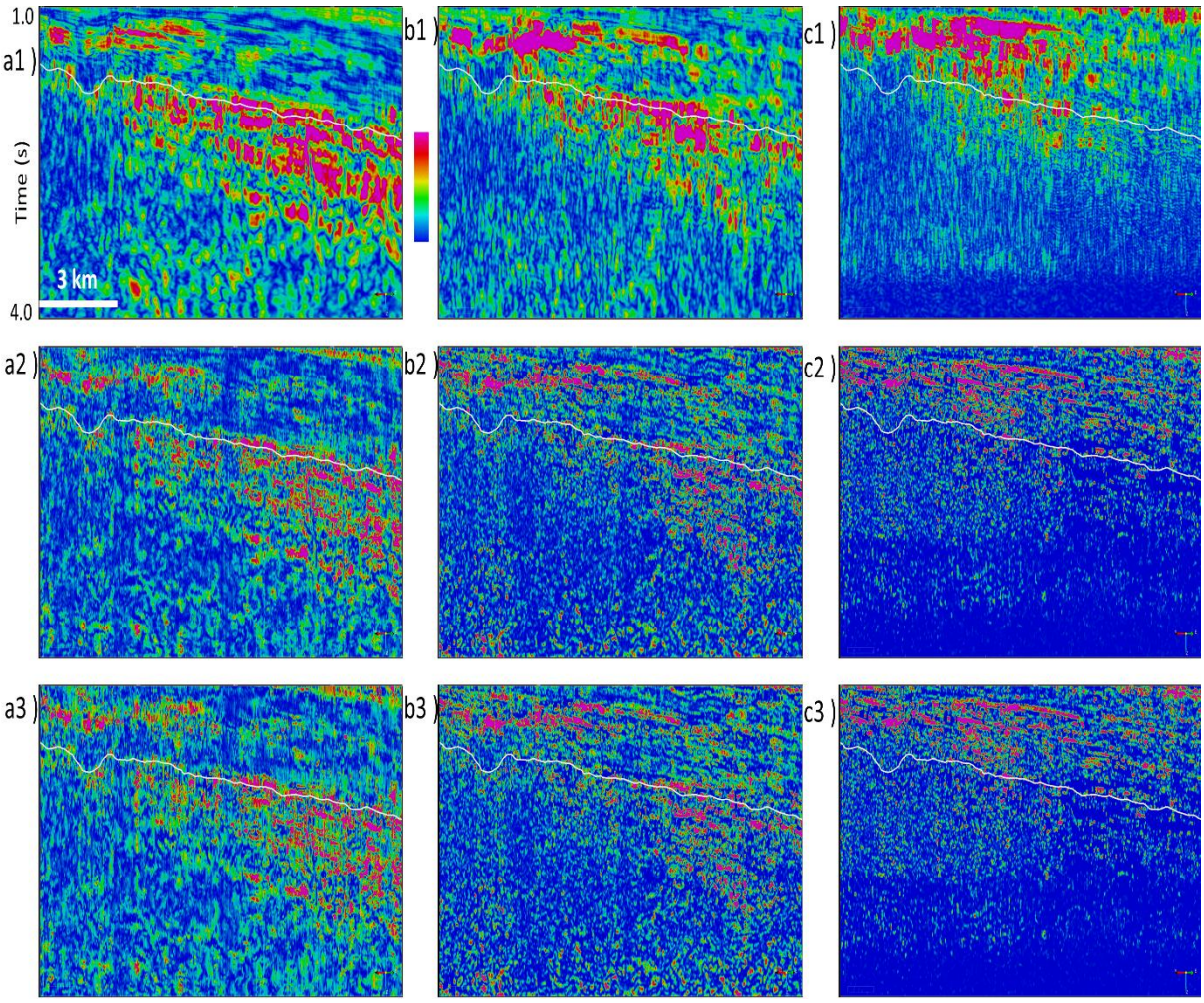

Figure 5.12: Isofrequency sections through short-time Fourier transform (*top*), CEEMD (*center*) and ICEEMD (*bottom*). (a1-a3) 15Hz; (b1-b3) 30Hz; and (c1-c3) 50Hz.

CONCLUSIONS

In this work we have evaluated and compared the CEEMD and a recent proposed development of it, called ICEEMD. Conventional attributes calculated in the EMD-based framework have been also evaluated. In our synthetic signal case, the differences and the superiority of ICEEMD over CEEMD are quite evident. The IMFs from ICEEMD are better separated with less noise occurrence, less mode-mixing and mode-splitting, which also improve its time-frequency representation. In our first example on a real seismic trace, the TF distribution shows a more consistent IF detection and delineation for ICEEMD. Additionally, several crossing IFs are detected in the CEEMD case, which suggests a poorer mode separation. In the second example of a real seismic data application, the differences are not straightforward. The main difference occurs in the second IMF. The cosine of phase turns the presence of noise and non-geological artifacts quite evident in IMF2 from CEEMD. The lateral continuity from IMF2 and IMF3 are considerable impaired when compared with ICEEMD ones. There is no physical or geological reason to justify this gaps and "jumps" for neighbors traces. The time-frequency representation and the derived attributes are quite similar, with a subtle improvement in energy concentration and less noise interference in the ICEEMD. Regarding the isofrequency slices, they are equally accepted.

Considering the stated findings and that both methods are equivalent in time-processing and parameters needed, we understand that the ICEEMD would be more suitable for seismic signal analysis and attributes calculation than CEEMD. One important aspect that must be taken in account in the noise-assisted versions of EMD is the computational complexity. The number of noise realizations together with the sifting process turn such approach considerable computational expensive.

REFERENCES

Barnes, A. E., 2007, Redundant and useless seismic attributes: Geophysics, 72(3), P33–P38.

Bekara, M. and M. van der Baan, 2009, Random and coherent noise attenuation by empirical mode decomposition: Geophysics, 74(5), V89–V98.

Chen, Y., J. Ma, 2014, Random noise attenuation by *f-x* empirical-mode decomposition predictive filtering: Geophysics, 79(3), V81–V91.

Chen, Y., G. Zhang, S. Gan, and C. Zhang, 2015, Enhancing seismic reflections using empirical mode decomposition in the flattened domain, Journal of Applied Geophysics, 119, 99-105.

Colominas, M. A., G. Schlotthauer, and M. E. Torres, 2014, Improved complete ensemble EMD: A suitable tool for biomedical signal processing: Biomedical Signal Processing and Control, Volume 14, 19-29.

Du, K.-j., J.-x. Cao, Y.-j. Xue and X.-j. Wang, 2015, Seismic facies analysis based on self-organizing map and empirical mode decomposition: Journal of Applied Geophysics, Volume 112, 52-61.

Flandrin, P., G. Rilling and P. Gonçalvés, 2004, Empirical mode decomposition as a filter bank. IEEE Signal Processing Letters, 11, 112–114.

Han, J. and M. van der Baan, 2013, Empirical mode decomposition for seismic time-frequency analysis: Geophysics, 78(2), O9-O19.

Han, J. and M. van der Baan, 2015, Microseismic and seismic denoising via ensemble empirical mode decomposition and adaptive thresholding: Geophysics, 80(6), KS69–KS80.

Huang, J., and B. Milkereit, 2009, Empirical mode decomposition based instantaneous spectral analysis and its applications to heterogeneous petrophysical model construction: CSPG CSEG CWLS Convention, 205–210.

Huang, N. E., Z. Shen, S. R. Long, M. C. Wu, H. H. Shih, Q. Zheng, N.-C. Yen, C. C. Tung, H. H. Liu,1998. The empirical mode decomposition and the Hilbert spectrum for nonlinear and non-stationary time series analysis: Proceedings of the Royal Society A Mathematical Physical and Engineering Sciences 454 (1971), 903–995.

Huang, N. E., Z. Wu, S. R. Long, K. C. Arnold, X. Chen, K. Blank, 2009, On instantaneous frequency: Advances in Adaptive Data Analysis, 1(2), 177–229.

Huo, S., 2015. Adaptive local frequency: Geophysics, 80(5), V115–V118.

Liu, Y., G. Yang, W. Cao, 2015, The division of sedimentary cycle based on HHT: 85th Annual Internationa lMeeting, SEG, 1902–1906.

Magrin-Chagnolleau, I., and R. G. Baraniuk, 1999, Empirical mode decomposition based time-frequency attributes: 69th Annual InternationalMeeting, SEG, 1–4.

Marfurt, K. J. and R. L. Kirlin, 2001, Narrow-band spectral analysis and thin-bed tuning: Geophysics, 66(4), 1274–1283.

Matos, M. C. and K. J. Marfurt, 2013. Improving wavelet transform deconvolution with empirical mode decomposition: 83rd Annual International Meeting, SEG, Expanded Abstracts.

Taner, M. T., F. Koehler and R. E. Sheriff, 1979, Complex seismic trace analysis. Geophysics, 44(6), 1041–1063

Tary, J. B., R. H. Herrera, J. Han and M. van der Baan, 2014, Spectral estimation—What is new? What is next?: Reviews of Geophysics, 52(4), 723–749,

Torres, M., M. Colominas, G. Schlotthauer and P. Flandrin, 2011, A complete ensemble empirical mode decomposition with adaptive noise: IEEE International Conference on Acoustics, Speech and Signal Processing (ICASSP), 4144–4147.

Wu, Z. and N. E. Huang, 2009, Ensemble empirical mode decomposition: A noise-assisted data analysis method. Advances in Adaptive Data Analysis, 1(1), 1–41.

Zhang, M., H. Wang, Z. Sui, X. Wang, Y. Zhang, 2015, A novel approach of seismic instantaneous frequency extraction and its application on field data. 85th Annual International Meeting, SEG, Expanded Abstracts, 1856–1860.

CHAPTER 6: CONCLUSIONS

Since the first classical paper on seismic attributes from Taner et al. (1979), the subject of attribute extraction and analysis has fascinated and conducted the geophysical interpreters. The work from Partyka et al. (1999) on interpretational aspects of spectral decomposition has opened a new door to the exploration community. Together with the advent of interpretation workstation and visualization systems, the establishment of these powerful 3D algorithms has changed remarkably the methodologies applied in seismic interpretation to extract hidden interpretive information from seismic volumes.

In this dissertation I examine some limitations of established techniques in the literature and propose new ideas and workflows based on the spectral characteristic of the seismic data for a more in depth interpretation of reservoir geometry and its physical aspects.

In chapter 2, I evaluate the complexity on handling the iso-frequency volumes generated by spectral decomposition. Typically, an interpreter might generate 80 or more spectral magnitude and phase components covering the usable seismic bandwidth at 1-Hz intervals, presenting a challenge in conveying the meaning of these data in a concise and interpreter-friendly way. The most common means of displaying these components is simply by scrolling through them to determine manually which single frequency best delineates an anomaly of interest. More sophisticated techniques try to overcome such empiricism by using mathematical approaches, such as the average of three non-overlapping spectral bands (Stark, 2006); the use of three predetermined basis functions, producing a more continuous and overlapped spectral bands (Liu and Marfurt, 2007); or the use of projections in a multidimensional space (PCA) (Guo et al., 2009). In this way, by going beyong the Gaussian assumption and taking advantage of higher order statistics to find a new set of variables, I propose the use of ICA to generate a set of independent spectral components to get a detailed image of the geology under investigation. Some remarks on this technique are that we could (i) better suppress the acquisition foot print; (ii) better delineate the channel system in the studied area; (iii) further analysis on different approaches for dimensionality reduction should be studied; (iv) a physical and geological guide for choosing the extracted ICs can enrich the technique.

An attempt in such direction is made in chapter 3, where we evaluate the ICs jointly with others geometrical (incoherence and fault moment filter) and physical (sweetness)

attributes. The combination of such attributes allowed us (i) to map the three main discontinuities fault system in the field; (ii) to delineate the reservoir into four main architectural elements; (iii) estimate the predominant facies for each architectural element; (iv) to correlate structurally the studied field with the JC in Bahamas, corroborating or even improving the thesis of them being analogous system.

In chapter 4, I propose the use of the DR algorithm, a technique for spectral enhancement and resolution improvement based on derivatives of the seismic data, as a pseudo-filter to extract dissimilar features at different spectral bands. Considering that the broadband data is a composite of various geological features which may have different scale ranges, the use of such pseudo-filter jointly with similarity attribute aims to capture the discontinuities intrinsic in each spectral band. Remarks from this technique are: (i) a different view using the Fourier properties allowed us to enrich the mathematical understanding of the technique; (ii) the trace normalization, which uses the median value of the absolute trace, should be further analyzed by means of different measurements such as the rms energy or other physical property (iii) a better definition on the smoothed component Y^{NS} should be evaluated in order to cover the "blindness" around 25Hz (Figure 4. 3); (iv) overall, a more detailed definition of the faults and karsts structures is achieved.

In chapter 5, I evaluate the ICEEMD, a recent proposal of a noise-assisted version of EMD, and compare it with the CEEMD to time-frequency analysis and seismic attributes commonly used in the EMD-framework. In the synthetic signal analysis, my observations are: (i) the IMFs from ICEEMD are better separated (less mode-mixing) with less noise occurrence; (ii) as consequence, the IF detection and definition are more consistent and the time-frequency representation is also improved. For the first real seismic data example, (i) the TF distribution and the IFs detection and delineation are more consistent for ICEEMD, with less crossings IFs than the CEEMD, which suggests a better mode separation. In the second real seismic data example, the differences are not straightforward. In this case, my analysis shows mainly that (i) the iso-frequency components from both techniques are quite equivalent and are equally accepted. When compared with the ones obtained by FFT, they have higher time-frequency resolution, but the associated peak-frequency attribute varies more rapidly, spatially and temporally, rendering the interpretation more challenging; (ii) despite their high cross-correlation (r=0.87), the peak-frequency attribute is slightly more concentrated by means of ICEEMD, which can lead to an improved resolution and better definition of

the frequency inherent to a specific layer; (iii) the most expressive difference between the two EMD-based methods is related to the IMF2, which is quite obscure in the second half in time direction and the lateral continuity is considerable impaired for CEEMD. The cosine of instantaneous phase emphasizes such expressions. No physical or geological element justify these discontinuities for neighbors traces. Therefore, considering the stated findings and that both methods are equivalent in time-processing and parameters needed, I understand that ICCEMD would be the reference method for the noise-assisted variation of EMD. One important aspect that must be taken in account in the noise-assisted versions of EMD is the computational complexity. The number of noise realizations together with the sifting process turn such approach considerable computational expensive.

REFERENCES

Partyka, G., J. Gridley, and J. Lopez, 1999, Interpretational applications of spectral decomposition in reservoir characterization: The Leading Edge, 18, 353–360.

Taner, M. T., Koehler, F., E. and R., S., 1979. Complex seismic trace analysis: Geophysics, 44(6), 1041–1063.